

Andrea Leite Gouvêa

LAMB SHIFT IN MUONIC HELIUM: X-RAY DETECTION SYSTEM

Ph.D. thesis in Physics Engineering, in the field of Instrumentation, performed under scientific guidance of Dr. Luis Manuel Panchorrinha Fernandes and Dr. Randolph Pohl and presented to the Physics Department of the Faculty of Sciences and Technology of the University of Coimbra

September 2014



UNIVERSIDADE DE COIMBRA

Lamb Shift in Muonic Helium: X-ray Detection System

Scientific Supervisor: Dr. Luis M. P. Fernandes

Scientific Co-Supervisor: Dr. Randolph Pohl

A Thesis Presented for
The Doctor of Philosophy in Physics Engineering
University of Coimbra

Andrea Leite Gouvêa

September 2014

© by Andrea Leite Gouvêa, 2014
All Rights Reserved.

This work is funded by FEDER, through *Programa Operacional Factores de Competitividade* - COMPETE, in the scope of the projects PTDC/FIS/102110/2008, PTDC/FIS-NUC/0843/2012, and by National Funds through FCT - *Fundação para a Ciência e Tecnologia*, in the frame of the Ph.D. grant with reference SFRH/BD/66731/2009.



À minha família

À Teresa

Acknowledgements

First and foremost, I would like to express my deepest gratitude to my thesis advisor, Dr. Luis Manuel Panchorrinha Fernandes. His peerless support and guidance were indispensable for the completion of this journey. During the last four years, I have learned from his deep experimental and theoretical understanding on particle physics. His frank yet patient attitude, and strong leadership skills led to the successful completion of the project. I would also like to acknowledge our team leader, Professor Joaquim Marques Ferreira dos Santos, for his support, help and patience during my PhD research, especially for his tips and for revising my final documents.

I also cannot forget how much I owe to my co-advisor Dr. Randolph Pohl. There are no words to express how indebted I am for offering me the possibility to learn and share his vast knowledge, and the knowledge of his group from MPQ Institute in Garching; for his kind and warm hospitality in my welcome and stay in Munich, for his patience and constant care during my 6 month journey with his group; for his strong leadership and enthusiastic driving force, essential to the successful completion of our project; for showing me, teaching me, and helping me in so many areas beyond science.

I would like to express my deepest gratitude to Dr. Franz Kottmann for his mentoring; for his constant and unmatched support; for the kindness, patience and time he shared with me; for his enlightening teachings on experimental and theoretical particle physics; for our captivating talks during lunchtime about physics and life; for making my life at PSI much easier. I would also like to thank Dr. Tobias Nebel

from MPQ for his friendship, kindness and constant care; for all his patience and for the knowledge he gracefully shared with me; for making me believe that the proton radius analysis is easy if you carefully make one step at a time! My acknowledgement as well to Dr. Aldo Antognini for his ever supporting presence and kind guidance. I must also thank Marc Diepold, Jan Vogelsang, Karsten Schuhmann, Dr. François Nez, Dr. Françoise Mulhauser for all the mutual support and sharing of each one's specific knowledge.

I would also like to acknowledge all my colleagues from GIAN, Dr. Cristina Monteiro, Dr. Elisabete Freitas, Dr. Fernando Amaro and M.S. Catalin Balan for their helpfulness and support.

To all the ones who made this thesis possible, I send an enormous grateful hug. To my family, Margues, Tina, Jorge, Avó, Lourdes and Dulce. To my friends Angela, Hugo, Maria and João, Joana, Sofia, Tiago, Amanda, Inês, Adérito, Sílvia, Sarita, Vera, Silvinha, Idália and Zé, Paulo, Inês, Barbeiro, Ivânia, Cats, Lena and Jacob, Eva and Nano, Maria, Leninha, Anita, Artur, Minó and Idés. Thank you so much for everything.

I cannot forget in any way my good friend Hugo Natal da Luz. You were my lighthouse from the beginning of my journey in the Physics Department of the University of Coimbra. I could not be more grateful for your friendship. I could not be more grateful for the knowledge you always shared in the most selfless and supporting manner. You are the main reason why I am here and why this thesis ever happened.

Last but not the least, I ought to express my love and gratefulness for all the love, tenderness, understanding and everlasting support of Rui, Miguel and my parents, José and Fernanda. Thank you ever so much for always being here.

“A good head and a good heart are always a formidable combination.”

Mandela

“A vida é breve, mas cabe nela muito mais do que somos capazes de viver.”

Saramago

Abstract

An experiment with the aim to determine the Lamb shift in muonic helium has been carried out by the Charge Radius Experiments with Muonic Atoms (CREMA) Collaboration at the Paul Scherrer Institute (PSI), Switzerland. The goal of the experiment is to measure several transitions between the 2S and 2P energy levels in muonic helium ions ($\mu^4\text{He}^+$ and $\mu^3\text{He}^+$) with a precision of 50 ppm, and consequently to determine the α particle and helion nuclear charge radii (RMS value) with a relative accuracy of 3×10^{-4} .

This experiment comes after the good results attained in the muonic hydrogen Lamb shift experiment, where the muonic hydrogen Lamb shift was measured and the proton charge radius determined, which lead to the proton radius puzzle. The next proposal of the CREMA Collaboration was to extend the Lamb shift measurements to muonic helium in an attempt to help to solve the proton radius puzzle and provide additional information about the helium nucleus.

This thesis is dedicated to the X-ray detection system used in the experiment, including the detectors and pre-amplifier system. The detectors chosen are avalanche photodiodes. A detailed study of two different types of avalanche photodiode (APD), reach-through avalanche photodiode (RT-APD) from Hamamatsu Photonics and large area avalanche photodiode (LAAPD) from Radiation Monitoring Devices Inc. (RMD), has been carried out. The two APD types have different depletion region thicknesses, and consequently different detection efficiencies for 8 keV X-rays emitted by muonic helium ions.

Regarding RT-APDs, two prototypes, with $5 \times 5 \text{ mm}^2$ and $3 \times 5 \text{ mm}^2$ active areas, have been investigated for 8.2 keV detection. The studies have shown that the energy resolution improves with decreasing temperature, reaching 9.5% at 0° C for the larger prototype, and the minimum detectable energy is about 0.9 keV for the optimal operation gain region. The gain variation with temperature increases with the bias voltage applied, varying between -1.0% per °C for a bias voltage of 200 V and -1.7% per °C for a bias voltage of 400 V. The gain non-linearity between X-rays and visible light pulses has been investigated for different temperatures, showing a non-linearity of 42% at -20° C, whereas it is only 30% at 20° C for a gain of 200. The overall performance of this type of APD is inferior to the prototypes from RMD, with the additional drawback of smaller active areas available.

Concerning LAAPDs from RMD, detection efficiencies between 53 and 65% for 8 keV X-rays have been measured for homogeneous irradiation of the whole efficient surface area of $13.5 \times 13.5 \text{ mm}^2$ and considering the effect of the X-ray incident angle. Energy resolution values below 20% (at FWHM) have been measured for 8 keV X-rays, at -30° C, and one prototype has even shown a much lower value of 9%, due to the small leakage current and good non-uniformity presented. The energy resolution behaviour at low temperatures has been investigated. No significant dependence on temperature was observed between -30° C and -20° C since the dark current difference is not significant for the degradation of the energy resolution. APDs from RMD were chosen for the experiment as their operation is much more reliable and they have larger active areas, appropriate for the detection space available around the gas target in the experiment apparatus.

Furthermore, new pre-amplifier and post-amplifier arrays were developed in view of avoiding crosstalk between adjacent channels and ringing effects, and to provide faster signals. Several prototypes were tested. The best pre-amplifier/post-amplifier configuration has shown an energy resolution of about 16% and a signal to noise ratio (SNR) of 6.5, as well as pulses with good shape, without undershoot.

During the beam time, an average energy resolution of 18.2% was measured for the 8.2 keV X-ray peak. This value demonstrates the overall good performance of the LAAPDs for 8.2 keV X-rays, similarly to their performance for 1.9 keV X-rays in the previous muonic hydrogen experiment.

The first line of $\mu^4\text{He}^+$ ion was measured in the second half of 2013 and the second one in 2014. As preliminary result of the experiment, two resonance curves have been obtained, corresponding to the energy differences $2S_{1/2} - 2P_{3/2}$ and $2S_{1/2} - 2P_{1/2}$, with wavelengths of 813 nm and 899 nm, respectively. The $\mu^3\text{He}^+$ ion has been investigated this year and the corresponding resonances have been found. An extensive analysis of the data will take place in the near future. From this data, the helium RMS charge radius, as well as the fine structure from both ions, $\mu^4\text{He}^+$ and $\mu^3\text{He}^+$, will be revealed. The magnetic moment distribution of $\mu^3\text{He}^+$ will also be disclosed.

Sumário

A Colaboração CREMA (Charge Radius Experiments with Muonic Atoms) realizou uma experiência no Instituto Paul Scherrer (PSI), na Suíça, com vista a determinar o desvio de Lamb no hélio muónico. O objetivo da experiência foi medir as energias de diferentes transições entre os níveis 2S e 2P nos iões do hélio muónico ($\mu^4\text{He}^+$ e $\mu^3\text{He}^+$) com uma precisão de 50 ppm e, conseqüentemente, determinar os correspondentes raios de carga nuclear (valor RMS) com uma exatidão relativa de 3×10^{-4} .

Esta experiência vem no seguimento dos bons resultados obtidos na experiência de espectroscopia laser do hidrogénio muónico, na qual foi medido o desvio de Lamb no hidrogénio muónico e determinado o raio de carga do protão, o que originou um “puzzle” em torno do raio do protão. A proposta seguinte da colaboração CREMA foi alargar as medições do desvio de Lamb ao hélio muónico numa tentativa de ajudar a solucionar o “puzzle” em torno do raio do protão e de fornecer informações adicionais sobre o núcleo do hélio.

A presente tese é dedicada ao sistema de deteção de raios X usado na experiência, nomeadamente os detetores e o sistema de pré-amplificadores. Os detetores selecionados são os fotodíodos de avalanche. Foi realizado um estudo detalhado sobre os dois tipos de fotodíodos de avalanche (APDs), fotodíodos de avalanche do tipo “reach-through” (RT-APDs) produzidos pela Hamamatsu Photonics e os fotodíodos de avalanche de “grandes áreas” (LAAPDs) produzidos pela Radiation Monitoring Devices Inc. (RMD). Os dois tipos de APDs possuem diferentes espessuras na região

de depleção e, conseqüentemente, diferentes eficiências de detecção para os raios X de 8 keV emitidos pelos íons de hélio muónico.

Os dois protótipos de RT-APDs adquiridos, com áreas ativas de $5 \times 5 \text{ mm}^2$ e $3 \times 5 \text{ mm}^2$, foram estudados na detecção de raios X de 8.2 keV. Os estudos demonstraram que a resolução em energia melhora com a diminuição da temperatura, atingindo 9.5% a 0°C para o protótipo maior, sendo que a energia mínima detetável é de aproximadamente 0.9 keV na região de ganhos de operação ótima. A variação do ganho com a temperatura aumenta com a tensão aplicada, variando entre -1.0% por $^\circ\text{C}$ para uma tensão de 200 V e -1.7% por $^\circ\text{C}$ para uma tensão de 400 V. A não-linearidade do ganho entre raios X e impulsos de luz visível foi também estudada para diferentes temperaturas, tendo-se obtido uma não-linearidade de 42% a -20°C , para um ganho de 200, sendo de apenas 30% a 20°C . O desempenho global deste tipo de APDs é inferior ao dos protótipos da RMD com a desvantagem adicional das áreas ativas disponíveis serem mais pequenas.

Relativamente aos fotodíodos de avalanche de “grandes áreas” da RMD, foram medidas as eficiências de detecção para raios X de 8 keV para 20 protótipos, tendo-se obtido valores entre 53% e 65% para uma irradiação homogênea da área ativa de cada APD ($13.5 \times 13.5 \text{ mm}^2$) e considerando o efeito do ângulo de incidência dos raios X no alvo de hélio usado na experiência. Valores de resolução em energia abaixo dos 20% foram obtidos para raios X de 8 keV a -30°C e um dos protótipos apresentou até um valor consideravelmente mais baixo, de 9%, devido à pequena corrente de fuga e boa não-uniformidade apresentadas. Foi estudado o comportamento da resolução em energia a baixas temperaturas, sendo que não foi observada uma dependência significativa da temperatura, entre -30°C e -20°C , uma vez que a diferença na corrente de fuga não é significativa para a degradação da resolução em energia. Os APDs da RMD foram selecionados para a experiência uma vez que a sua operação é bastante mais fiável e possuem áreas ativas de maior dimensão, adequadas ao espaço de detecção disponível em torno do alvo gasoso na experiência.

Além disso, foram desenvolvidos novos pré-amplificadores e pós-amplificadores com vista a evitar interferências entre canais adjacentes e tornar os sinais mais rápidos. Foram testados vários protótipos. A melhor configuração pré-amplificador/pós-amplificador apresentou uma resolução em energia de aproximadamente 16% e uma relação sinal-ruído (SNR) de 6.5, bem como impulsos com forma adequada.

Durante o tempo de feixe, uma resolução em energia média de 18.2% foi medida no pico de raios X de 8.2 keV. Este valor demonstra o bom desempenho global dos LAAPDs para raios X de 8.2 keV, semelhante ao seu desempenho para raios X de 1.9 keV na experiência anterior com hidrogénio muónico.

A primeira risca do ião $\mu^4\text{He}^+$ foi medida na segunda metade do ano de 2013 e a segunda risca em 2014. Como resultado preliminar da experiência, foram obtidas duas curvas de ressonância, que correspondem às diferenças de energia $2S_{1/2} - 2P_{3/2}$ e $2S_{1/2} - 2P_{1/2}$, com comprimentos de onda de 813 nm e 899 nm, respetivamente. O ião $\mu^3\text{He}^+$ foi estudado este ano, tendo sido identificadas as respetivas ressonâncias. Num futuro muito próximo será efetuada uma análise exaustiva dos dados. A partir destes dados, serão estimados os raios de carga dos iões de hélio, bem como a estrutura fina de ambos os iões $\mu^4\text{He}^+$ e $\mu^3\text{He}^+$. A distribuição de momento magnético do ião $\mu^3\text{He}^+$ será igualmente determinada.

Contents

List of Figures	xvii
List of Tables	xxi
List of Abbreviations	xxiii
1 Introduction	1
2 Muonic Helium Experiment Background	7
2.1 The Lamb Shift in the Hydrogen Atom and Respective Contributions	7
2.2 Muonic Atoms	11
2.3 X-ray Detectors for Spectroscopy of Muonic Atoms	14
3 X-ray Detection with Avalanche Photodiodes	21
3.1 Interaction of Radiation with Matter	21
3.1.1 X-rays	22
3.1.2 Charged Particles	24
3.2 X-ray Detection	27
3.3 Avalanche Photodiodes	31
3.3.1 Operation Principle	31
3.3.2 Operational Characteristics	34
4 Muonic Helium Lamb Shift Experiment: Principle and Apparatus	39
4.1 Muon Beam Line and Target Systems	41

4.2	Laser System and Optical Cavity	45
4.3	X-ray and Electron Detectors	46
5	Reach-Through Avalanche Photodiodes for 8 keV X-ray Detection	51
5.1	Experimental Setup	53
5.2	Gain Measurements	55
5.2.1	Gain Determination	55
5.2.2	Gain Non-Linearity	55
5.2.3	Temperature Dependence	58
5.3	Response in X-Ray Detection	60
5.3.1	Energy Resolution	61
5.3.2	Minimum Detectable Energy	62
5.4	Contributions to the Energy Resolution	63
5.4.1	Energy Resolution for X-rays and Light	67
5.4.2	Electronic Noise	68
5.4.3	Intrinsic Resolution and Gain Non-Uniformity	70
5.5	Excess Noise Factor	74
5.6	Discussion	76
6	The X-ray Detection System for the μHe Experiment	77
6.1	Avalanche Photodiode for X-ray Detection	78
6.1.1	Experimental Setup for APD Tests	78
6.1.2	Preliminary Tests	81
6.1.3	Detection Efficiency	85
6.1.4	Spatial Non-Uniformity	95
6.1.5	Energy Resolution for 8 keV X-rays	96
6.2	The Pre-Amplifier System	99
6.2.1	The New Pre-Amplifier Concept	101
6.2.2	Pre-Amplifier Prototypes	102
6.2.3	Pre-Amplifier Tests and Results	106

6.3 Discussion	115
7 Preliminary Results of the Muonic Helium Experiment	117
8 Conclusions	127
A Event Structure	131
Bibliography	133
Curriculum Vitae	147
List of Publications	149

List of Figures

2.1	Energy levels in the hydrogen atom according to Bohr, Dirac and Lamb theories.	10
2.2	Energy level of $\mu^4\text{He}^+$	12
2.3	LAAPDs from API used in 2002 run.	18
2.4	LAAPDs from RMD with $13.5 \times 13.5 \text{ mm}^2$ active area.	18
3.1	Cross sections for several interaction mechanisms as a function of the X-ray energy deposited in Si material.	23
3.2	The Bragg peak of protons.	26
3.3	Schematic of the RT-APD structure and the electric field strength. . .	33
4.1	Principle of excitation for the $2S - 2P$ transition.	40
4.2	Part of the complex experimental apparatus used for the muonic helium Lamb shift experiments, located in the πE5 area.	42
4.3	Schematic of the muon beam line and target systems.	43
4.4	Schematic of the PSC solenoid with 1 m length.	44
4.5	Schematic of the laser system used in the muonic helium Lamb shift experiment.	46
4.6	Multipass cavity and one LAAPD array mounted inside the target. .	47
4.7	One array of APD detectors from RMD, model S1315.	48
4.8	Schematic showing the X-ray and electron detectors inside the target.	49

5.1	RT-APDs from Hamamatsu Photonics with active areas of $3 \times 5 \text{ mm}^2$ and $5 \times 5 \text{ mm}^2$	54
5.2	Gain obtained for both 3×5 and $5 \times 5 \text{ mm}^2$ APD prototypes as a function of bias voltage.	56
5.3	X-ray and visible light gains as a function of bias voltage at 25°C . The dark current is also plotted.	57
5.4	Gain non-linearity between X-rays and visible light pulses as a function of bias voltage for different temperatures.	58
5.5	Gain non-linearity between X-rays and visible light pulses as a function of the APD gain for different temperatures.	59
5.6	X-ray gain as a function of bias voltage for different temperatures. . .	60
5.7	X-ray gain as a function of temperature at different bias voltages. . .	61
5.8	Typical energy distributions for 8 keV X-rays, obtained with two RT-APD prototypes.	62
5.9	Energy resolution for 8 keV X-rays as a function of gain, obtained at 20°C for both $5 \times 5 \text{ mm}^2$ and $3 \times 5 \text{ mm}^2$ prototypes.	63
5.10	Energy resolution for 8 keV X-rays as a function of gain.	64
5.11	Minimum detectable energy as a function of gain for both $5 \times 5 \text{ mm}^2$ and $3 \times 5 \text{ mm}^2$ RT-APDs.	65
5.12	Minimum detectable energy as a function of gain for the $5 \times 5 \text{ mm}^2$ prototype at different temperatures.	66
5.13	Typical pulse-height distribution obtained in the RT-APD.	67
5.14	Energy resolution for 8 keV X-rays and visible light pulses at different temperatures.	68
5.15	Electronic noise contribution (FWHM) to the RT-APD energy resolution as a function of gain, for different temperatures.	69
5.16	Dark current as a function of gain at different temperatures.	70
5.17	Dark current components, superficial and volumetric, as a function of temperature.	71

5.18	Intrinsic energy resolution for 8 keV X-rays and visible light pulses of the same energy as a function of gain obtained at (a) 20° C, (b) 0° C and (c) −20° C.	73
5.19	Gain non-uniformity (σ_U/G) obtained for three different temperatures.	74
5.20	Excess noise factor (F) as a function of the APD gain (G), for different temperatures for the $5 \times 5 \text{ mm}^2$ prototype. The straight line represents a fit to all measurements for gains above 50.	75
6.1	Schematic diagram showing the experimental setup used during measurements.	80
6.2	Array of 10 LAAPDs to be tested inside the vacuum chamber.	80
6.3	Holder for the ^{65}Zn source with a collimator of 10 mm diameter.	81
6.4	Holder for the ^{65}Zn source with no collimation for energy resolution measurements.	81
6.5	Energy distributions from arrays A and B, for 8 keV X-rays at −30° C.	83
6.6	Holder used to determine the detection efficiency.	86
6.7	The intrinsic detection efficiency for the XR-100CR detector.	87
6.8	Energy spectrum for the Si-PIN detector for 8 keV X-rays.	88
6.9	Detection efficiency of the Si-PIN detector relative to the centre of the detector along the X axis.	89
6.10	Energy spectrum for the B6 APD at −30° C with no collimator.	90
6.11	Energy spectrum obtained in the APD B6 using the collimator with 1.1 mm diameter.	91
6.12	Photon attenuation length in silicon as a function of energy.	94
6.13	Absolute efficiency (%) for Array A and B.	95
6.14	Energy resolution as a function of the bias voltage.	99
6.15	Array of 10 large area avalanche photodiodes (bottom) and 10 RAL 108A low-noise charge-sensitive pre-amplifiers (top).	101
6.16	First pre-amplifier prototype.	103

6.17	Second pre-amplifier prototype made of 5 pre-amplifier boards.	104
6.18	Final version of the pre-amplifier array.	105
6.19	Schematic diagram of the data acquisition system used to analyse the pulses.	105
6.20	Pre-amplifier signals for the first prototype at room temperature. . .	107
6.21	Pre-amplifier output pulses for the first prototype using the ^{65}Zn source at -30°C	109
6.22	Noise at the pre-amplifier output for 3 channels in 3 different conditions.	110
6.23	Output signals for different pre-amplifier's bias voltages.	112
6.24	Energy resolution and SNR as a function of the pre-amplifier bias voltage at -30°C	113
6.25	Signal shape at the post-amplifier output at -30°C	114
7.1	Number of detected pulses per LAAPD.	119
7.2	2D plot of energy versus time for all particles detected in the LAAPDs A8 and B8.	119
7.3	LAAPD A6 pulses in the muonic helium experiment.	120
7.4	Energy distribution of the pulses obtained in all LAAPDs (except B8) during beam time of the muonic helium Lamb shift experiment. . . .	121
7.5	Time spectra of all hits in the LAAPDs.	122
7.6	Time spectra of all X-ray events from Class 110 detected in two different situations: Laser Off resonance and Laser On resonance. . .	124
7.7	Very preliminary resonance curve corresponding to the first transition measured in $\mu^4\text{He}^+$ ions.	125

List of Tables

2.1	Contributions to the Lamb shift $\Delta E(2P_{1/2} - 2S_{1/2})$ in $\mu^4\text{He}^+$	15
2.2	Relevant characteristics from 3 GPSC prototypes.	16
3.1	Relevant properties of different X-ray detectors.	28
5.1	Operational parameters of the RT-APDs from Hamamatsu at 25°C. .	53
6.1	The main types of radiation emitted during the ^{65}Zn decay.	79
6.2	Operational characteristics for 20 APDs used during the μp experiment in 2009.	84
6.3	Relevant specifications for Si-PIN detectors from AmpTek.	86
6.4	Count rates and efficiencies for 8 keV X-rays attained in all APDs from array A and array B.	93
6.5	Distribution of the normalized amplitude for 8 keV X-rays.	96
6.6	Best energy resolution obtained for 8 keV X-rays for APDs from array A and array B at -30°C	97
6.7	Operational LAAPD parameters for the pre-amplifier study.	106
6.8	LAAPDs and corresponding pre-amplifier boards, with different time constants (differentiation).	108
6.9	Pre-amplifier output signal characteristic with different differentiation constants at -20°C	111
A.1	Event Classes.	132

List of Abbreviations

ADC	Analogue to Digital Converter	ETH	Swiss Federal Institute of Technology Zurich
APD	avalanche photodiode	EVG	Event Gate
API	Advanced Photonix Inc.	EEVG	End of Event Gate
CZT	cadmium zinc tellurium	FET	Field Effect Transistor
CODATA	Committee on Data for Science and Technology	FWHM	Full Width at Half Maximum
CREMA	Charge Radius Experiments with Muonic Atoms	GPSC	gas proportional scintillation counter
CsI	Caesium Iodide	GIAN	Grupo de Instrumentação Atómica e Nuclear
CT	Cyclotron Trap	Hamamatsu	Hamamatsu Photonics
DAQ	Data Acquisition System	LKB	Laboratoire Kastler Brossel
DRIM	Grupo de Detecção de Radiação e Imagiologia Médica	LAAPD	large area avalanche photodiode
ENF	excess noise factor	LED	Light Emitting Diode

LIP	Laboratório de Física Experimental de Partículas	QED	modern Quantum Electrodynamics
		QM	Quantum Mechanics
MIDAS	Maximum Integrated Data Acquisition System	RAL	Rutherford Appleton Laboratory
MPQ	Max Planck Institute	RMD	Radiation Monitoring Devices Inc.
MDE	minimum detectable energy		
MEC	Muon Extraction Channel	RMS	Root Mean Square
NIM	Nuclear Instrumentation Module	RPC	Resistive Plate Chamber
		RT-APD	reach-through avalanche photodiode
QED	Quantum Electrodynamics		
PET	Positron Emission Tomography	SNR	signal to noise ratio
		TDC	Time to Digital Converter
PSI	Paul Scherrer Institute	TOF	time of flight
EG&G	Perkin Elmer Optoelectronics	VME	Versa Module Europa
		WFD	Waveform Digitizer

Chapter 1

Introduction

The small energy difference between the $2S_{1/2}$ and $2P_{1/2}$ levels in the hydrogen atom is known as the Lamb shift. It was first measured by Lamb and Retherford in 1947 [1] and since then the Quantum Electrodynamics (QED) theory of the bound states experienced a series of developments. This small energy difference introduced a discrepancy in the predictions of the Dirac equation and since then theoretical and experimental independent studies have been carried out in order to refine the methods thus obtaining the most precise calculations for the $2S_{1/2} - 2P_{1/2}$ energy difference, the proton charge radius and the Rydberg constant [2–16].

Two fundamental constants given by the Committee on Data for Science and Technology (CODATA) [16], the proton charge radius and the Rydberg constant, are obtained by least square analysis from two different research methods, electron scattering [13–15] and hydrogen spectroscopy [10–12].

The Charge Radius Experiments with Muonic Atoms (CREMA) collaboration started in the late 1990s [17] with the main aim of determining the Lamb shift in muonic hydrogen by means of laser spectroscopy, thus establishing another independent method to access these fundamental constants. It is composed by members from Paul Scherrer Institute (PSI), Swiss Federal Institute of Technology Zurich (ETH), Max Planck Institute (MPQ), Laboratoire Kastler Brossel (LKB),

University of Coimbra, University of Aveiro, University of Fribourg, University of Stuttgart and University of Taiwan. Three data-taking campaigns on muonic hydrogen took place in 2003, 2007 and 2009. The 2009 data revealed the best results ever to be achieved by the collaboration. The transition between energy levels, $2S_{1/2}^{F=1} - 2P_{3/2}^{F=2}$, in muonic hydrogen was measured, 202.3706 (23) meV [9]. The 2S-hyperfine splitting was also obtained, 22.8089 (51) meV. The corresponding proton charge radius extracted was $r_p = 0.84087$ (39) fm after a careful analysis, which is 1.7 times more precise than the one obtained after the experiment and reported in [7] and 7.0σ discrepant from the CODATA value. The Rydberg constant is deduced as $R_\infty = 3.289841960251$ (3) $\times 10^{15}$ Hz/c with a relative accuracy of $u_r = 1.0 \times 10^{-12}$, also 7 standard deviations away from the CODATA value, yet 5 times more precise [16]. However, since the muonic result obtained is so inconsistent in comparison with the other two results (obtained by electron scattering and hydrogen spectroscopy methods), and also because of the assumption that both particles, muon and electron, interact with the proton exactly in the same way, CODATA did not yet integrate these calculations in the proton radius and consequently in the Rydberg constant [16]. The origin of the discrepancy should first be better understood.

Since these muonic hydrogen Lamb shift measurements, a puzzle that goes beyond the proton radius has started in the scientific community. The discrepancy obtained took a central role and gathered efforts from both theoretical and experimental sides. Independent methods have been carried out in order to identify, understand and explain the possible solutions to solve the proton radius puzzle [3, 8, 9, 18–21].

A new experiment was planned by the CREMA Collaboration at Paul Scherrer Institute (PSI), aiming to measure with high precision several transitions frequencies $2S - 2P$ in muonic helium ions ($\mu^4\text{He}^+$ and $\mu^3\text{He}^+$), and consequently to determine the ^4He (α -particle) and ^3He root mean square (RMS) nuclear charge radii with 3×10^{-4} relative accuracy. In addition, the fine and hyperfine structure may be better understood. The radius of the helion magnetic moment distribution may also be determined. It is also expected that the results will lead to a better understanding

of the proton radius discrepancy, providing more relevant information to solve the proton radius puzzle.

The principle of the experiment is based on laser spectroscopy, laser pulses induce the muon $2S - 2P$ transition, the de-excitation $2P - 1S$ is immediately followed by the emission of an 8.2 keV X-ray, which will be detected by avalanche photodiodes. The number of X-rays in time-coincidence with the laser pulses as a function of the laser wavelength will give a resonance curve, from which the Lamb shift will be determined [22].

The main motivation behind this thesis is the research, development and operation of the X-ray detection system for the muonic helium Lamb shift experiment. The avalanche photodiodes used in the previous experiment (muonic hydrogen Lamb shift) are from Radiation Monitoring Devices Inc. (RMD), with $14 \times 14 \text{ mm}^2$ active area. They are optimal for the detection of 1.9 keV X-rays, although they are not as good for 8.2 keV X-rays, since there is a drop in the detection efficiency, from over 90% to about 40% (without considering the effect of the X-ray incident angle in the muonic helium experiment). More recently, Hamamatsu Photonics developed RT-APDs with a much thicker depletion layer [23, 24]. These APDs present a much higher detection efficiency for 8 keV X-rays (above 90%). At the same time, they have shown better energy resolution and lower background plateau in the amplitude distributions [23, 24].

A detailed characterization of RT-APDs provided by Hamamatsu Photonics (rectangular $3 \times 5 \text{ mm}^2$ and square $5 \times 5 \text{ mm}^2$) was performed. The studies include the determination of the gain and energy resolution as a function of the X-ray energy. The operational characteristics of the RT-APDs, such as gain, energy resolution and risetime, have been investigated in order to optimize their performance for the detection of 8 keV X-rays. Furthermore, a study to compare the several energy resolution contributions was carried out, specifically by evaluating the RT-APD response to visible light pulses.

This thesis is organized in 8 chapters. Chapter 2 presents the theoretical background to understand the experiment as a whole. A short background review on

the theory of the Lamb shift is provided in the first section. A brief summary regarding muonic atoms is presented, including the contributions to the muonic helium Lamb shift compared to the electronic helium contributions. A final section shows the X-ray detection system milestones achieved since the beginning of the Collaboration.

Chapter 3 offers a comprehensive yet straightforward compilation concerning the semiconductor detectors used in the experimental studies. In the first section there is information about interaction of radiation with matter, which is important to understand the processes involved in photon detection. The detectors that can be used in the muonic helium Lamb shift experiment and their particular advantages and drawbacks are highlighted, in particular alternatives to conventional APDs, such as RT-APDs and cadmium zinc tellurium (CZT) detectors. The last sections are dedicated to avalanche photodiodes. The basic operational characteristics are presented, as well as the working principle.

Chapter 4 is dedicated to the muonic helium Lamb shift experiment apparatus. The principle and the set up of the experiment are presented. The most important parts of the experimental system are described.

The following two chapters show the studies carried out for the selection of the detectors to be used during the experiment. In chapter 5, a detailed study about RT-APDs from Hamamatsu Photonics is presented. These APDs present a wide depletion region, increasing their efficiency for 8.2 keV X-rays when compared to the previous APDs used during the muonic hydrogen experiment. The experimental setup used and all the relevant operational parameters, such as gain, energy resolution, non-linearity and temperature dependence, are presented. The response of the reach-through avalanche photodiode in X-ray detection, in terms of energy resolution and minimum detectable energy was characterized. The different contributions to the energy resolution were evaluated.

Chapter 6 shows the detectors selected for the muonic helium experiment and presently being used. Their advantages against RT-APDs and a detailed study on their operation in 8.2 keV X-ray detection is explored. The previous pre-amplifiers

were replaced in order to provide faster pulses. The new pre-amplifier system was studied and its performance evaluated. The results are presented in the last section of this chapter.

In chapter 7 preliminary results are shown. Since the experiment was still taking place at the moment when this thesis is being written, results are focused on the performance of the X-ray detectors during beam time. Energy and time distributions are shown for all hits in all APDs. Finally, the time spectra for X-rays from the $2P - 1S$ transition, with the laser off and on, are disclosed.

Last chapter is the conclusion of the work performed under this thesis, where the main achievements are outlined. The future work to be done is delineated, in addition to a forecast of other options to be considered after a subsequent data analysis of the muonic helium Lamb shift experiment.

Chapter 2

Muonic Helium Experiment Background

This chapter introduces a simple and overall approach of fundamental concepts concerning the Lamb shift theory, muonic atoms and X-ray detectors for the muonic helium experiment. The first section offers a digest of the theory of the Lamb shift. In section 2.2 there is an additional emphasis on muonic atoms, hydrogen and helium, which allow a better understanding of the Lamb shift in muonic helium and the goals of the experiment. The last section is dedicated to the X-ray detectors needed for the experiment, encompassing a retrospective of the work developed since the beginning of the CREMA Collaboration, the prototypes investigated and their principal characteristics.

2.1 The Lamb Shift in the Hydrogen Atom and Respective Contributions

Precision spectroscopy of light atoms leads to precise measurements on modern Quantum Electrodynamics (QED) and to the determination of fundamental constants, as well as other properties of atomic nuclei. The hydrogen atom has always played a

central role due to its simple atomic system, made simply of one negative charge (electron) and one positive charge (proton) [25]. The hydrogen atom permitted the development of Quantum Mechanics (QM), proved several fundamental physical theories, and refinement studies triggered the development of the QED theory [26]. "Hydrogen-like" atoms, which have one electron, have raised interest in the scientific community mostly because they allowed solving the Schrödinger equation and their structure could be discussed with precision, thus promoting a set of concepts that could be extrapolated and applied to both many-electron atoms and complex structures [25].

Long before Schrödinger could demonstrate the energy split in the hydrogen atom levels, Johann Balmer, Johannes Rydberg and Max Planck, among others, started to experimentally observe and mathematically define the light's wavenumber in vacuum ($1/\lambda_{vac}$) as a function of the principal quantum number (n),

$$\frac{1}{\lambda_{vac}} = R_H \left(\frac{1}{n_1^2} - \frac{1}{n_2^2} \right), \quad (2.1)$$

with $n_1 = 1, 2, \dots$ and $n_2 = n_1 + 1, n_1 + 2, \dots$ and R_H the Rydberg constant for hydrogen and that black bodies emit electromagnetic radiation only as discrete quanta of energy. It was Niels Bohr who successfully explained the Rydberg formula and thus a model of the hydrogen atom was postulated; electrons could only have certain classical motions [25]. He successfully determined the energy difference between different levels,

$$\Delta E = E_2 - E_1 = h\nu, \quad (2.2)$$

where h is the Planck constant and ν the frequency.

Since then, theory has greatly developed through the study of "hydrogen-like" atoms. In 1926, Schrödinger showed in a non-relativistic way that the split in the energy levels had only a principal quantum number (n) contribution, considering the

2.1. The Lamb Shift in the Hydrogen Atom and Respective Contributions

nucleus as a point with infinite mass:

$$E_n = -\frac{mc^2(Z\alpha)^2}{2} \frac{1}{n^2} \quad n = 1, 2, 3, \dots \quad (2.3)$$

where m is the mass of the orbiting particle, c is the speed of light in vacuum, Z is the nuclear charge and α is the fine structure constant.

Dirac in 1928, connected the quantum mechanics theory with the relativistic kinematics, demonstrating and introducing in the previous equation a dependence between the relativistic variation of mass, velocity and spin. This contribution is known as the fine structure (*fs*) of the energy levels, which is dependent on the total angular momentum j . Equation 2.3 with the fine structure integrated and expanded in powers of $(Z\alpha)$ will adopt the form [27]:

$$E_{nj} \simeq E_n \left[1 + \frac{(Z\alpha)^2}{n} \left(\frac{1}{j + \frac{1}{2}} - \frac{3}{4n} \right) + \dots \right]. \quad (2.4)$$

Nonetheless, for energy levels such as $2S_{1/2}$ and $2P_{1/2}$, both having the same binding energy, these states remain degenerate, as shown in figure 2.1.

In 1947, Willis Lamb and Robert Retherford observed a deviation of 1 GHz from the energies predicted by Dirac, for the energy levels $2S_{1/2}$ and $2P_{1/2}$, in the hydrogen atom, as seen in figure 2.1 [1]. This splitting was explained in the same year by Bethe as originating by electron self-interaction [28], and since then more developments in QED theory became more and more frequent.

The hyperfine splitting (*hfs*), another contribution present here, is due to an interaction between the electron angular momentum and the nuclear spin, causing additional splitting in the energy levels. It also needs to be integrated in Dirac's equation, explaining the non-degenerate state level, for instance in $2S_{1/2}$. This is mathematically represented by:

$$\Delta E_{hfs} = \frac{8}{3} \frac{A}{n^3} \frac{F(F+1) - I(I+1) - j(j+1)}{j(j+1)(2I+1)}, \quad (2.5)$$

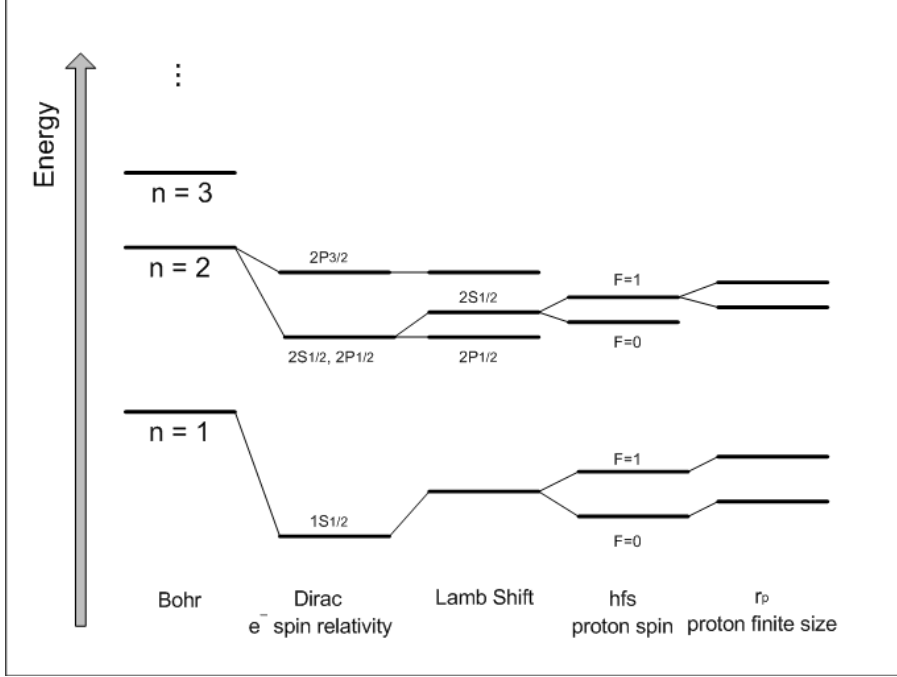


Figure 2.1: Energy levels in the hydrogen atom according to Bohr, Dirac and Lamb theories. The Lamb shift is the energy difference between $2P_{1/2}$ and $2S_{1/2}$ states. The hyperfine splitting and the proton finite size contribution are also shown.

where A is the splitting between the hyperfine levels $F = 1$ and $F = 0$ of the $1S_{1/2}$ state, F is the total angular momentum of the "hydrogen-like" atom ($F = j \oplus I$, \oplus being the quantum sum, I the spin of the nucleus) and l is the electron orbital quantum number [27].

This theoretical background has come a long way, with continuous evolution taking place until today, also thanks to laser technology developments [29]. QED theory has indeed benefited from progress of more precise experiments and theoretical refinements, that allowed for improved precision. Consequently, new improvements and additional corrections in the energy levels are still taking place as a result of quantized electromagnetic field interaction theory [3, 5, 7, 9, 10, 13, 15, 30, 31]. These corrections can be divided in four main groups [7, 27, 32]:

- two-body recoil,

- radiative,
- radiative-recoil,
- nuclear finite size and structure.

The two-body recoil correction is due to the nucleus motion effect and depends on m/M (the recoil parameter, where m is the mass of the orbiting particle and M is the nuclear mass). The radiative corrections take into account the changes of the electromagnetic potential seen by an orbiting particle, depending on parameters such as α and $(Z\alpha)$. The radiative-recoil corrections are expansion terms which depend on parameters such as α , $(Z\alpha)$ and m/M . The last correction is due to the finite nuclear size, which considers the spatial distribution of the nucleus, and to the nuclear polarization, which takes into account the nuclear excitation to virtual excited states inside the nucleus. In what concerns these 4 energy corrections, the second one has a dominant role for the Lamb shift in both electronic and muonic hydrogen experiments. The radiative energy correction is dominated by two types of contributions, the electron self-energy (assuming that orbiting particles do not behave as a point-like particle) and the vacuum polarization (VP), i. e., the virtual production and annihilation of e^+e^- pairs which induces a modification of Coulomb's law at small distances when compared to the electron Compton wavelength [3, 27, 31, 33, 34].

2.2 Muonic Atoms

The Lamb shift in muonic helium shares the same contributions as the hydrogen atom.

The muon is about 200 times heavier than the electron. It means that in muonic atoms the negative muon moves around the nucleus with an atomic Bohr radius about 200 times smaller than in the corresponding electronic atom. Hence the energy levels of muonic atoms suffer a strong influence from the vacuum polarization effect (VP), the nuclear structure (finite nuclear size and nuclear polarizability) and

the relativistic recoil, whereas the electronic atoms are dominated by self-energy effects [3, 22, 31, 34–36]. For instance, the energy levels of S -states are very sensitive to the nuclear finite size (see figure 2.2), thus suffering relevant shifts when compared to P -states. Therefore, muonic atoms represent an exceptional opportunity to determine the root-mean-square (RMS) charge radii of the nuclei and other nuclear properties.

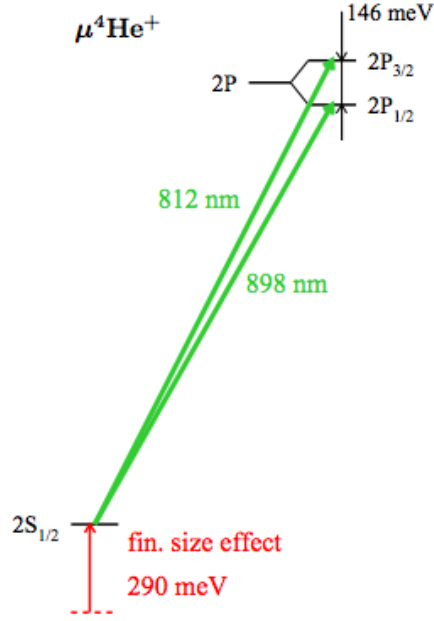


Figure 2.2: Energy levels of $\mu^4\text{He}^+$ [22].

When muonic helium ions are formed, the muons are initially highly excited in a state $11 < n < 15$. Due to selection rules, 98% of them decay promptly to the ground state $1S$ (decaying or interacting weakly with the nucleus) emitting a K -line X-ray and the remaining 2% populate the long-lived $2S$ metastable state [32, 37]. The muonic cascade proceeds via a competition of different collisional processes and radiative transitions. The collisional processes involved are Stark mixing and external Auger effect. The radiative transitions, independent on density and collision energy, also participate in the cascade mechanisms [38]. The first process is due to electric field influences on the nucleus and electrons from neighbouring atoms and molecules. In the

2.2. Muonic Atoms

Auger process, the transition energy is transferred to an electron of the neighbouring atom or molecule, being maximum for $n = 7$.

The lifetime of the $\mu\text{He}^+2\text{S}$ -state is a crucial parameter for the experiment, determining the setup. The muonic helium Lamb shift apparatus, explained in detailed in chapter 4, was thought and designed for a 2S lifetime of $1.4\ \mu\text{s}$ at 30 mbar.

Muonic helium is the second simplest exotic atom after muonic hydrogen. The $\mu^4\text{He}^+$ and $\mu^3\text{He}^+$ ions are the only stable muonic helium isotopes, with 2 and 1 neutrons, respectively. Like in hydrogen, QED tests in He^+ need high precision in the charge radius of helium nuclei, until now provided by electron scattering experiments. For instance, $r(^4\text{He}^+) = 1.681 \pm 0.004\ \text{fm}$ with a relative accuracy of $u_r = 2.5 \times 10^{-3}$ [5].

The principal interest in $\mu^4\text{He}^+$ comes from its characteristics. Since the finite size effect scales with $Z^4 r^2$, where r is the nuclear radius, the $\mu^4\text{He}^+$ energy levels are much more sensitive to bound-state QED corrections when compared to μH , specifically the effect is 20% in $\mu^4\text{He}^+$ compared to 2% in μH . After the good campaign with muonic hydrogen, which generated the proton radius puzzle, it made sense that the next muonic atom to test would be muonic helium. CREMA collaboration decided to measure the $2\text{S} - 2\text{P}$ transitions in $\mu^4\text{He}^+$ and $\mu^3\text{He}^+$ with a precision of 50 ppm. This result, combined with the theoretical predictions, will lead to a determination of the nuclear RMS charge radii with a relative accuracy of 3×10^{-4} , mainly limited by the uncertainty of the nuclear polarization contribution. [19]. The measurement, combined with theoretical and experimental results from helium spectroscopy and electron scattering, will provide valuable support to solve the proton radius puzzle and, in future, improve the bound-state QED in the 1S Lamb shift in He^+ .

The various contributions to the $2\text{S}_{1/2} - 2\text{P}_{1/2}$ energy difference in $\mu^4\text{He}^+$ are summarized in table 2.1. The results obtained were based on [4]. The contributions for $\mu^3\text{He}^+$ are not presented here since more theoretical calculations are needed and at the time of this writing the Lamb shift of the $\mu^3\text{He}^+$ ion was not experimentally measured yet. The weight of the vacuum polarization (VP) from all the contributions is clear. Taking into account all corrections except the nuclear polarizability for $\mu^4\text{He}^+$, the

transition $2S_{1/2} - 2P_{1/2}$ is expected to be [19, 22]:

$$\Delta E(\text{meV}) = 1670.370(10)(600) - 105.322r_{He}^2 + 1.529r_{He}^3 (\text{meV}). \quad (2.6)$$

For $r(^4\text{He}^+) = 1.681(4) \text{ fm}$ [5] the transition is:

$$\Delta E(\text{meV}) = 1380.020(10)^{theor}(600)^{pol}(1420)^{fin.size} (\text{meV}). \quad (2.7)$$

The first, second and third uncertainties are related to "pure" bound-state QED and recoil contributions, nuclear polarizability and the finite size effect, respectively.

2.3 X-ray Detectors for Spectroscopy of Muonic Atoms

To carry out a laser spectroscopy experiment with muonic atoms it is essential to bring together different scientific backgrounds, such as muon beam production and gas targets, laser spectroscopy and cavities, electronic and data acquisition systems, X-ray and electron detectors, as well as theoretical knowledge.

The Grupo de Instrumentação Atômica e Nuclear (GIAN) at the University of Coimbra joined this collaboration in 1999 thanks to their extensive work in the field of gaseous detectors. GIAN became responsible for the development and operation of the X-ray detection system for the muonic hydrogen Lamb shift experiment [17, 39, 40]. Specific requirements of the X-ray detectors had to be met for implementation in the experiment:

- operation under intense magnetic field (5 T) with no performance degradation;
- energy resolution of about 20 % for 2 keV X-rays;
- time resolution better than 50 ns;
- pulse rise time shorter than 500 ns;

Table 2.1: Contributions to the Lamb shift $\Delta E(2P_{1/2} - 2S_{1/2})$ in $\mu^4\text{He}^+$. The value $r(^4\text{He}^+) = 1.681(4) \text{ fm}$ [5] was used to calculate the finite size effect of order $(Z\alpha)^4$ and the nuclear structure contribution of order $(Z\alpha)^5$ [4].

Contributions	ΔE (meV)
One-photon VP contribution, $\alpha(Z\alpha)^2$	1665.782
Two-loop VP contributions in first and second order PT, $\alpha^2(Z\alpha)^2$	15.188
Wichmann-Kroll correction	0.135
Three-loop VP contributions in first and second order PT, $\alpha^3(Z\alpha)^2$	0.138
Relativistic VP effects	-0.203
Hadronic VP	0.223
μ self-energy, μ VP, μ form factor corrections	-11.243
Recoil corrections $(Z\alpha)^4$, $(Z\alpha)^5$, $(Z\alpha)^6$	-0.355
Radiative-recoil corrections	-0.040
Nuclear structure contribution of order $(Z\alpha)^4$: $-105.322 r_{He}^2$	-297.615
Nuclear structure contribution of order $(Z\alpha)^5$: $1.529 r_{He}^3$	7.261
Nuclear structure and one-two-loop VP + higher order nuclear structure	2.357
Nuclear polarizability contribution	3.100
Total splitting	1380.020

- large detection area to maximize the solid angle.

The first prototypes assembled and tested for this purpose were three gas detectors of the type gas proportional scintillation counter (GPSC) [41–43]. One prototype used a microstrip plate coated with a Caesium Iodide (CsI) film operating in pure xenon (GPSC1). Another prototype used the same photosensor, microstrip plate coated with a Caesium Iodide (CsI), but operated in a separate chamber with a quartz window isolating it from a P-10 mixture chamber (GPSC2). The last prototype had an APD as photosensor in a xenon atmosphere (GPSC3). None of them had a drift region to minimize the pulse risetime and time resolution, and to reduce the transverse drift in primary electrons due to the magnetic field present in the experiment. The results achieved after careful optimizations are shown in table 2.2.

Table 2.2: *Relevant characteristics from the 3 GPSC prototypes developed for the muonic hydrogen Lamb shift experiment [42].*

Prototype	MDE (eV)	Amplitude Variation (5 T/0 T)	Energy Resolution 2.3 keV X-ray (0 T— 5 T)		Time Resolution (ns)	Risetime (μ s)
GPSC1	300	-25%	27%	31%	> 200	1.1
GPSC2	50	+1%	27%	27%	30	0.5
GPSC3	40	-8%	18%	26%	25	1.2

With technological advances in the manufacturing of photodiodes in the last decade of the past century, APDs started to be produced with diameters up to 16 mm [44]. They presented gains of a few hundreds and a high disruption voltage (≈ 2 kV) [45]. Several techniques were extensively developed in companies such as Advanced Photonix Inc., Hamamatsu Photonics and RMD in order to produce a large quantity of reliable and homogeneous prototypes [43], in order to be a good option in direct low energy X-ray detection in replacement of gas detectors with

2.3. X-ray Detectors for Spectroscopy of Muonic Atoms

photosensors. Since then, large area APDs have been extensively studied in view of their application in different fields, from high energy physics to medical applications [46–49], as well as for the muonic hydrogen experiment, to be used as low energy X-ray detectors [27, 43, 50–53].

The relative small area of each APD is compensated by the use of arrays of several detectors with a dimension close to the useful detection area. This way all the requirements listed above for the X-ray detection system for the muonic hydrogen experiment were fulfilled. APDs have compact structures and are simple to operate. They are less sensitive to ionizing particles, allowing a complete separation between electrons and X-rays. They can operate under intense magnetic fields with negligible performance degradation for 2 keV X-rays. The pulse shape does not have a relevant dependence on the magnetic field as well. Concerning the rise time, a slight difference between 0 T and 5 T was measured, respectively 20 and 32 ns [43]. These values are far better in comparison with the prototypes from table 2.2, allowing detection of events in time coincidence. The time resolution was determined by coincidence between 5.4 keV X-rays and 835 keV γ -rays both emitted by a ^{54}Mn radioactive source [42, 43]. Values between 10 and 12 ns were obtained, much lower than the gaseous prototypes in table 2.2.

Large area avalanche photodiodes were chosen instead of the gaseous detectors, and since then they have been used as direct X-ray detectors for 1.9 keV X-rays emitted by muonic hydrogen atoms in the Lamb shift experiment. In the first run in 2002, circular LAAPDs from API [50–52] were used, as seen in figure 2.3. Two series of 6 photodiodes were cooled down to -10°C for energy resolution and signal-to-noise ratio improvements [51, 54]. Each LAAPD had a 16 mm diameter and an energy resolution for 1.9 keV X-rays of about 25%.

In the second run in 2003, new LAAPDs with square shape and planar structure from Radiation Monitoring Devices Inc. were used (see figure 2.4).

The main difference of the new prototypes from the previous ones is their square shape, with $13.5 \times 13.5\text{ mm}^2$ active area, delimited by a thin edge of inactive material.

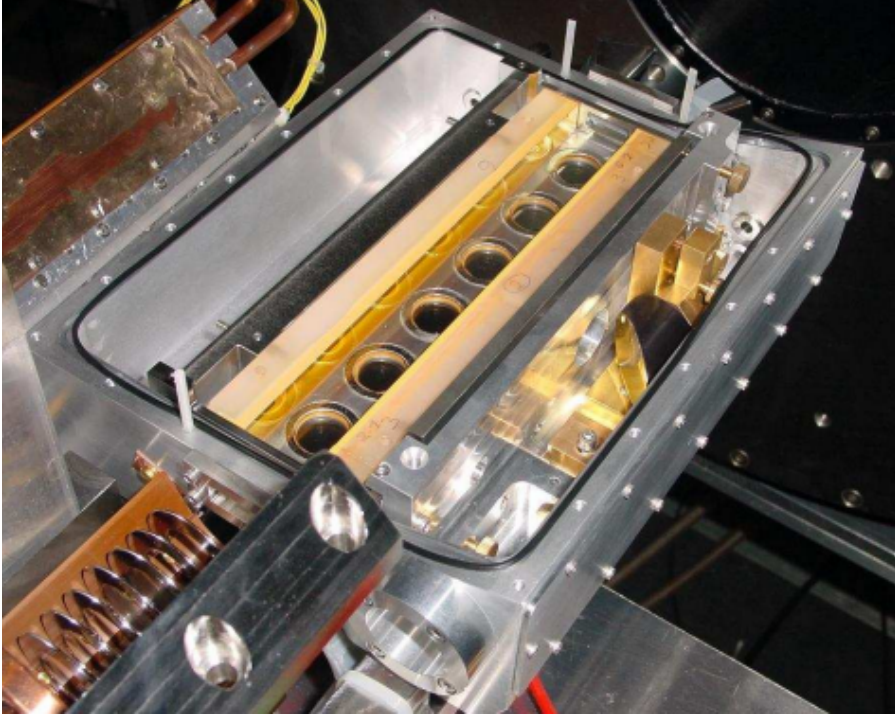


Figure 2.3: LAAPDs from Advanced Photonix Inc. used in 2002 with round shape and 16 mm diameter.

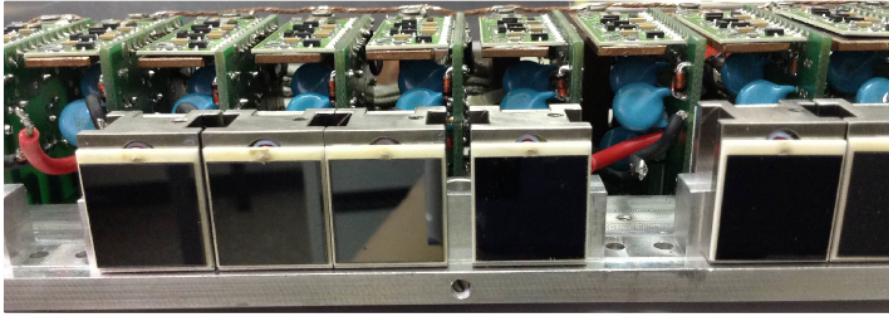


Figure 2.4: LAAPDs from Radiation Monitoring Devices Inc. (RMD) with $13.5 \times 13.5 \text{ mm}^2$ active area used in muonic hydrogen runs since 2003.

This allowed for a significant increase in the useful area, as instead of 6 detectors, 10 new prototypes could be implemented in each array, thus increasing the solid angle for X-ray detection. However, they presented higher dark currents at room temperature, about $2\mu\text{A}$, consequently degrading the energy resolution and the signal-to-noise ratio.

2.3. X-ray Detectors for Spectroscopy of Muonic Atoms

This drawback was overcome by decreasing the temperature to -30°C , thus dropping the dark current for values in the range of $10 - 20\text{ nA}$ [43]. In the subsequent runs, in 2007 and 2009, LAAPDs from RMD were extensively used. They are reverse biased at voltages between 1600 and 1700 V. Typical gains of about 200 are achieved varying from LAAPD to LAAPD. Cooled down to -30°C , they presented for 1.9 keV X-rays an average energy resolution of 30% at FWHM. The time resolution was about 35 ns. The pre-amplifiers used during the muonic hydrogen experiment campaigns are RAL 108A prototypes from Rutherford Appleton Laboratory (RAL) specifically designed as one of the components for a modular amplifier system for the readout of silicon strip detectors. The RAL 108A preamplifier is a low noise charge sensitive device, amplifying negative input signals and giving at its output positive signals [55].

Chapter 3

X-ray Detection with Avalanche Photodiodes

This chapter is intended to give the reader information about the physical processes behind the detectors used in the muonic helium Lamb shift experiment and the main characteristics of avalanche photodiodes. Section 3.1 provides a general description of the processes of interaction of X-rays and charged particles with matter. The second section discusses the possible detectors to be implemented in the muonic helium experiment. In section 3.3, the characteristics of avalanche photodiodes are displayed, in particular their working principle. The operational parameters are showed in the last section.

3.1 Interaction of Radiation with Matter

It is very important to understand how the particles to be detected in the experiment interact and lose energy within the detector's material, as well as the processes involved. The performance and operation of the detector depend on this, since those interactions determine the sensitivity and efficiency of the detector for a specific particle. There are several distinct ways of categorizing particles. They can be

distinguished taking into account their effect on matter, and they can be distinguished between charged and uncharged particle, interacting differently with matter. This is a wide and complex field and the relevant information will be presented here in a straightforward manner, in order to give the reader a fundamental understanding of the most important effects that are originated from ionizing radiation, in particular X-rays, electrons, protons and alpha particles. For further details, beyond the scope of this thesis, see [56–58].

3.1.1 X-rays

When an X-ray photon interacts with matter, several interaction mechanisms can occur. Those mechanisms are determined by the photon energy and by the material atomic number. The most relevant processes are:

- Photoelectric effect,
- Compton scattering,
- Pair production.

Figure 3.1 shows the cross sections⁽¹⁾ in silicon for each of these interaction processes as a function of the photon energy. The photoelectric effect dominates for lower energies, presenting a K-edge⁽²⁾ of 1.84 keV. The Compton Scattering (Incoherent scattering) is relevant for energies from 0.1 to 1 MeV. For higher energies, above 1.02 MeV, the pair production becomes relevant.

The photoelectric effect is an interaction between a single X-ray photon and a bound atomic electron. Since the photon has zero rest mass, all its energy ($h\nu$) is in the form of kinetic energy and will be transferred to the electron, with the photon disappearing in the process. If the energy transferred by the photon is greater than

⁽¹⁾The cross section is essentially a measurement of the probability for an interaction to occur and may be calculated if the form of the basic interaction between the particles is known [57].

⁽²⁾K edge is the energy where the absorption coefficient suffers a sharp rise, which happens when the X-ray energy equals the binding energy of a K-shell electron.

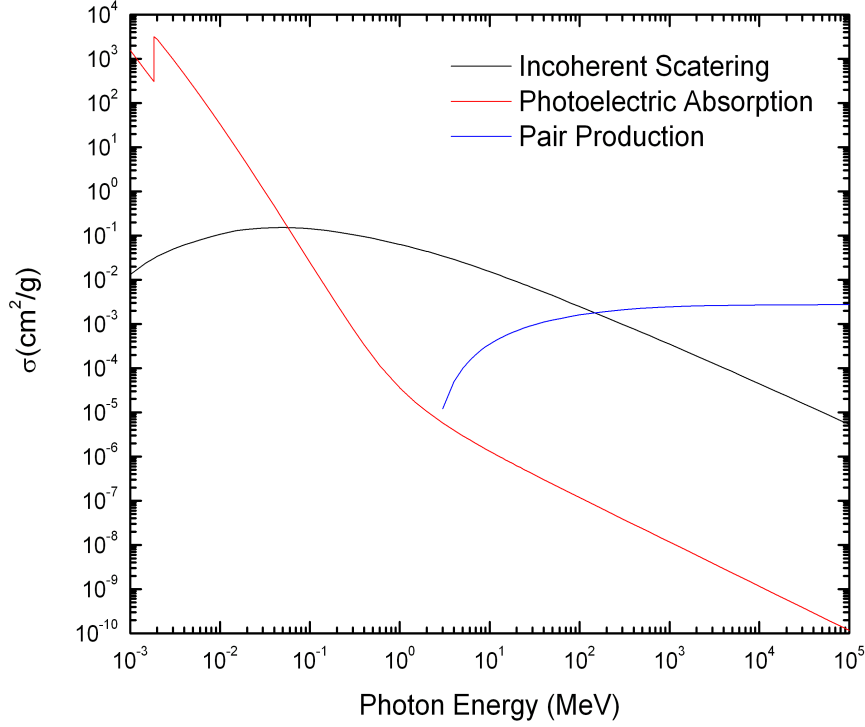


Figure 3.1: Cross sections for several interaction mechanisms as a function of the X-ray energy deposited in Si material.

the electron binding energy (E_b) in the atom, the latter will be ejected as a free electron from the respective shell, with kinetic energy equal to:

$$E_e = h\nu - E_b. \quad (3.1)$$

Only electrons with binding energy smaller than the photon energy can be "kicked out", and those with highest probability are placed in the inner atomic shells. Therefore, the ion is unstable and an electron from a higher energy level is moving down to the unfilled energy level. Two processes can arise here: either one electron from an outside shell is moving from its shell directly to fill the gap, or a cascade

event will take place, the K-shell gap is then refilled by a L-shell electron, and so on. In these processes, since an electron from a higher energy shell is moving to a lower energy level, there is an excess of energy, so either photons are produced (called characteristic radiation) or other electrons are ejected from their shells (known as Auger electrons).

In Compton scattering, the interaction between the photon and the electron will lead to photon deflection through an angle (θ) from the initial direction and the electron is removed from its shell. The energy of the deflected photon is reduced and the remaining energy will be given to the electron. The new photon energy is given by:

$$h\nu' = \frac{h\nu}{1 + \frac{h\nu}{m_0c^2}(1 - \cos \theta)}, \quad (3.2)$$

where m_0c^2 is the electron rest-mass energy. If the angle θ is small, less energy is transferred; otherwise, for higher angles, more energy will be transferred.

The pair production effect is an interaction between a photon and the nucleus. However, it will take place only when the photon exceeds twice the rest-mass energy of an electron. The photon will be absorbed, producing a positron-electron pair, with the subsequent positron annihilation originating two photons. This effect is significant for higher photon energies.

Within the scope of this thesis, the last two effects are almost negligible, since the X-ray energy involved is 8.2 keV, well below 100 keV, where Compton scattering starts to dominate over the photoelectric absorption [56–58].

3.1.2 Charged Particles

When charged particles such as electrons and positrons, protons, alpha particles, muons, heavy ions, among others, are passing through matter, they lose energy and may suffer a deflection from their initial directions. However, these mechanisms are not the same as for X-rays (uncharged particles), and they may also differ for light

3.1. Interaction of Radiation with Matter

charged particles (such as electrons) and heavy charged particles (such as protons). Because of this, they will be treated separately in this thesis.

For heavy charged particles, the interactions that are more likely to occur are Coulomb interactions with atomic electrons (inelastic interaction), even if other interactions with the atomic nucleus may occur. The charged particle interactions with many atomic electrons depend on the distance between the particle and the electrons, and may lead to the atom's excitation or ionization. Due to the huge mass difference between the two interacting particles, the heavy charged particle will not lose all the energy in one collision, but instead will need a large number of interactions with electrons from the medium alongside its path to lose all its energy and to stop. This behaviour is represented as the *linear stopping power*, S , and it is given by the Bethe-Bloch formula:

$$S = -\frac{dE}{dx} = \frac{4\pi e^4 z^2}{m_0 v^2} N B, \quad (3.3)$$

where

$$B \equiv Z \left[\ln \frac{2m_0 v^2}{I} - \ln \left(1 - \frac{v^2}{c^2} \right) - \frac{v^2}{c^2} \right], \quad (3.4)$$

v and ze being the velocity and charge of the primary particle, m_0 and e the electron rest mass and charge, N and Z the density number and the atomic number of the absorber atoms and c the velocity of light.

The way heavy charged particles lose energy through the material is a well-known process described by *the Bragg curve*. It is characterized by a small energy loss in the beginning of the track, increasing slightly with the penetration in the material until it reaches a maximum, stopping finally. The heavy charged particles have a finite and almost straight range along their way (see figure 3.2), in a specific material and, due to their large mass, they will suffer almost no deflection [56–58].

Fast electrons, also known as β particles, interact with matter also through Coulomb interactions like heavy charged particles. However, other relevant interactions need to be taken into account, such as radiative processes consisting of an energy loss where *bremsstrahlung* radiation is generated. Therefore, the equation

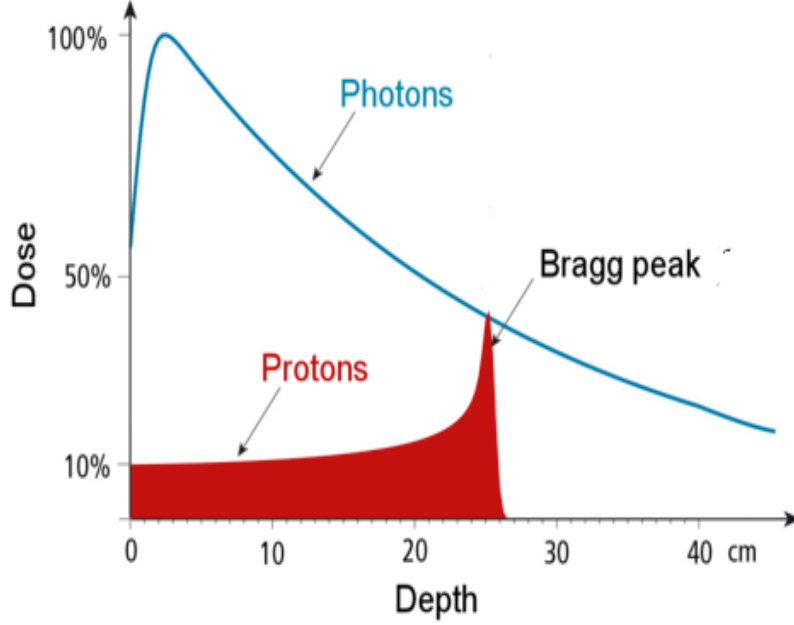


Figure 3.2: Relative dose deposited as a function depth along a non specific material for protons and X-ray photons [59].

for the *stopping power* will have two parameters related to collisional and radiative processes:

$$\frac{dE}{dx} = \left(\frac{dE}{dx} \right)_c + \left(\frac{dE}{dx} \right)_r, \quad (3.5)$$

where the collisional parameter for electrons has the form:

$$-\left(\frac{dE}{dx} \right)_c = \frac{2\pi e^4 N Z}{m_0 v^2} \left(\ln \frac{m_0 v^2 E}{2 I^2 (1 - \beta^2)} - (\ln 2)(2\sqrt{1 - \beta^2} - 1 + \beta^2) + (1 - \beta^2) + \frac{1}{8} \left(1 - \sqrt{1 - \beta^2} \right)^2 \right), \quad (3.6)$$

and the radiative parameter is described by:

$$-\left(\frac{dE}{dx} \right)_r = \frac{N E Z (Z + 1) e^4}{137 m_0^2 c^4} \left(4 \ln \frac{2 E}{m_0 c^2} - \frac{4}{3} \right), \quad (3.7)$$

3.2. X-ray Detection

where $\beta \equiv v/c$ and the other elements are already described in equation 3.3. Unlike what happens with heavy charged particles, since β particles have masses equal to atomic electrons, larger deflection angles and tortuous path along their tracks will take place.

Nevertheless, since the nuclear radius (about 10^{-14}m) is much smaller than the atomic radius (10^{-10}m), the ratio between the number of interactions with atomic electrons and the number of interactions with the nucleus is of the order of 10^8 , meaning that the first is the major process of energy loss for charged particles [56–58].

3.2 X-ray Detection

There is a vast diversity of X-ray detectors, depending on the specific application: count rate measurements, total flux, single photon counting, energy, position or time determination of each X-ray photon. The first prototypes to be evaluated for experiments with muonic atoms were gas proportional scintillation counters. The idea of using GPSC was rapidly set aside due to technical and mechanical reasons. The place where the high voltage was applied is at the entrance of the radiation window, repelling the muons and preventing them from entering the target. On the other hand, the detector time response was not fast. At that time these drawbacks were considered limitation factors, which led to searching for other types of detectors to replace GPSCs, in particular solid state detectors due to their compactness. The general and most relevant properties of the different detectors are listed in table 3.1. APDs show the lowest dead time and the maximum count rate capability from all detectors. In comparison with gas ionization and scintillation detectors the energy resolution is better. The energy range of detection for APDs is the same as for gas ionization and proportional detectors; nonetheless, their range is much smaller than the range of scintillation and HPGe detectors, which can detect particle energies from 1 to 10.000 keV. Therefore, since there is always need to compromise and find

a balance between the application's purpose and the detector characteristics, APDs present very good properties for different detection applications.

Table 3.1: *Relevant properties of different X-ray detectors. The third column quotes typical relative energy resolutions (FWHM) for 8 keV X-rays [60].*

Detector	Energy Range(keV)	Resolution (%)	Dead time/event (μs)	Maximum count rate (s^{-1})
Gas ionization (current mode)	0.2 - 50	20	0.2	10^7
GPSC	0.2 - 50	15	0.2	10^6
Scintillation [NaI(Tl)]	3 - 10.000	40	0.25	2×10^6
Energy-resolving semiconductor (HPGe)	1 - 10.000	10	0.5 - 30	2×10^5
Avalanche photodiodes	0.1 - 50	20	0.01	10^8

In the muonic hydrogen Lamb shift experiment the detectors used, for 1.9 keV X-rays, were avalanche photodiode since they matched the above mentioned constraints. At the same time, they are insensitive to intense magnetic fields, among other useful characteristics. However, for 8 keV X-rays they present a detection efficiency of only 40% (without considering the effect of the X-ray incident angle), comparing with 90% efficiency for 2 keV X-rays. Alternative detectors for the muonic helium Lamb shift experiment were searched.

One alternative could be the use of scintillation detectors coupled to photomultiplier tubes. They have competitive characteristics in comparison to the APD [45, 48], such as a larger detection area and higher internal gain, although the PMT volume and sensitivity to intense magnetic fields are real drawbacks. Other possible substitutes

3.2. X-ray Detection

of standard APDs as 8 keV X-rays detectors are reach-through avalanche photodiode (RT-APD) and cadmium zinc tellurium (CZT) detectors.

CZT and CdTe detectors are compound semiconductor devices developed to detect charged and uncharged particles with applications in several fields, from nuclear medicine imaging and hard X-ray astronomy to gamma-ray spectroscopy, over a vast temperature range (-20°C to 40°C) [61–65]. They have a very high linear coefficient, thus allowing high detection efficiency in a small volume and low leakage currents, which provides low electronic noise level at room temperature. This makes them attractive for X-ray and gamma-ray spectroscopy [64]. There is also the possibility of producing configurations with particular geometries incorporated, such as the size of the collecting electrodes, which is an important advantage over other detectors. There are CZT and CdTe prototypes available in the market. For instance, for an incident photon with energy of 8 keV, the efficiency of a 1 mm thick CdTe device is almost 100 % [65]. The results achieved with these solid-state detectors have shown much better energy resolution than scintillation detectors [63], and studies targeted for medical applications at room temperature revealed an energy resolution of 5 % and a good photopeak efficiency, for a photon energy of 140 keV. For an energy of 122 keV, an energy resolution of 3.6 % was obtained, together with very high photopeak efficiency [62]. Other studies aiming to find a viable alternative to Si and Ge semiconductors working at room temperature, achieved for 5.9 keV an energy resolution of 311 eV at FWHM (5.3 %) at -37°C and 1500 eV at FWHM (25.4 %) at 20°C [64]. They also showed symmetric photopeaks in the measured energy-loss spectra for energies below 50 keV. The detector showed in general a uniform spatial response, with few localized areas presenting non-uniformities. However, the manufacturing process of these detectors is complex, and they present a considerable number of critical steps which may compromise the detector performance. Another drawback is the material itself, since it is necessary to guarantee homogeneity and low defect density to minimize the leakage currents and short circuits between the contacts, as well as to ensure good charge transport. Another characteristic to take

into account in these detectors is the hole tailing effect, which introduces a pulse height loss in the measured signal due to the dependence of the amplitude with the depth of interaction, decreasing with increasing depth. For more details about these detectors, see [61–67].

In APDs, X-rays are absorbed in silicon with an average absorption length which varies with the photon energy. Most X-rays absorbed in the Si material are converted into electron-hole pairs. However, the variation of the X-ray interaction probability at different depths in the depletion region will lead to partial amplification, consequently affecting the energy linearity of the detector. The X-ray absorption length dependence on photon energy will affect the detector's efficiency [46, 68]. Reach-through avalanche photodiodes are regular APDs with a thicker depletion layer, which makes them more efficient for higher energies [23, 69]. The detection efficiency is a critical parameter for the muonic helium Lamb shift experiment, where 8 keV X-rays need to be detected with the highest efficiency possible, as well as with good energy resolution. These detectors have been used for different applications such as X-ray diffraction experiments, optical communications, read-out of scintillation in gamma-ray detectors, X-ray/gamma-ray imaging spectrometers, and as soft X-ray detectors [23, 24, 69, 70]. A RT-APD with 3 mm diameter and 130 μm depletion layer has shown an energy resolution of 6.4% (FWHM) for 5.9 keV photons and a minimum detectable energy of about 0.3 keV at -20°C [23]. In what concerns timing properties, the RT-APD has shown excellent results in comparison to fast PMTs. It also presented good counting rate capability. The output count rate loss was less than 10% for an input rate of approximately 10^7 photons s^{-1} . The main disadvantage of these detectors is the manufacturing process, which is not reliable thus compromising the silicon wafer uniformity and consequently impairing the detector overall performance.

The APDs used in the muonic hydrogen experiment were first tested, in particular the determination of their quantum efficiency for 8 keV X-rays. Then, two RT-APD prototypes from Hamamatsu Photonics with square and rectangular shapes ($5 \times 5 \text{ mm}^2$

and $3 \times 5 \text{ mm}^2$ active areas) were tested in detail for 8 keV X-ray spectroscopy. Since the results with the APDs were relatively good, the study of CZT detectors was discarded for this experiment.

3.3 Avalanche Photodiodes

Avalanche photodiodes are semiconductor devices combining the advantages of conventional photodiodes and photomultiplier tubes. That was the main reason behind a growing interest in them during the decade of 1990. They are nowadays spread across various application fields, from nuclear to particle physics and medicine, as direct X-ray detectors or coupled to scintillators [48, 49, 52, 53, 71–77].

APDs are monolithic devices made of silicon material with p-n junctions exploiting the photoelectric effect to convert photons into electron-hole pairs. The p-n junction is reverse bias polarized at both ends of the Si wafer. The main difference from PIN diodes is the existence of a very high electric field region where the free charge carriers, when crossing it, acquire enough energy to produce more electron-hole pairs in an avalanche process. This way, a signal gain arises. This is the main advantage of APDs over PIN diodes as detectors with high signal-to-noise ratio. Other advantages of APD are their fast response, compact and rugged structure, low power consumption and sensitivity to different radiation types. These properties make them suitable for a wide range of applications. There are currently four main companies manufacturing APDs: Hamamatsu Photonics, Advanced Photonix Inc. (API), Radiation Monitoring Devices Inc. (RMD) and Perkin Elmer Optoelectronics (EG&G), although their research and development continues running in industry and in the academy.

3.3.1 Operation Principle

The APD working principle is based on photon conversion into charge carriers in the depletion region (active volume), with subsequent multiplication in an avalanche

process via impact ionization. The active volume is composed essentially by two regions with different electric fields intensities, the absorption region (Ab) and the multiplication region (Av), as seen in figure 3.3 [78, 79]. The p-n junction plays the key role in the photon absorption and electron-hole pair multiplication. A regular Si APD consists of a p region positively doped and a n region negatively doped sandwiching a neutral charge area, which is the depletion region (also known as π -region) [80]. Depending on the doping material (p-type or n-type) and their concentrations, one will have an acceptor or donor semiconductor. The acceptor will have free positive charges in the bulk of the material, and the donor will have more negative charges and may donate them to the material bulk. For example, the main difference between an APD and a RT-APD is the width of the depletion region: the first presents a width of about $50\text{ }\mu\text{m}$, the latter approximately $130\text{ }\mu\text{m}$. There are different geometrical and layer configurations depending from company to company. Figure 3.3 shows one possible APD scheme configuration adapted from [81]. The dimensions in the picture are not in scale.

In the front surface of the APD there is a SiO_2 layer, which is used to prevent the detector from high dark currents. An X-ray photon absorbed in the absorption region (Ab) or depletion region produces a fast photoelectron, which slows down in successive collisions, resulting in many electron-hole pairs, with an average energy of 3.62 eV deposited per electron-hole pair. This zone is characterized by a low electric field, which increases slowly with depth, being responsible for separating the holes and electrons generated and to redirect them towards the respective electrodes. However, before arriving, the electrons will pass through an intense electric field region, the avalanche region (Av), where charges will be multiplied in successive collisions by impact ionization [43, 58, 73, 78]. The average absorption length for incident X-rays depends strongly on the photon energy [43, 48, 49, 53]. For instance, for 8 keV X-rays, the average absorption length is about $70\text{ }\mu\text{m}$, when compared to $1.7\text{ }\mu\text{m}$, $30\text{ }\mu\text{m}$ and $150\text{ }\mu\text{m}$ for 2 keV , 6 keV and 10 keV , respectively [82]. When a photon interacts with the semiconductor bulk, three different and distinct phenomena can

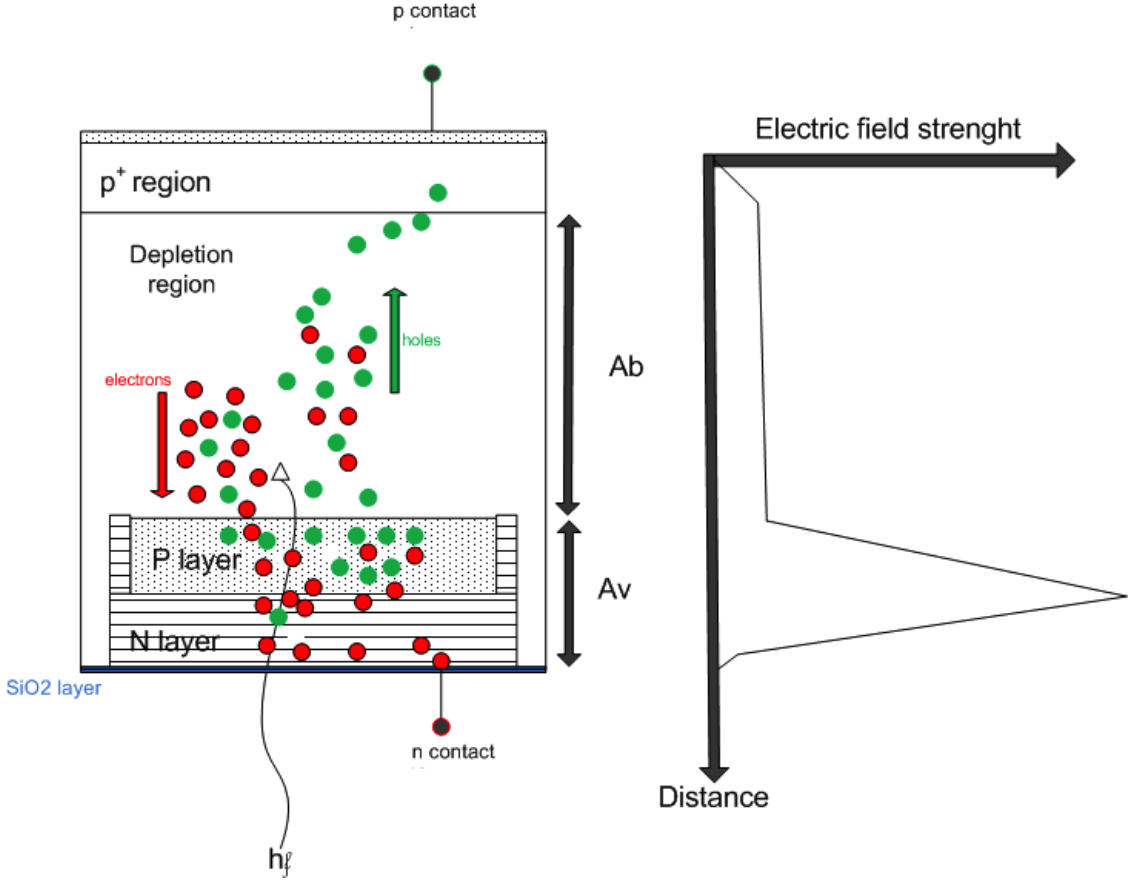


Figure 3.3: Schematic of the RT-APD structure and the electric field strength in the different regions (Ab -absorption region; Av -Avalanche region). The depletion region is around the p-n junction. The red circles represent the electrons and the green circles the holes. The arrows, red and green, indicate the direction of the charges. The picture is not in a real scale. Adapted from [81].

happen: the lattice excitation (when incident radiation deposits energy increasing the lattice vibrations), ionization (when photon produces an electron-hole pair), or atomic displacement (non-ionizing phenomenon causing bulk damage by radiation). Within the scope of this thesis, only the second process is useful. Nevertheless, the lattice excitation poses a significant contribution to the statistics of electron-hole pair production. The average energy needed to create an electron-hole pair in silicon (3.62 eV) does not depend on the type of radiation detected. The ionization

process is similar to gas detectors, although it is the low average energy needed for the electron-hole pair creation that makes the semiconductor interesting. In gases, the average energy is approximately 4 to 8 times higher than in semiconductors. Thus, the number of charge carriers is much higher in semiconductors, making them superior in what concerns resolution and sensitivity [58, 78, 79]. But even if the semiconductor has a better performance, it is still far from the ideal detector. The impurities and crystal imperfections cause additional production of electron-hole pairs, which may cause electron recombination through two processes, band or trap recombination, thus introducing non-linearities in the response of the detectors [58, 78].

In these detectors, the pulse amplitude is proportional to the energy absorbed in silicon. In the end, one will have an energy spectrum to analyse.

3.3.2 Operational Characteristics

The main basic operational characteristics in detectors in general, and APDs in particular, are the quantum efficiency, gain, energy resolution, noise level and time response.

Detection efficiency may be defined as the ratio between the number of electron-hole pairs generated and the number of incident photons in the detector active area. To achieve the maximum detection efficiency, photons should be absorbed only in the absorption layer, creating electron-hole pairs that are fully amplified and have a fast time response due to the electric field applied. However, some photons are absorbed before the absorption region and others are absorbed directly in the avalanche zone. In the first case, delayed charges will be originated since there is a residual electric field that is not strong enough to rapidly transport them to the edge of the absorption zone. Some traps may also exist, holding electrons for long periods, thus causing a reduction in the amplitude of the current pulse, and consequently a reduction in the output signal amplitude. If photons are absorbed in the avalanche zone, they will just be partially amplified, originating pulses with lower amplitude but fast response.

3.3. Avalanche Photodiodes

In practice, photons absorbed in these two regions will create low energy tails in the amplitude distributions, an effect that deviates the APD output pulse amplitude distribution from a Gaussian curve [43, 58, 78]. It is also perceptible from the above that the time resolution is strongly dependent on the X-ray interaction point.

The energy spectrum will be highly affected by noise. As a consequence, the Gaussian distribution will be widened, thus degrading the energy resolution. This is one of the key parameters in spectroscopy applications.

Since APDs were designed to operate under a reverse bias voltage at low light levels, their sensitivity is strongly limited by the noise. The main noise sources are:

- Leakage currents,
- Excess noise factor,
- Thermal noise.

The leakage current is a random fluctuation following Poisson statistics. In APDs the current has two components: the surface leakage current (I_{DS}) generated in the interface between the p-n junction and the SiO_2 layer, and the bulk leakage current (I_{DB}) which is multiplied by the gain (G) and is generated inside the silicon volume. The leakage current (I_D) can be expressed in terms of these components

$$I_D = I_{DS} + I_{DB}.G \quad (3.8)$$

There is another contribution to the noise related to the avalanche process itself, which is the excess noise factor (F). Even if the reverse bias applied is constant, thus keeping the gain constant due to the statistical nature of the multiplication process, the number of generated carriers is not uniform, thus degrading the detector's overall performance. This parameter is expressed by:

$$F = k_{eff}.G + (1 - k_{eff}) \left(2 - \frac{1}{G} \right), \quad (3.9)$$

where k_{eff} is the ratio of electron and hole ionization coefficients, and can be determined experimentally using the model developed by McIntyre [83].

The thermal noise is the noise related with the output circuitry, mainly generated in the preamplifier due to thermal agitations of charge carriers and is given by:

$$\langle V_N \rangle = \sqrt{\frac{4k_B T}{R_{eq}}}, \quad (3.10)$$

where k_B is the Boltzmann constant (1.38×10^{-23} J/K), T the absolute temperature (in K), and $R_{eq} = 2/3g_m$ the equivalent resistance for the junction FET employed in charge-sensitive preamplifiers used with semiconductor detectors and being g_m the FET mutual conductance [84]. Other contributions, such as the FET capacitance, its input current and the detector's polarization resistance, contribute to thermal noise, although their weight is not relevant when compared to the equivalent resistance [43, 53, 73].

The gain depends strongly on temperature and on the electric field applied in the multiplication region. The exponential gain dependence with bias voltage is well known. However, there is a voltage limit where the gain is maximum. When exceeding this value, the output signal ceases to be proportional to the amount of incident radiation, originating a device disruption. What occurs in this high gain region is a positive feedback from hole-induced ionization just after the multiplication region, resulting in an avalanche almost as high as the one of the primary avalanche [43, 58, 73]. In what concerns temperature, for a constant bias voltage, the gain drops with the increase in temperature, due to an energy loss interaction of electrons with phonons from the crystal lattice. It is then important to stabilize the operational temperature and voltage in order to have a constant output [43, 58, 73, 78].

The energy resolution is generally defined, for a monoenergetic radiation source, as the FWHM of the peak detected in a pulse height distribution, relatively to its centroid, H_0 , assuming no background on top of which the peak is superimposed [58].

3.3. Avalanche Photodiodes

In mathematical terms, it is presented as:

$$Res = \frac{FWHM}{H_0} = \frac{2.35K\sqrt{N}}{KN} = \frac{2.35}{\sqrt{N}}, \quad (3.11)$$

where FWHM is the full width at half maximum, N is the total number of charge carriers and K is a proportional constant [58].

A detector with “good resolution” is the one that has the width of the distribution as low as possible, revealing a superior detector performance. In other words, a detector with good resolution would have as many charge carriers generated per event as possible.

APDs belong to the semiconductor detector’s family which are very popular due to their high amount of charge carriers generated. However, some contributions lead to the peak enlargement, such as statistical fluctuations, gain non-uniformities and detector noise, all explained in detail in chapter 5.

Depending on the type of radiation detected, for example light or X-rays, different contributions to the energy resolution need to be taken into account, since the absorption process of the radiation is quite different within the silicon wafer. Thus, since for X-rays it is a point-like absorption mechanism, whereas in light it is spread all over the APD volume averaging the total fluctuations, some considerations need to be understood and considered.

The detector’s time response is determined by the transit time of the carriers in the depletion region and by the R_{eq} and C_T constant from the pre-amplifier. The carrier’s velocity is dependent on the electric field strength. Ideally, the velocity is higher for a higher electric field; however, there is a maximum value in the voltage applied before rupture, as explained before. The ideal C_T value, given by the total effective capacitance in the pre-amplifier input (including the detector and the FET input capacitance) and the R_{eq} value, should be as short as possible, and provide a higher system cutoff frequency. The best time response can be achieved by increasing the depletion region’s thickness and selecting the R_{eq} and C_T values in accordance with the

detectors ones. It is evident that a compromise should be taken. Another phenomenon that happens in the avalanche region is that charge carriers will successively collide with the crystal lattice along their path, taking longer to travel the same distance in the depletion region. As mentioned before, if the photons are absorbed outside the absorption layer, which is characterized by a residual electric field, it will cause not fully amplified and delayed pulses, degrading the detector's time response [58, 79].

Chapter 4

Muonic Helium Lamb Shift

Experiment: Principle and Apparatus

The principle of the muonic helium Lamb shift experiment consists on measuring through laser spectroscopy the transition from the $2S$ metastable state to the $2P$ state in muonic helium ions, as seen in figure 4.1.

A low energy negative muon beam is stopped in a helium gas volume at low pressure, producing highly excited He^+ ions. The majority of these ions (about 98%) de-excite rapidly to the $1S$ ground state, promptly emitting X-rays, but a small fraction (2%) remains in the long-lived $2S$ state. A short laser pulse with a wavelength tunable in the region of 800 – 970 nm is sent to a mirror cavity involving the gas volume after the muon stops in the target, inducing the $2S - 2P$ transition. Atoms in the $2P$ state promptly de-excite to the ground state, emitting 8.2 keV X-rays in time-coincidence with the laser pulse. The laser-induced events are determined as a function of the laser wavelength, originating a resonance curve that determines the Lamb shift [7, 32]. There are two essential parameters to take into account in order

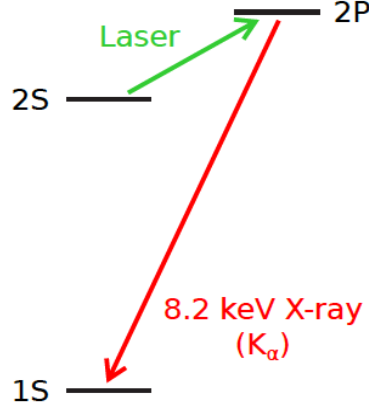


Figure 4.1: Principle of excitation for the $2S - 2P$ transition. A short laser pulse corresponding to the $2S - 2P$ transition frequency is sent to a mirror cavity involving the gas volume and induces the $2S - 2P$ transition from the fraction of muons (2 %) remaining in the long-lived $2S$ state. The atom deexcites to the ground state emitting 8.2 keV X-rays in time-coincidence with the laser pulse. Adapted from [22].

to maximize the number of muonic helium ions available in the $2S$ state: the lifetime of the $2S$ metastable state (τ_{2S}) and its relative population (ϵ_{2S}) [22].

The $2S$ lifetime is determined by three parameters, the muon lifetime ($\tau_\mu = 2.2 \mu\text{s}$), the $2S - 1S$ two-photon decay rate and the quenching rate, which in turn depends on the helium pressure. Thus, since the environment is gaseous the interactions with the gas molecules have to be considered. It is known that the quenching rate shortens the $2S$ lifetime for higher gas densities, and consequently for higher pressures (in the mbar region). For this experiment, simulation studies determined the best gas pressure to be 4 hPa, corresponding to a lifetime of $1.71 \mu\text{s}$ and a long-lived $2S$ population of $\epsilon_{2S} = (2.2 \pm 0.3)\%$ [22]. For these calculated parameters, only a few “good” events per hour on resonance are expected. Therefore, the X-ray detection and the laser systems are optimized to obtain as many events as possible.

The experiment is taking place at Paul Scherrer Institute in Switzerland. The institute has a proton beam facility where protons are accelerated to 590 MeV (2 mA current) and collide with a carbon target with a 40 mm thick rotating-wheel. Pions and muons are there produced and partly guided by a secondary beam line to the $\pi E5$ area. The experimental apparatus in figure 4.2 shows the muon beam line and the solenoid containing the target, the X-ray and electron detector systems and the laser cavity. Two other zones outside the radiation environment complete the experimental apparatus, the laser hut and the counting room. The laser hut is where the laser system is implemented. The laser output is directed by a set of mirrors to the cavity mirror inside the gas target. Most of the data acquisition system for the experiment, ADCs, TDCs, WFDs, NIM and VME modules, the frontend and backend computers, as well as computers to monitor the online data-taking are placed inside the counting room. Details about each part of the experimental apparatus are described below.

4.1 Muon Beam Line and Target Systems

After the proton generation by the cyclotron ring and posterior production of pions and muons, particles are driven to the $\pi E5$ area with the goal of forming muonic helium atoms. In order to achieve this, a complex beam line is assembled, as seen in figure 4.3. The beam line is composed of the following parts:

- Cyclotron Trap (CT) - where pions decay into high energy muons and these are decelerated into low-energy muons.
- Muon Extraction Channel (MEC) - responsible for the transport and selection of low energy muons.
- PSC solenoid with two transmission detectors for muon detection. The gas target is placed inside the PSC solenoid, as well as the optical cavity and the X-ray and electron detectors.

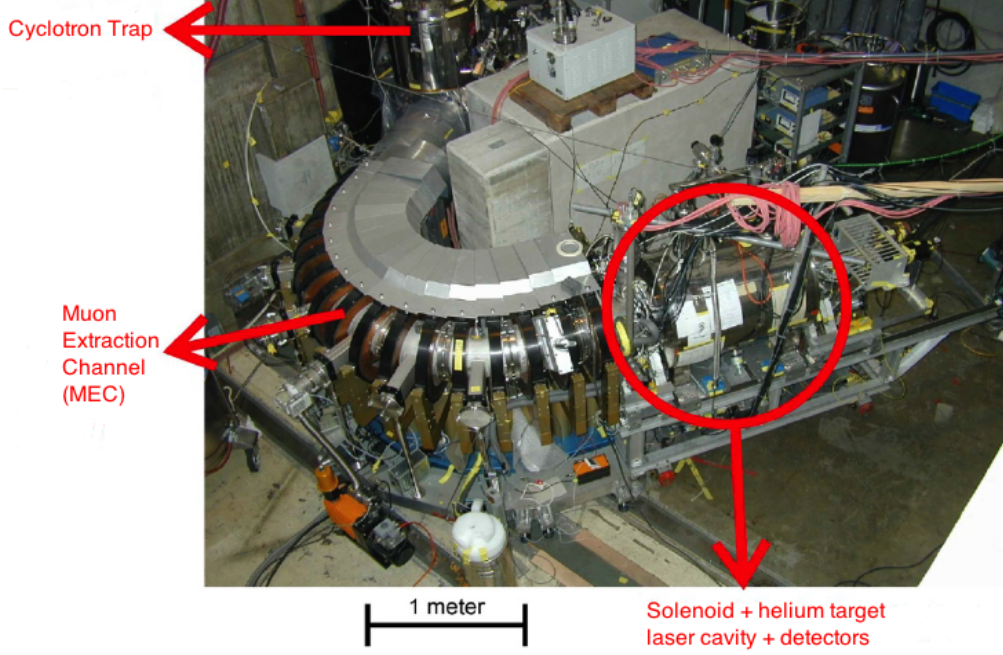


Figure 4.2: Part of the complex experimental apparatus used for the muonic helium Lamb shift experiment, located in the $\pi E5$ area at PSI. The experimental apparatus is complete with the laser hut and counting room areas, not shown in the figure. The CT is responsible for the decay of pions into muons, the MEC, is in charge of selecting the appropriate muons and their transport to the PSC solenoid, which incorporates the helium target, the optical cavity and the X-ray and electron detectors. Adapted from [85].

About $10^8 s^{-1}$ negative pions with a $102 \text{ MeV}/c$ momentum enter the CT area tangentially. After hitting a moderator, they lose energy and decay into negative muons with energies of the order of MeV. Muons are slowed down when passing many times through a metallized thin foil (Formvar) polarized with a high voltage. The magnetic forces dominate over the electric field applied to the foil, until low kinetic energies, of the order of tens of keV, are achieved. Muons that escape from the CT enter the MEC, a curved solenoid for transport and selection, which works as

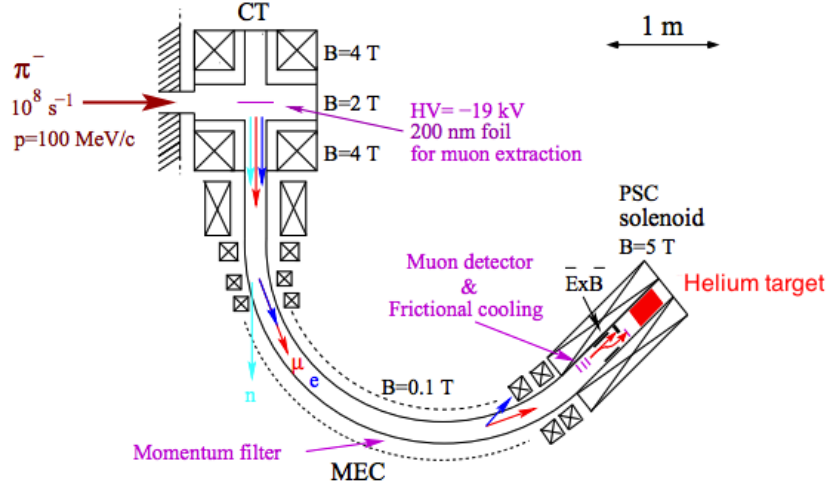


Figure 4.3: Schematic of the muon beam line and target systems. After protons produce pions, these are slowed down by hitting a moderator with posterior decay into muons in the CT. The muons which escape from the CT are driven through the MEC and directed to the PSC solenoid to form muonic helium atoms. Adapted from [85].

a momentum filter. This region operates at a 0.15 T toroidal magnetic field, selecting muons with 20 keV energy and providing their separation from unwanted background radiation and particles (see figure 4.3). For example, an intense flow of electrons is one of the background contributions, produced when muons pass through the coil [7]. It is the curved configuration, leading to an horizontal gradient and consequently a downward force, which is responsible for separate muons from electrons, along with their velocity difference. After this selection, muons are driven to the PSC solenoid that contains the gas target volume and two transmission detectors to set the muon trigger, as well as the optical cavity and the X-ray and electron detectors. This solenoid operates under a 5 T magnetic field to guarantee minimum radial dispersion of the muon beam and enhance its concentration in the target volume. Before entering the gas volume, muons cross two stacks ($S1$ and $S2$) of ultra thin carbon foils, with $4\mu\text{g}/\text{cm}^2$ thickness each, where they release electrons, as shown in figure 4.4 [43].

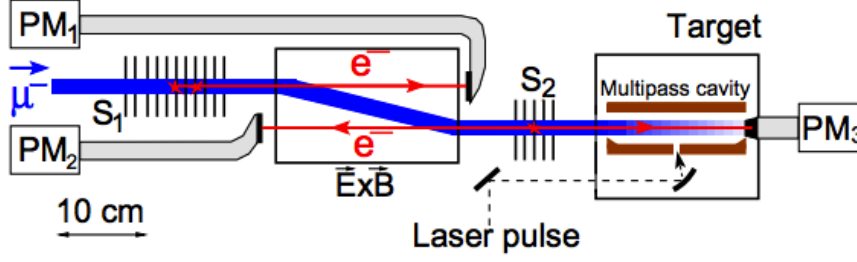


Figure 4.4: Schematic of the PSC solenoid with 1 m length. Inside there are muon detectors, the gas target, the optical cavity and X-ray and electron detectors. When a muon passes through the first stack, S_1 , electrons are released and are detected in a scintillator coupled via light guides to a photomultiplier, PM_1 . The same process occurs in the S_2 stack, however the electrons are detected by either the PM_2 or PM_3 detectors. Those two signals in TOF coincidence are the signal trigger for the laser and the data acquisition system. After the S_2 stack interaction, the muon continues arriving at the gas target where muonic helium atoms will be formed. Adapted from [85].

The first stack, denoted as S_1 , is kept at voltages up to -12 kV, decelerating muons down to $5 - 8$ keV. The released electrons are driven to a scintillator coupled to a photomultiplier (PM_1) through light guides. Due to an $\vec{E} \times \vec{B}$ separator between the stack and the scintillator, the transversal shift is higher for muons than for electrons, allowing muons to continue their trajectory towards the target. The electrons will be accelerated towards the scintillator and detected, originating the first muonic signal (S_1^{down}).

Once the muon reaches the second stack (S_2), the process is repeated, nevertheless the electrons are detected by either the PM_2 or PM_3 photomultipliers, originating the second muonic signal (S_2^{up} or S_2^{down} , respectively). In practice the electrons from S_1 and S_2 , in time-of-flight coincidence (with typical time of flight of 150 ns for 5 keV muons) will originate the trigger signal for the data acquisition system and for the laser.

Inside the target system, muons are slowed down in the gas volume (with a pressure of approximately 3 hPa and a length of 20 cm) by collisions with the gas atoms and are finally captured by a helium atom, producing μHe in highly excited states (see section 2.2). The gas volume is surrounded by a multipass cavity and above and below there are x-ray detectors positioned. The electron detectors are also located there but more aside, as explained below.

4.2 Laser System and Optical Cavity

When the trigger signal from muon detectors is set, the laser system is triggered. The laser has to deliver pulses of 4 mJ at 812 nm (figure 4.5). It has also to be stochastically triggerable, with average rates of about 500 s^{-1} and a delay time between the trigger signal and the arrival of the pulse to the cavity shorter than $1.7\text{ }\mu\text{s}$. It has to be tunable around the predicted transition frequency (800-970 nm), with a bandwidth below 10 GHz to search for the resonance [19, 22, 36].

The complex laser system is composed by 3 distinct parts. The frequency double Yb:YAG thin disk laser responsible for pumping the Ti:Sa ring laser with 43 mJ of 515 nm light. It has a Q-switched oscillator and 12 pass amplifier generating 80 mJ pulses which are converted by a non-linear crystal into the 43 mJ. The tunable continuous wave (cw) Ti:Sa laser is in charge of determining the wavelength and locking the cavity laser and for monitoring the wavemeters. The stability is guaranteed by locking it to an external Fabry-Perot cavity [19]. And at last, the pulsed Ti:Sa ring laser, which generates pulses of 4 mJ and forward them to the optical cavity, 20 m away from the laser hut.

The light is transported to the optical cavity, illuminating the gas target volume but before it is coupled by means of an off-axis parabolic mirror (OAP), seen in figure 4.5.

The multipass cavity (figure 4.6) made of two sized mirrors placed parallel to each other, surrounds the gas target. It is designed to be robust, insensitive to

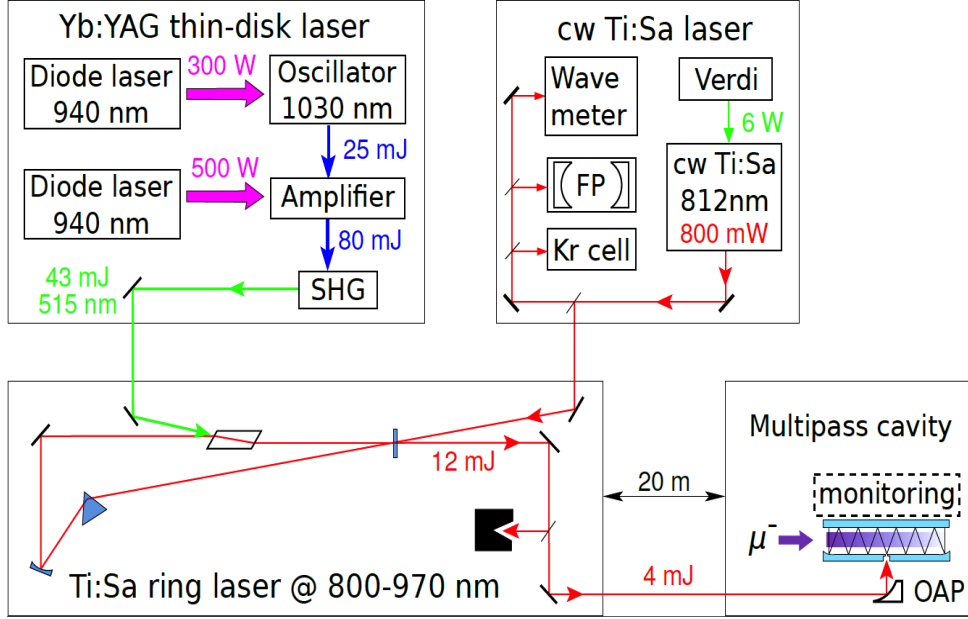


Figure 4.5: Schematic of the laser system used in the muonic helium Lamb shift experiment. It is composed essentially by three distinct parts, the frequency double Yb:YAG thin disk laser responsible for pumping the Ti:Sa ring laser, and the tunable continuous wave (cw) Ti:Sa laser. At the end pulses with 4 mJ are directed to the optical cavity. Assigned by CREMA.

misalignment and to illuminate the whole gas volume. The laser enters through a small hole (0.6 mm diameter) in the centre of one of the mirrors.

4.3 X-ray and Electron Detectors

When muonic helium atoms in the $2P$ state de-excite to the ground state, they emit 8.2 keV X-rays. Only a few good events per hour are expected in coincidence with the laser pulse, so it is very important to ensure that all events are recorded. The most important X-ray detector requirements are:

- no performance degradation under intense magnetic field (5 T),
- good energy resolution,

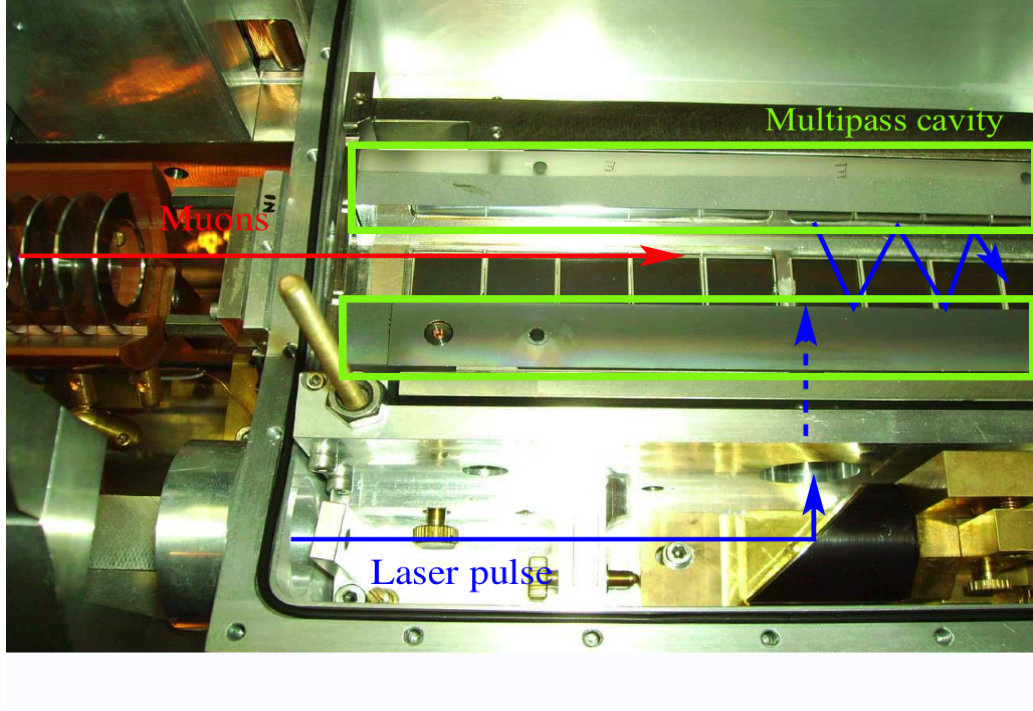


Figure 4.6: Multipass cavity (green) and one LAAPD array mounted inside the target and below the muon beam axis. It is also visible from where the muon beam enters (red) as well as the laser pulse (blue) and the path of its reflection in the cavity. Assigned by CREMA.

- compactness and robustness,
- fast time response.

The X-ray detectors chosen for the experiment are large area avalanche photodiodes from RMD, model S1315 [86], biased to approximately 1600 V (figure 4.7). For 8.2 keV X-rays emitted by muonic helium atoms, they present about 20% energy resolution (FWHM), and show no performance degradation under 5 T magnetic fields [87]. The X-ray detection system for the μHe experiment is composed by 2 arrays of 10 APDs, placed face-to-face in the top and bottom sides of the gas target, 8 mm from the muon beam axis (see figure 4.8). The detection efficiency is about 50% for 8 keV X-rays. The signal output amplitude is approximately 2 mV with

25 ns rise time. Each APD has a pre-amplifier attached, a low noise charge sensitive pre-amplifier designed by ETH and responsible for the first amplification stage, with approximately 500 mV amplitude signals. The two APD arrays and the pre-amplifiers are cooled down to -30°C using a circulation alcohol system. This low temperature allows for low dark current, thus improving the detector's performance.

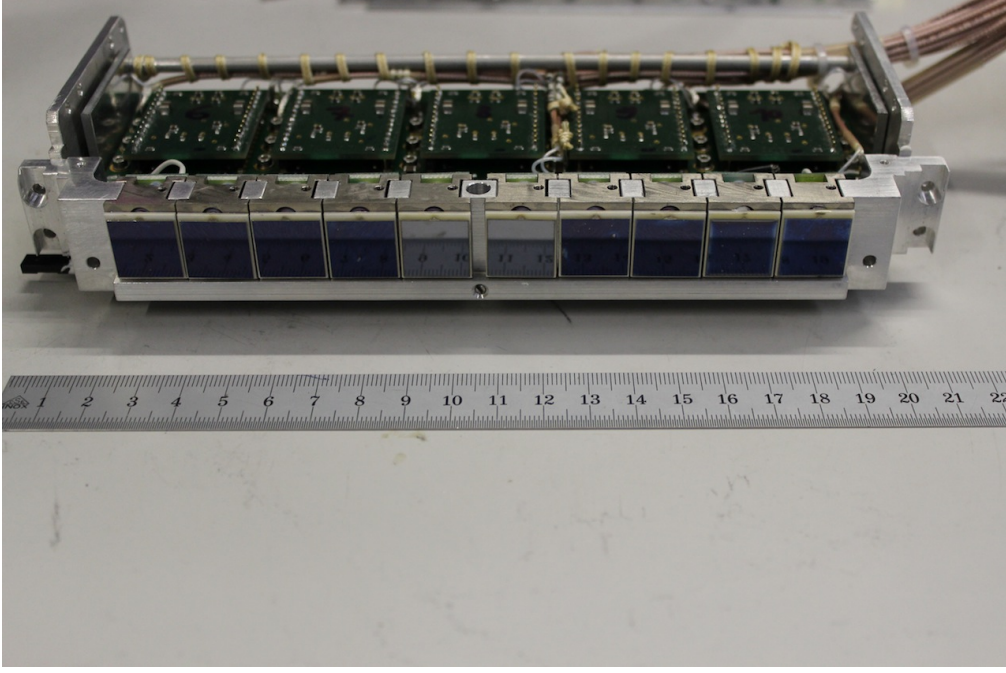


Figure 4.7: One array of APD detectors from RMD, model S1315, used as X-rays detectors, and the respective pre-amplifiers.

The pre-amplifier signal goes to the post-amplifier, a linear amplifier with a gain of 4, placed relatively near the detector but outside the vacuum chamber, to provide an amplitude signal of few Volts in order to be driven safely to the data acquisition system.

An important issue to take into account in the experiment is the detection of electrons (with MeV energies) resulting from the muon decay. These charged particles are detected by 2 pairs of 2 plastic scintillator plates each (E_{left} and E_{right}) which have an X-shaped structure around the target system. Two scintillators from the same side, left or right, are connected to the same light guide which drives the signal

4.3. X-ray and Electron Detectors

to one PMT. But electrons can also be detected by APDs, originating signals with high amplitudes, when compared with 8 keV X-rays. The electron detection by plastic scintillators or APDs in coincidence with X-ray detection in an APD will be useful to reduce the background of the experiment.

The Maximum Integrated Data Acquisition System (MIDAS) is a data acquisition system developed at PSI and Triumf Laboratory [88], used in the muonic helium Lamb shift experiment for data collection and recording, for data flow control, for hardware drivers and for event-by-event analysis. When electrons from $S1$ and $S2$ stacks, in TOF coincidence are detected (confirming a muon detection), a trigger signal for the laser and the DAQ systems is set, opening an Event Gate (EVG) of $20\ \mu\text{s}$. The laser will deliver pulses inside the optical cavity in order to induce the $2S - 2P$ transition and the DAQ system is ready and is waiting for electron and X-ray signals in order to be processed in NIM and VME modules for posterior saving in the hard disc driver at the backend computer. If one 8.2 keV X-ray is detected in one APD (and consequently amplified in the pre-amplifier and the post-amplifier) during the EVG,

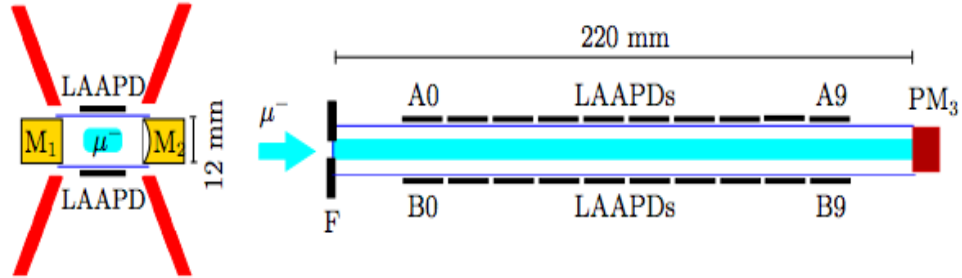


Figure 4.8: Schematic showing the X-ray and electron detectors inside the target in a sectional view. (Left) The electron detectors are 2 pairs of 2 plastic scintillator plates (E_{left} and E_{right}) (red) with an X-shaped structure around the target system. Scintillators from the same side (left or right) are read by the same PMT. $M1$ and $M2$ are the mirrors from the cavity (yellow). (Right) The muon beam enters in the target system and on the top and below there are two arrays of APDs, each with 10 detectors labelled from 0 to 9 (in the muon beam direction). Adapted from [85].

the signal will be split in two paths at this stage. One drives the signal to a clock-amplifier, which adds a time stamp and direct it to a Waveform Digitizer (WFD) where the data is stored. It is a 12 bit CAEN [89] module, with 3752 bins and a length of $15\text{ }\mu\text{s}$ (4 ns per bin). The other path is in charge of deciding whether the pulse stored in the WFD is useful or not. The signal goes to a shaping amplifier where all the accurate time information is lost in order to shape the noisy signal for further threshold discrimination in the slow discriminator, settling the minimal detectable energy. The next stage is a TDC, responsible for recording the discriminator outputs and for deciding which WFD should be read out and saved. This module integrates all the APDs signals since all detectors are here connected. In the meantime a gate of $5\text{ }\mu\text{s}$ is opened before the EVG if a click in one of the 20 APDs is detected, indicating a possible successful X-ray signal that happened before the EVG. It is one way to avoid losing important data. In parallel, and after the X-ray detection, the 2 PMTs or even an APD are available for electron detection. The signal is then discriminated and hereafter recorded by a TDC. At the end of the $25\text{ }\mu\text{s}$ a signal to stop the DAQ system is set, the End of Event Gate (EEVG), stopping the WFDs and the Time to Digital Converters (TDCs). The DAQ system is again prepared for processing more data.

Chapter 5

Reach-Through Avalanche Photodiodes for 8 keV X-ray Detection

Reach-through avalanche photodiode are silicon APDs with thicker depletion region than regular APDs, which makes them more efficient for detection of higher-energy X-rays [23, 24]. The main disadvantage remains in the manufacturing technique of large area prototypes, which is not reliable yet. Companies such as Hamamatsu Photonics and Perkin Elmer Optoelectronics are producing RT-APDs, although with small detection areas [80, 90].

The main objective of this work is to investigate the performance of RT-APDs from Hamamatsu with different active areas, $3 \times 5 \text{ mm}^2$ and $5 \times 5 \text{ mm}^2$, for low-energy X-ray detection in view of their use in the muonic helium Lamb shift experiment [19], where 8 keV X-rays need to be detected with good efficiency. In the previous experiment, for muonic hydrogen [7, 9], large area avalanche photodiodes from RMD [86] were used to detect 2 keV X-rays. The main characteristics of RMD APDs for 2 keV X-rays are: detection efficiency above 90%, energy resolution of about 15%, compactness, fast time response, large active areas of $13.5 \times 13.5 \text{ mm}^2$ and insensitivity to magnetic

fields up to 5 T [7, 9, 53]. However, for 8 keV X-rays, they have an efficiency of only 40%, without considering the effect of the X-ray incident angle, motivating the investigation of RT-APDs as alternative.

The performance characteristics of two RT-APD prototypes have been investigated. Gain, minimum detectable energy and energy resolution were determined as a function of bias voltage and temperature. The gain non-linearity between X-rays and visible light has been evaluated.

Since the energy resolution is a critical parameter in the muonic helium Lamb shift experiment, the different contributions were evaluated in view of a better understanding of its behaviour, the gain non-uniformity was estimated and the excess noise factor was determined.

The energy resolution is in general defined by the FWHM of the peak obtained in the amplitude spectrum. Several contributions are responsible for the peak broadening in silicon APDs:

- statistical fluctuations associated with the number of electron-hole pairs produced in the silicon and related to the avalanche process;
- gain non-uniformity due to impurities and crystal imperfections;
- noise, generated by the detector dark current and by the preamplifier electronics.

The energy resolution of a measured peak (ΔE) can be mathematically represented as the quadratic addition of the three contributions:

$$(\Delta E)^2 = (\Delta E_s)^2 + (\Delta E_u)^2 + (\Delta E_n)^2, \quad (5.1)$$

where ΔE_s corresponds to the statistical fluctuations, ΔE_u the fluctuations associated to the gain non-uniformity and ΔE_n the noise fluctuations [53, 58].

The intrinsic energy resolution, which is given by all contributions except the noise, is essentially defined by the fluctuations associated to the production of electron-hole pairs and to the electron multiplication process. The spatial non-uniformity may also

contribute to the intrinsic energy resolution, particularly in X-ray detection, due to the point-like absorption of the X-ray, while in light detection the primary electron-hole pairs are spread over the APD volume if the whole area is illuminated, averaging local gain variations [49, 51, 52]. Non-uniform silicon resistivity leads to electric field variations, and consequently to gain fluctuations. Therefore the contributions to take into account in the intrinsic energy resolution are different in light and X-ray detection. Another relevant aspect to take into account is the Fano factor, f , which describes the relative variance in the process of electron-hole pair production for energy loss in matter. This parameter is well known in the area of radiation detectors, being in silicon about 0.12 [58]. Monte Carlo simulation has shown that this parameter is almost constant with temperature presenting small fluctuations around 0.117 [91].

5.1 Experimental Setup

Figure 5.1 shows a picture of the two RT-APDs from Hamamatsu, model S10936-0374, used in these studies. They present a depletion region of $130\text{ }\mu\text{m}$. One is rectangular with $3 \times 5\text{ mm}^2$ active area and the other one is square with $5 \times 5\text{ mm}^2$ active area. The RT-APDs were mounted on a titanium piece for efficient cooling and connected to RAL-108A low noise charge sensitive preamplifiers [55]. A typical signal at the RAL preamplifier output has about 200 ns rise-time, more than $100\text{ }\mu\text{s}$ fall-time and amplitudes of about $100\text{-}200\text{ mV}$. According to the datasheets provided by the manufacturer, the relevant parameters of each RT-APD are listed in Table 5.1.

Table 5.1: Operational parameters of the RT-APDs from Hamamatsu at 25°C .

APD size	Active area (mm^2)	Breakdown voltage (V)	Gain (V=200 V)
5×5	25	623	39
3×5	15	510	57

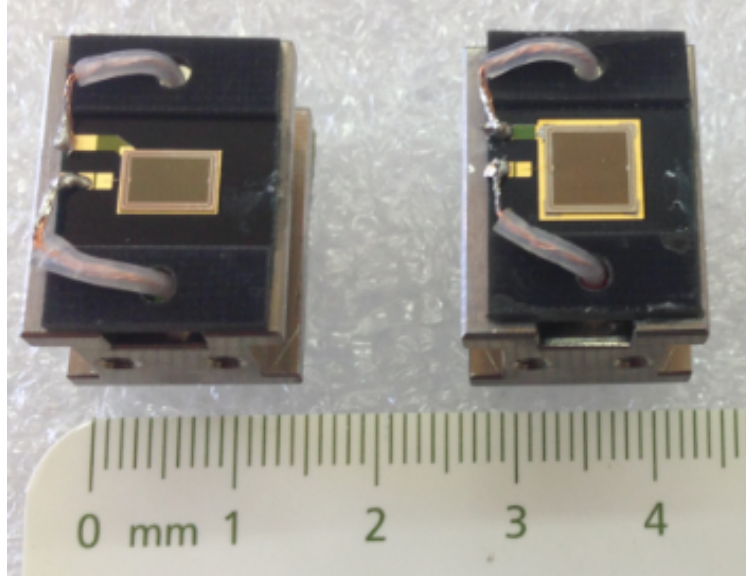


Figure 5.1: RT-APDs from Hamamatsu Photonics with active areas of $3 \times 5 \text{ mm}^2$ and $5 \times 5 \text{ mm}^2$. The APDs are mounted on Ti pieces for efficient cooling.

The RT-APDs, together with the respective pre-amplifiers, were placed inside a vacuum chamber for temperature control. Cooling of the system was provided by an alcohol system connected to the pre-amplifier assembly. Temperature stabilization within $\pm 0.1^\circ\text{C}$ was obtained. The pre-amplifier was connected to an Ortec Spectroscopy Research Amplifier [92] with integration and differentiation time constants of $0.5 \mu\text{s}$ followed by a multi-channel analyser (AmpTek Pocket MCA 8000A) [93]. A positive high voltage power supply was used to polarize the APDs. A Light Emitting Diode (LED) was operated in pulse mode with peak emission at 600 nm and was supplied by a "LED pulser" giving pulses of 100 – 500 ns width and up to -10 V amplitude. The LED was coupled to a light guide to transport the light pulses towards the detector surface. A ^{65}Zn radioactive source emitting 8.0 keV K_α and 8.9 keV K_β X-rays was placed at about 1 cm distance from the detector surface, together with the light guide. No collimator was used, the full active area of the detectors was irradiated by the two radiation sources.

5.2 Gain Measurements

It is well known that the gain of the APD depends on the applied voltage as well as on temperature. Another relevant aspect in the response of the APD is the gain non-linearity between X-rays and visible light due to space charge effects in X-ray detection, leading to local gain variations [48, 49, 51, 52, 72]. The gain curves provided by the manufacturer at room temperature (25° C) were used as a reference for our measurements. The normalization was made for a bias voltage of 200 V, which corresponds to a gain of 39 for the 5×5 prototype and 57 for the 3×5 prototype (Table 5.1).

5.2.1 Gain Determination

The gain was measured at 0° C for both RT-APDs as a function of bias voltage, using LED pulses, as shown in figure 5.2. The unitary gain was not determined in our measurements, as no signals could be detected at low voltages for both X-rays or light pulses. The absolute gain was obtained by normalizing the light pulse amplitude to the manufacturer gain (Table 5.1). A correction factor was introduced by comparing the relative amplitudes obtained in each RT-APD at 25° C and 0° C. As shown in figure 5.2, for lower bias voltages the gain drops abruptly. This effect is probably due to the recombination of the primary electrons under very low electric fields, leading to partial charge collection. The gain is higher for the 3×5 prototype at higher voltages, while it is about the same for both RT-APDs at lower voltages.

5.2.2 Gain Non-Linearity

Gain non-linearity takes place at higher gains due to high signal current densities produced by X-rays. The gain obtained for X-rays is lower than for visible light, and the difference increases with bias voltage. The non-linearity owes essentially to space charge effects with a consequent reduction of the local electric field, as

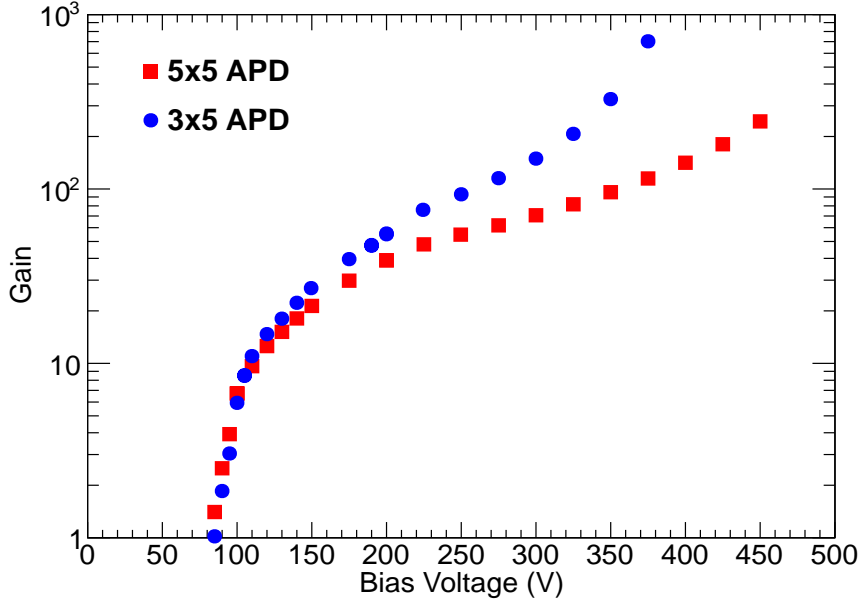


Figure 5.2: Gain obtained for both 3×5 and 5×5 mm² APD prototypes as a function of bias voltage at 0° C, for visible light pulses.

well as local heating, due to the point-like nature of the X-ray interaction. To evaluate the gain non-linearity, the ratio between pulse amplitudes for 8 keV X-rays and visible light pulses from the LED, simultaneously illuminating the RT-APD active area, was determined. Figure 5.3 presents the gain obtained for X-rays and visible light as a function of bias voltage at 25 °C, for the 5×5 mm² RT-APD. The two series of data points were normalized to the manufacturer gain values at 200 V (Table 5.1). Figure 5.3 also displays the dark current measured during measurements. As expected, the light gain is higher than the X-ray gain, increasing significantly for voltages above 400 V. Similarly, the dark current increases with increasing bias voltage, limiting the energy resolution obtained at higher bias voltages, as it will be shown later.

In figure 5.4, the ratio between the gains obtained for 8 keV X-rays and visible light pulses is depicted as a function of the reverse bias voltage for different temperatures. As shown, the variation (gain non-linearity) is not very large for lower voltages, but

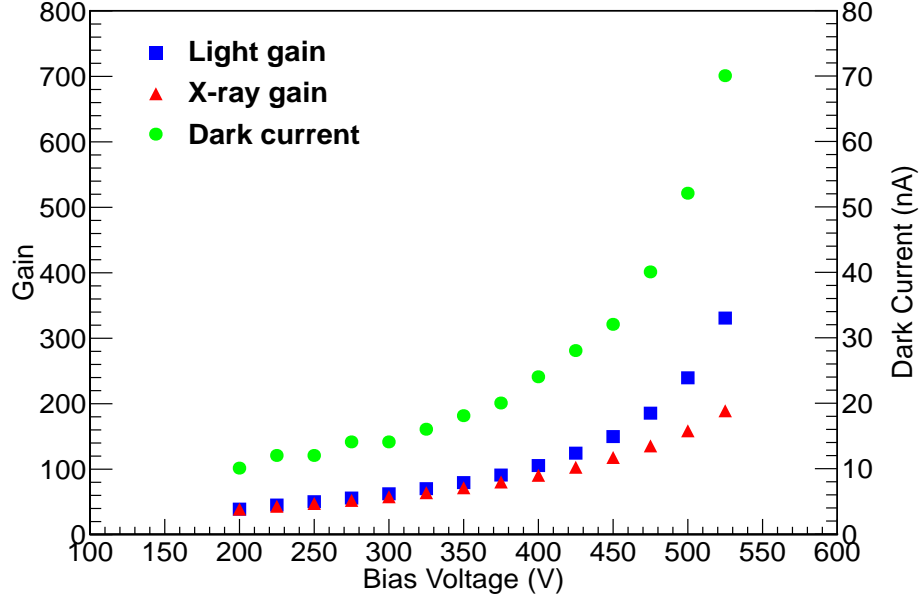


Figure 5.3: *X-ray and visible light gains as a function of bias voltage for the $5 \times 5 \text{ mm}^2$ RT-APD prototype at 25°C . The APD dark current is also plotted.*

increases significantly for voltages above 300 V. The gain non-linearity increases with decreasing temperature, as observed. At 350 V, the gain non-linearity obtained for -20°C , 0°C and 20°C is about 25%, 18% and 10%, respectively.

Figure 5.5 shows the gain non-linearity (same data as figure 5.4) as a function of the RT-APD gain (for light), for different temperatures. As shown, the gain non-linearity increases slightly with decreasing temperature. For a gain of 200, the gain non-linearity is about 30%, 37% and 42% for 20°C , 0°C and -20°C , respectively. For gains of about 300, the non-linearity is as large as about 50%, for temperatures of -20°C and 0°C . This behaviour is expected since, for the same voltage, the density of charge carriers is larger for lower temperatures as a result of higher gain, so the space charge effect is stronger. Although the behaviour agrees with the results reported in [94]. The values obtained are significantly larger than the ones observed in other types of APDs. For instance, for a gain of 200 and for 5.9 keV X-rays, gain non-linearities between 7% and 10% were measured with LAAPDs from Advanced

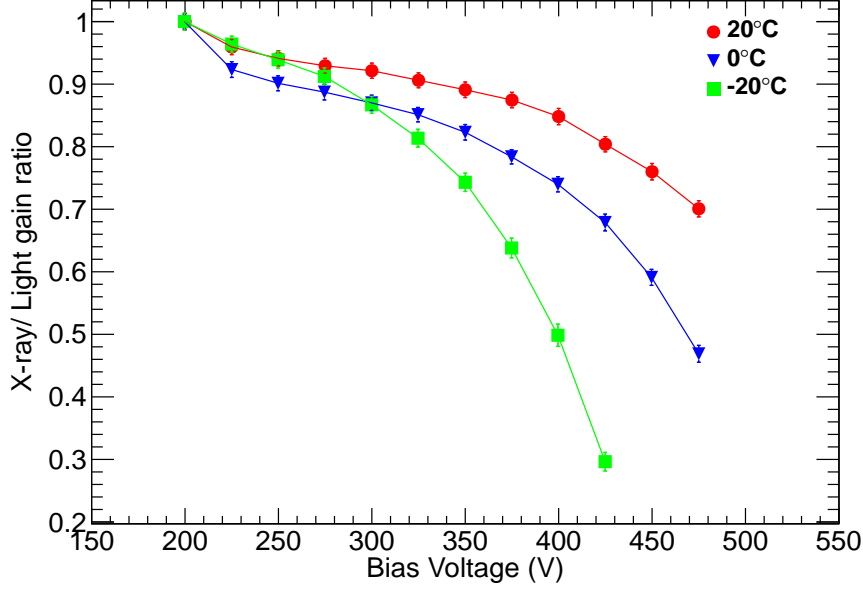


Figure 5.4: Gain non-linearity between X-rays and visible light pulses for the $5 \times 5 \text{ mm}^2$ RT-APD as a function of bias voltage for different temperatures.

Photonics Inc. [53]. For 5.4 keV X-rays and for a gain of 400, a 10% deviation was obtained for LAAPDs from RMD [52]. However, as stated in [47], the non-linearity obtained for larger active areas are smaller when compared to prototypes with smaller areas.

5.2.3 Temperature Dependence

Gain measurements were performed at different temperatures for both X-rays and visible light pulses. Normalization to the gain provided by the manufacturer at 200 V and 25°C was made. Figure 5.6 shows that the behaviour observed at room temperature is also reproduced at lower temperatures, for X-rays. The gain increases with increasing voltage for both RT-APDs, and decreases with increasing temperatures. For the $5 \times 5 \text{ mm}^2$ RT-APD at 350 V, the gain obtained at -20°C is about twice the gain obtained at 20°C .

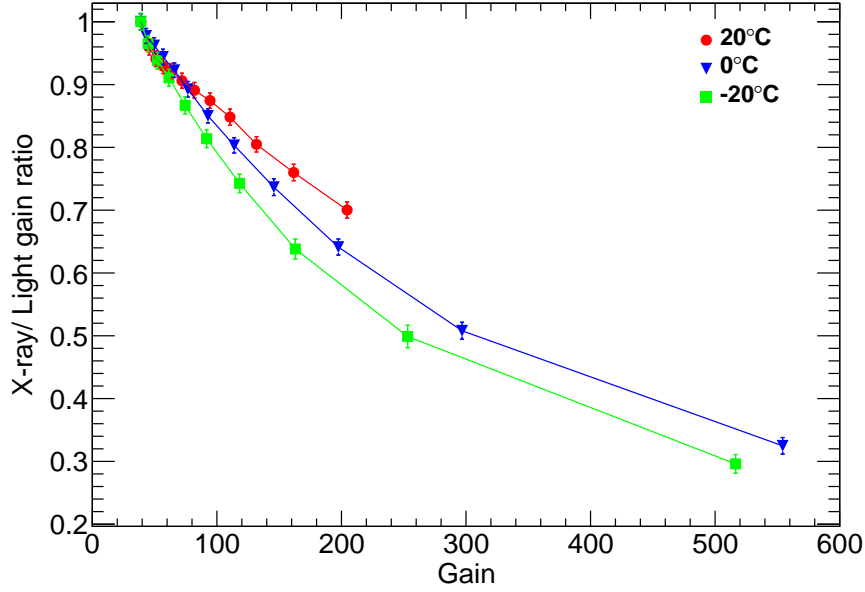


Figure 5.5: Gain non-linearity between X-rays and visible light pulses for the $5 \times 5 \text{ mm}^2$ RT-APD as a function of the APD gain (obtained for light pulses) for different temperatures.

In figure 5.7, the X-ray gain is plotted as a function of temperature for different bias voltages for the $5 \times 5 \text{ mm}^2$ RT-APD. For a given bias voltage, the gain increases with decreasing temperature, as expected. The relative gain change with temperature is practically constant for each voltage, as shown by the exponential fits in figure 5.7. The gain relative variation increases with bias voltage, being -1.0% per $^{\circ}\text{C}$ at 200 V and -1.7% per $^{\circ}\text{C}$ at 400 V. Comparable results were obtained for the $3 \times 5 \text{ mm}^2$ prototype. Nonetheless, the variation is smaller than the one reported for other types of APDs [51, 52], where relative variations of -4.5% per $^{\circ}\text{C}$ were measured for the higher voltages applied. Even for the same type of RT-APD, this result is smaller than the one reported in [23], where a variation of -2.2% per $^{\circ}\text{C}$ was found at 200 V.

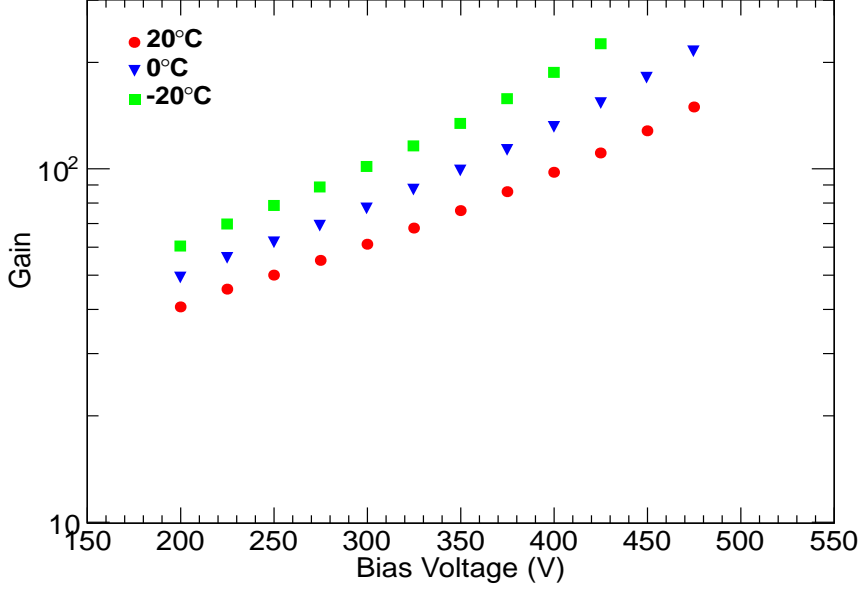


Figure 5.6: X-ray gain as a function of bias voltage for different temperatures obtained with the $5 \times 5 \text{ mm}^2$ RT-APD.

5.3 Response in X-Ray Detection

The response of the RT-APDs was evaluated in view of their implementation as X-ray detectors in the muonic helium Lamb shift experiment. The performance characteristics in the detection of 8 keV X-rays were investigated at different temperatures, in particular the energy resolution and minimum detectable energy. Figure 5.8 shows a typical pulse-height distribution for 8 keV X-rays interacting in the two RT-APDs investigated. The distributions are normalized to the same number of events in the X-ray peak region and were obtained at 0°C for $V = 300 \text{ V}$. The X-ray distribution of the $5 \times 5 \text{ mm}^2$ prototype presents a well-defined Gaussian, while the $3 \times 5 \text{ mm}^2$ prototype shows larger asymmetry to the left, compromising the energy resolution obtained. Nonetheless, since only one prototype of each size was tested, solid conclusions cannot be driven by the trend shown.

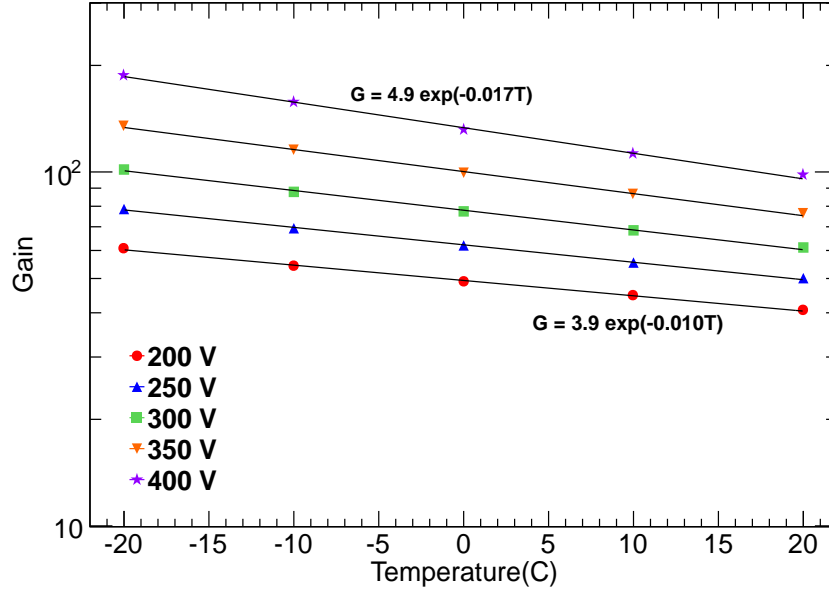


Figure 5.7: X-ray gain as a function of temperature for the $5 \times 5 \text{ mm}^2$ RT-APD prototype at different bias voltages. Exponential fits to the data points are shown.

As seen in figure 5.8, there is no significant tail towards the low-energy region, for both RT-APDs, unlike what was reported in [53] and [52]. This reveals that almost all the 8 keV X-rays are fully amplified. The electronic noise tail observed in the energy distributions determines the minimum detectable X-ray energy.

5.3.1 Energy Resolution

The energy resolution for 8 keV X-rays obtained at 20°C in both RT-APDs is depicted in figure 5.9 as a function of the gain. The best energy resolution achieved is 11% (FWHM) for the $5 \times 5 \text{ mm}^2$ prototype, obtained at a gain of 55. For the $3 \times 5 \text{ mm}^2$ prototype, the minimum value is 12.1% at a gain of 60. It is observed that the energy resolution degrades for higher gains. This is due to the increase of the dark current with voltage and gain (see figure 5.3).

The temperature dependence of the energy resolution is shown in figure 5.10. As expected, and similar to APDs from references [51, 52], the energy resolution

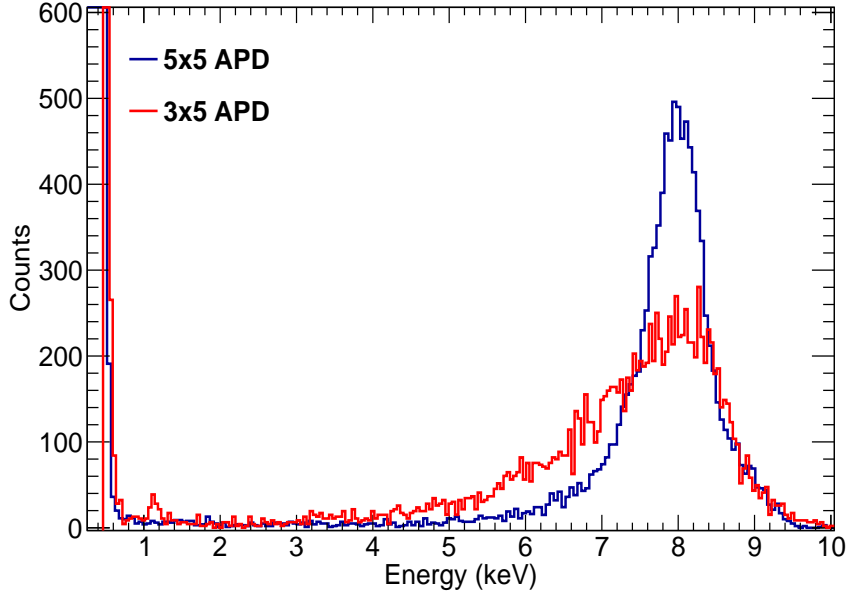


Figure 5.8: Typical energy distributions for 8 keV X-rays, obtained with two RT-APDs prototypes at 0° C for a bias voltage of 300 V.

improves for lower temperatures and degrades for higher gains. This behaviour is in accordance with the variation of the dark current with temperature and gain. There is no significant improvement in the energy resolution below 0° C. The best energy resolution achieved was 9.5% at 0° C for a gain of 55.

5.3.2 Minimum Detectable Energy

The minimum detectable energy (MDE) is defined as the channel in the amplitude spectrum where the number of counts in the noise distribution reaches 10% of the counts at the height of the X-ray distribution (centroid channel), the MDE being the corresponding energy normalized to the centroid of the 8 keV X-ray peak. This definition is suitable for our typical X-ray source intensities which correspond to a rate of detected events of order 8000/s. The MDE is presented in figure 5.11 as a function of gain for both RT-APDs at 0° C. The minimum detectable energy decreases with gain and is lower for the smaller prototype, although the difference is not significant.

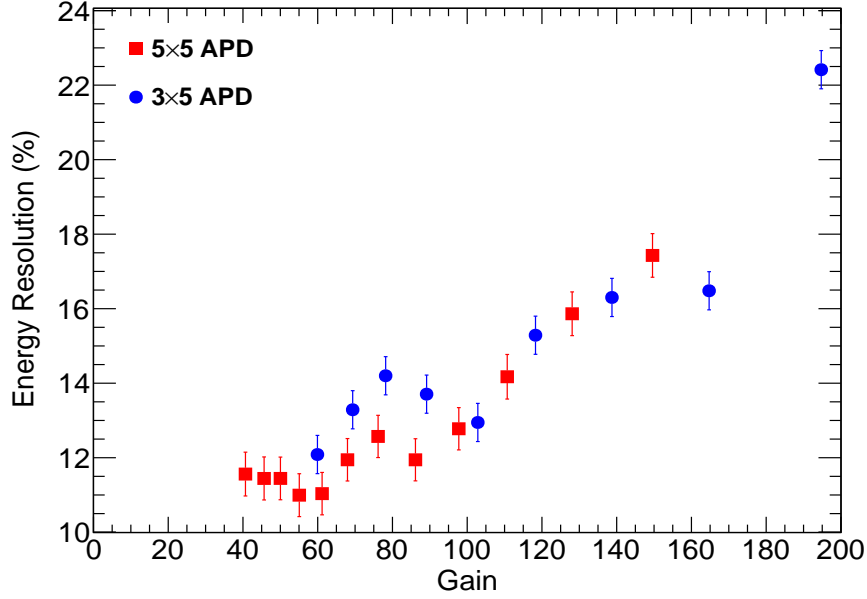


Figure 5.9: Energy resolution for 8 keV X-rays as a function of gain, obtained at 20° C for both $5 \times 5 \text{ mm}^2$ and $3 \times 5 \text{ mm}^2$ prototypes.

The best MDE value obtained is about 0.25 keV for the higher gains. However, it is 0.9 keV in the gain region corresponding to the best energy resolution. The MDE was determined for different temperatures, as seen in figure 5.12 for the $5 \times 5 \text{ mm}^2$ RT-APD. The trend is similar for each temperature, the MDE has a fast initial decrease with gain and tends to stabilize for high gains. It improves with decreasing temperature. Still, this behaviour is not as significant as for other types of APD [53].

5.4 Contributions to the Energy Resolution

By simultaneous measurements of X-rays and visible light pulses detected in the APD, as well as test pulses from a reference pulser injected in the preamplifier, the contributions to the energy resolution, expressed in equation (5.1), can be determined from the width of each peak in the pulse-height distribution. Figure 5.13 shows a typical pulse-height distribution obtained in the RT-APD for the three different

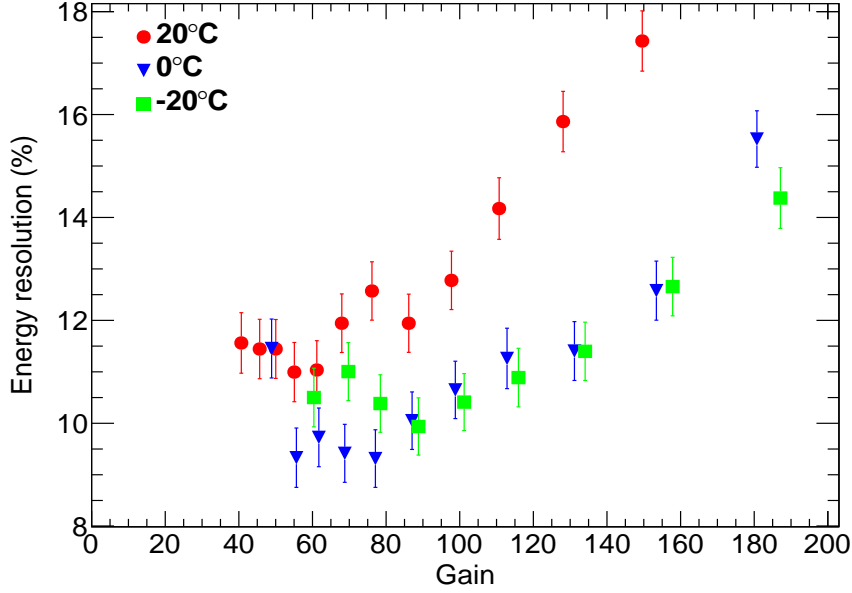


Figure 5.10: Energy resolution for 8 keV X-rays as a function of gain, obtained in the $5 \times 5 \text{ mm}^2$ prototype, at different temperatures.

signals: 8 keV X-rays, visible light pulses, and test pulses from a pulse generator. The centroid of the X-ray peak defines the energy calibration for the visible light peak [95]. The electronic noise contribution to the energy resolution is determined by the pulser peak broadening in the pulse-height distribution (FWHM in units of energy). The position of the pulser peak does not depend on the detector's gain [49, 52]. The noise contribution can be quadratically subtracted from the total energy resolution to extract the intrinsic energy resolution of the detector and also to determine the excess noise factor.

The signal variance associated to the statistical contribution in equation (5.1) is given by:

$$\sigma_s^2 = \sigma_N^2 + N(F - 1), \quad (5.2)$$

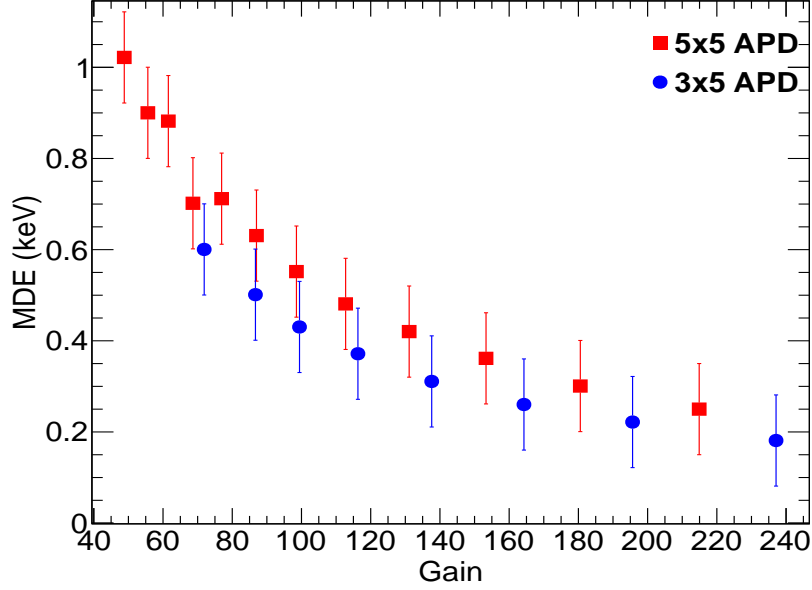


Figure 5.11: Minimum detectable energy as a function of gain for both $5 \times 5 \text{ mm}^2$ and $3 \times 5 \text{ mm}^2$ RT-APDs at 0° C .

where N is the number of primary electrons, σ_N its variance and F the excess noise factor. F is related to the variance of the gain during one avalanche, σ_A^2 , for a specific gain G . It is defined by:

$$F = 1 + \frac{\sigma_A^2}{G^2}. \quad (5.3)$$

In light detection, if the whole active area of the APD is irradiated, the contribution associated to the gain non-uniformity in equation (5.1) is negligible, since the final pulse results from the average response to the full amount of photons interacting in the absorption region of the APD. The intrinsic energy resolution for light detection, considering the variance of the number of primary electrons described by Poisson statistics ($\sigma_N^2 = N$), is given by:

$$R_{int}^L = 2.355 \frac{\sigma_s}{N} = 2.355 \sqrt{\frac{F}{N}}, \quad (5.4)$$

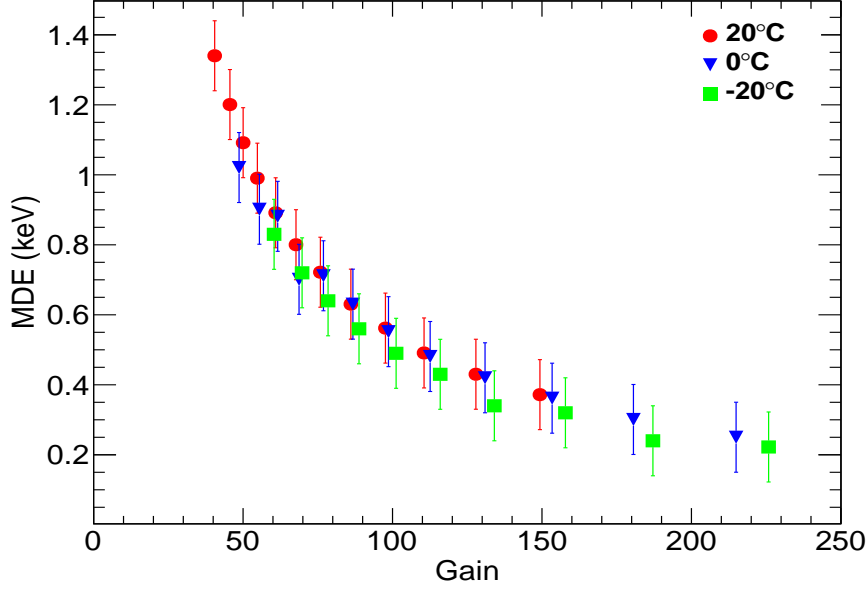


Figure 5.12: Minimum detectable energy as a function of gain for the $5 \times 5 \text{ mm}^2$ prototype at different temperatures.

where $\sigma_s^2 = NF$ was used, following equation 5.2.

In X-ray detection, one needs to take into account the non-uniformity contribution and the Fano factor, f . Therefore, the variance in the number of primary electrons is $\sigma_N^2 = Nf$ and the statistical contribution takes the form:

$$\sigma_s^2 = N(F + f - 1). \quad (5.5)$$

The intrinsic energy resolution in X-ray radiation will be:

$$R_{int}^X = 2.355 \sqrt{\frac{F + f - 1}{N} + \left(\frac{\sigma_U}{G}\right)^2}, \quad (5.6)$$

where σ_U/G is the relative standard deviation associated to gain non-uniformities.

If the number of primary electrons produced in silicon by both X-rays and light pulses is the same, from equations (5.4) and (5.6), the intrinsic energy resolution for X-rays and light are related by:

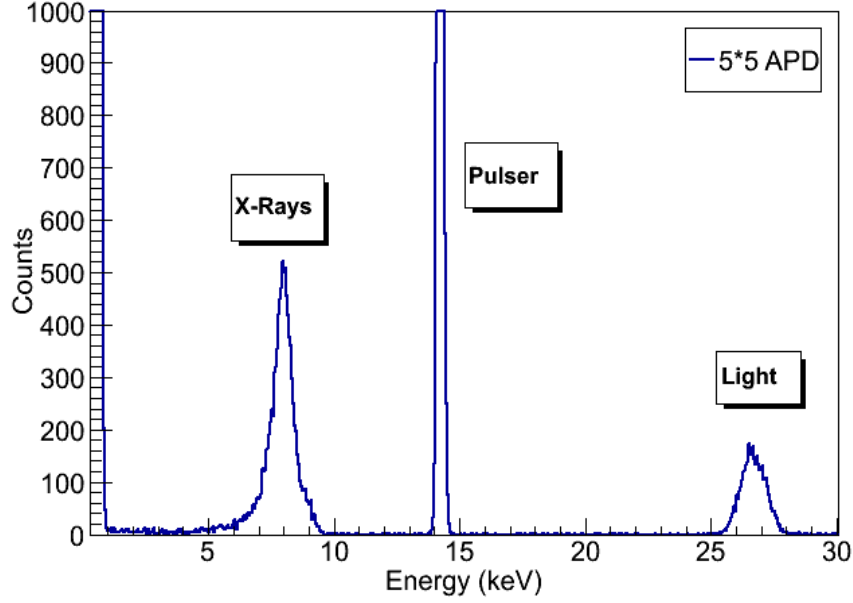


Figure 5.13: Typical pulse-height distribution obtained in the RT-APD from 8 keV X-rays emitted by a ^{65}Zn source, visible light pulses from a LED and pulses from a reference pulser directly injected in the preamplifier test input.

$$(R_{int}^X)^2 - (R_{int}^L)^2 = (2.355)^2 \left[\left(\frac{f-1}{N} \right) + \left(\frac{\sigma_u}{G} \right)^2 \right]. \quad (5.7)$$

5.4.1 Energy Resolution for X-rays and Light

Figure 5.14 shows the energy resolution obtained for 8 keV X-rays and visible light pulses with the same energy deposited, as a function of gain for different temperatures (20°C, 0°C and -20°C). As seen, the energy resolution improves with decreasing temperature for both X-rays and visible light, but the improvement is not significant from 0°C to -20°C. The optimum gain, providing the best energy resolution achieved, is in the region 50-100. Energy resolution values between 7% and 9% were obtained for visible light and for X-rays between 10% and 12.5%. As shown, the energy resolution is better for lower gains and degrades for higher gains. For both X-rays and visible light the energy resolution starts to increase slowly above a gain of 100. This is related

to the increasing dark current at higher temperatures and, in any case, to the excess noise factor, as explained ahead.

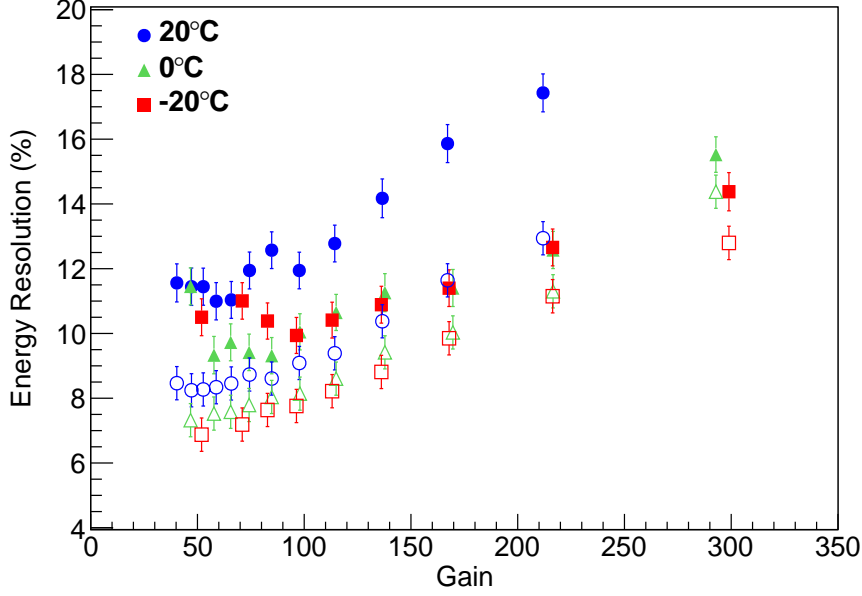


Figure 5.14: Energy resolution for 8 keV X-rays (closed symbols) and visible light pulses (open symbols) at different temperatures (20° C, 0° C and −20° C).

5.4.2 Electronic Noise

Figure 5.15 shows the electronic noise contribution (FWHM), in units of energy and in % to the energy resolution as a function of gain for different temperatures (0° C, −20° C and 20° C). To express the noise contribution in units of energy, the position of the 8 keV X-ray peak was taken for normalization. As seen, the electronic noise is strongly dependent on temperature, increasing for higher temperatures, and its variation with gain shows a minimum value which is 0.58 keV(7%), 0.26 keV(3.24%) and 0.13 keV (1.5%) for 20° C, 0° C and −20° C, respectively. For higher gains, the electronic noise increase is more pronounced for higher temperatures, as a result of the larger dark current. The behaviour of the noise contribution with gain and with temperature is coherent with the results reported in [49, 52].

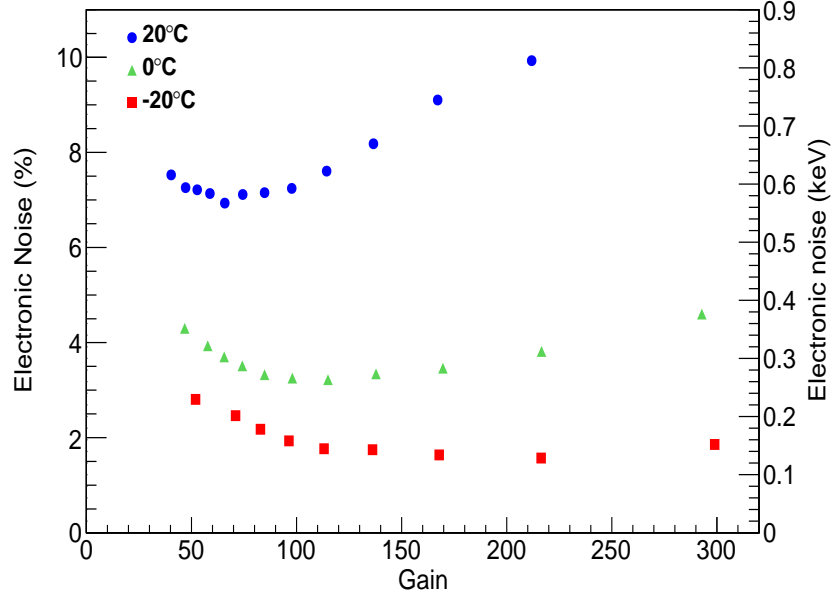


Figure 5.15: *Electronic noise contribution (FWHM) to the RT-APD energy resolution as a function of gain, for different temperatures, normalized to 8 keV.*

The dark current is another parameter that needs to be characterized due to its important contribution to the electronic noise and consequently to the energy resolution, compromising the detector's overall performance. As explained in chapter 3, the dark current (I_D) has two components, the superficial (I_{DS}) and the volumetric currents (I_{DV}), which sum up according to $I_D = I_{DS} + I_{DV}G$. The total dark current was registered for each bias voltage applied and for each temperature. The high voltage power supply has a precision of 1 nA for the dark current. Figure 5.16 shows the dark current behaviour with gain for each temperature for the $5 \times 5 \text{ mm}^2$ RT-APD. The respective components were obtained through a linear fitting to the dark current versus gain. As expected, the dark current has a strong dependence with temperature and gain. For each temperature the dark current increases with increasing gain, being more significant for gains higher than 200. For the lowest temperature tested (-20°C) the volumetric current is negligible. The dark

current dependence with temperature is very strong, affecting the overall detector's performance, which is much worse at higher temperatures.

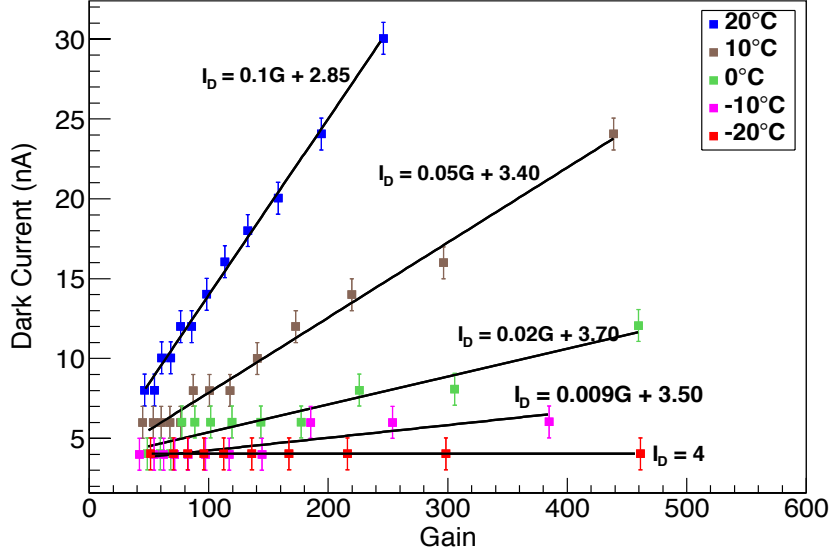


Figure 5.16: The dark current as a function of gain for the $5 \times 5 \text{ mm}^2$ RT-APD at different temperatures. The linear fitting of dark current values as a function of gain, for each temperature, gives the superficial and volumetric components.

Figure 5.17 shows the behaviour of the two dark current components as a function of temperature. The exponential dependence of the volumetric current with increasing temperature is noticeable, as reported in [43]. The superficial current shows some fluctuations but it tends to decrease with increasing temperature. Therefore, the dependence of the dark current on temperature is mainly associated with the volumetric component.

5.4.3 Intrinsic Resolution and Gain Non-Uniformity

The intrinsic energy resolution is a characteristic inherent to the APD. It is originated from statistical fluctuations associated to the number of electron-hole pairs produced

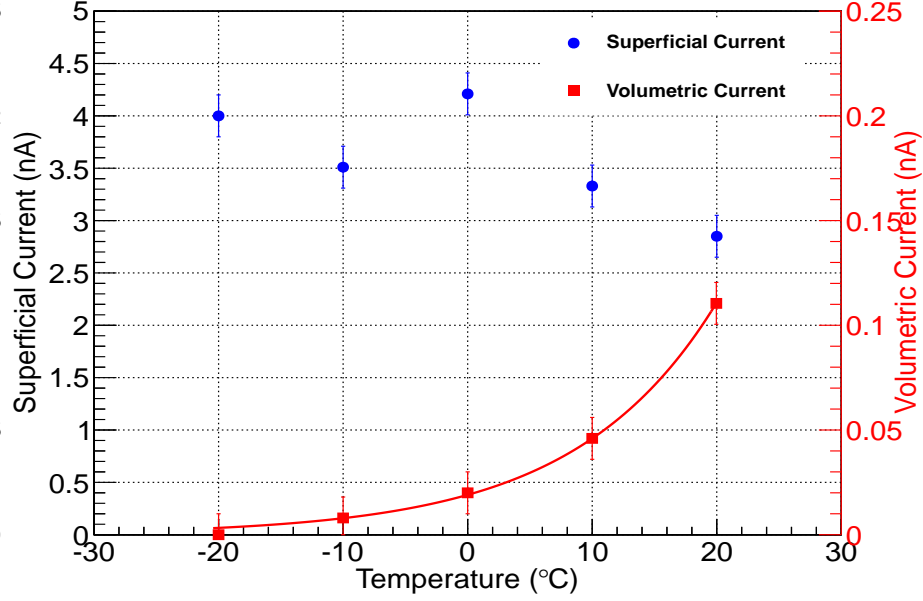


Figure 5.17: Dark current components, superficial and volumetric, as a function of temperature for the $5 \times 5 \text{ mm}^2$ RT-APD.

in the silicon volume and to the avalanche process. In X-ray detection, the gain non-uniformity in the avalanche region is also a major contribution to the intrinsic energy resolution.

Figure 5.18 shows the intrinsic energy resolution for 8 keV X-rays and visible light pulses with the same energy deposited as a function of gain obtained at 20°C , 0°C and -20°C , as well as the quadratic difference between the two curves. The contribution of the electronic noise was quadratically subtracted from the total energy resolution (fig. 5.14) to obtain the intrinsic energy resolution. As expected, the intrinsic energy resolution is larger for X-rays, as a result of the gain non-uniformity contribution. The quadratic difference between the energy resolution curves for 8 keV X-rays and visible light pulses, also shown in figure 5.18, is important to deduce the gain non-uniformity from equation (5.7).

The gain non-uniformity can significantly degrade the energy resolution for X-rays. This contribution was obtained as a function of gain, for temperatures of 20°C ,

0° C and −20° C, using equation (5.7) and the intrinsic energy resolution values of figure 5.18. The result is presented in figure 5.19, showing an average non-uniformity of $(\sigma_U/G) = 2.5\% \pm 0.4\%$, in good agreement with the results reported in [49, 53]. Nonetheless it is higher than the one reported in [23], of about 1.4%. The method used here is different from the one used in [43]. Our value is obtained indirectly from the energy resolution, with the whole detector area irradiated, the reason why it is an average value. It does not reflect the point-to-point variation of the gain, which may vary significantly across the detector area. The data points for higher gains at 20° C, shown in figure 5.19, deviate by more than their statistical uncertainties from the average value. The origin of these deviations is not known, although since the gain non-uniformity variation between different zones inside the Si wafer is a well understood process, this could be one possible explanation for the deviations obtained using this approach, but it is also not of relevance for the present investigations. For X-rays, the additional contribution of the non-uniformity causes deterioration of the energy resolution, more pronounced for higher gains, discussed below. In light detection, there is also energy resolution degradation with increasing gain. Nevertheless, for RT-APDs, this increase is more noticeable than the one reported in [51].

5.4. Contributions to the Energy Resolution

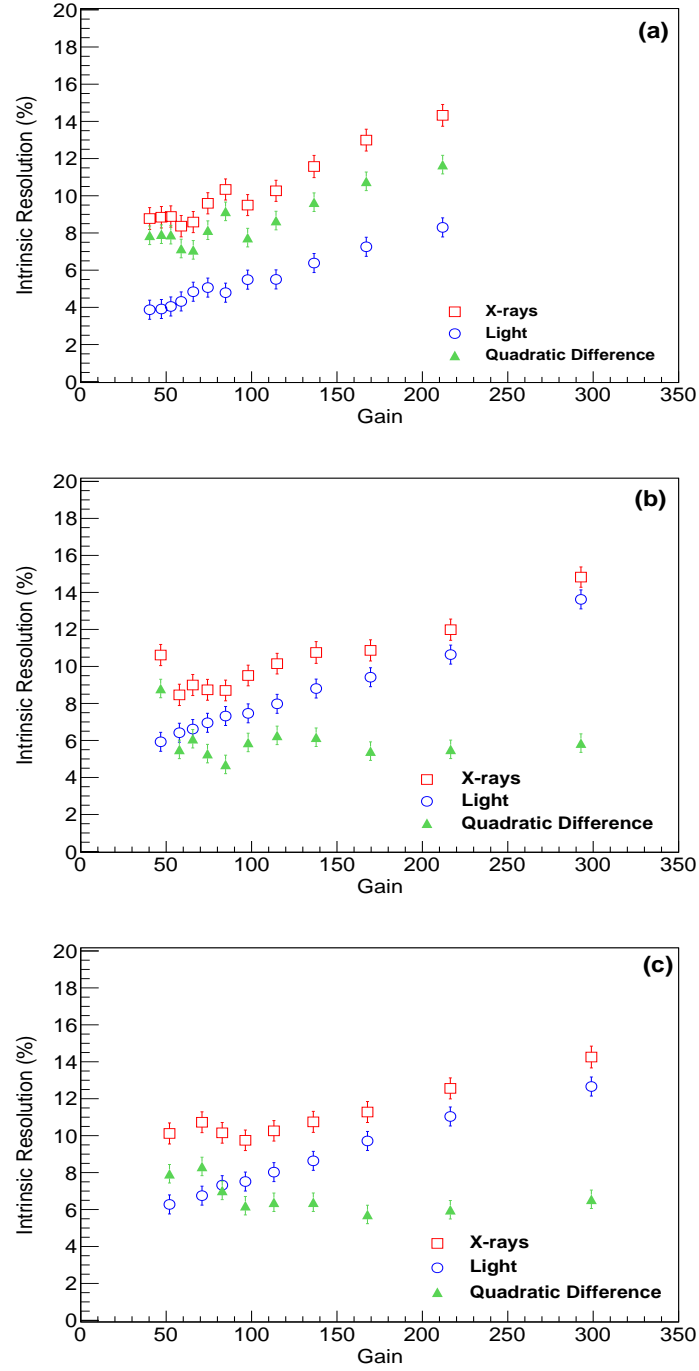


Figure 5.18: Intrinsic energy resolution for 8 keV X-rays and visible light pulses of the same energy as a function of gain obtained at (a) 20° C, (b) 0° C and (c) -20° C. The quadratic difference between the two curves is also shown.

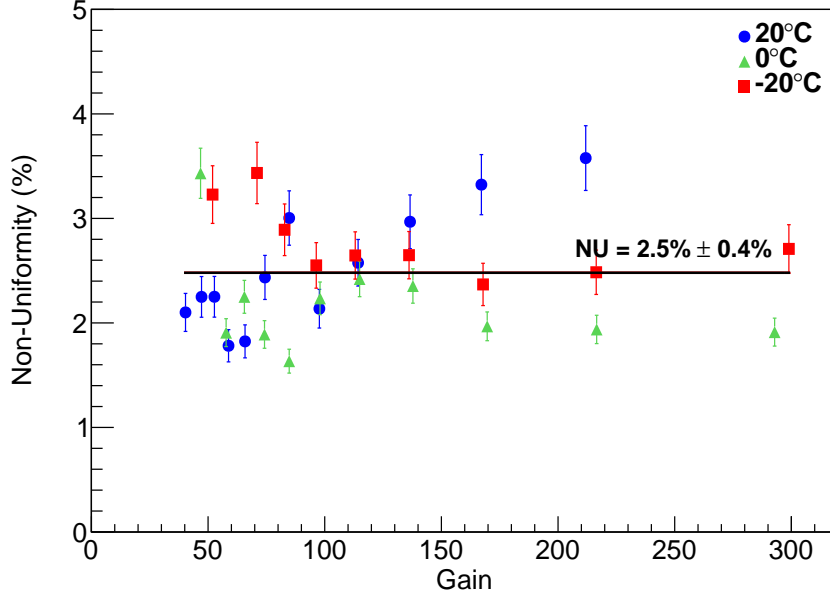


Figure 5.19: Gain non-uniformity (σ_U/G) obtained for three different temperatures, 20° C, 0° C and −20° C. The straight line shows the average of all points.

5.5 Excess Noise Factor

The excess noise factor (ENF) is an intrinsic characteristic of the APD [49, 51–53] and can be determined according to the equation:

$$\Delta E^2 = (\Delta E_n)^2 + (2.355)^2 F E \varepsilon, \quad (5.8)$$

where ΔE is the energy broadening of the visible light peak (FWHM, in units of energy), ΔE_n is the corresponding noise contribution (FWHM, in units of energy), $\varepsilon = 3.62 \text{ eV}$ is the mean energy to produce an electron-hole pair in silicon and E is the energy deposited in the silicon by a calibration radioactive source giving the same pulse height as visible light. Equation (5.8) results from equation (5.4) since $N = E/\varepsilon$.

5.5. Excess Noise Factor

ENF was determined using equation (5.8) as a function of the APD gain for different temperatures (-20°C , 0°C and 20°C), as shown in figure 5.20. As expected, ENF does not depend on temperature and increases with gain [49, 51, 52]. It is about 2 for gains below 80 and about 3.2 for a gain of 200. A linear fit to all measurements was made for gains above 50. The linear dependence between F and gain (G) is expressed by:

$$F = 0.009G + 1.42. \quad (5.9)$$

Comparing these results with those from the LAAPDs from RMD [53], for the same gain, F is almost twice as high for the RT-APD. For the same RT-APD structure, as reported in [23], for a gain of 60 at -20°C , they obtained about 2.5, a value slightly higher than ours.

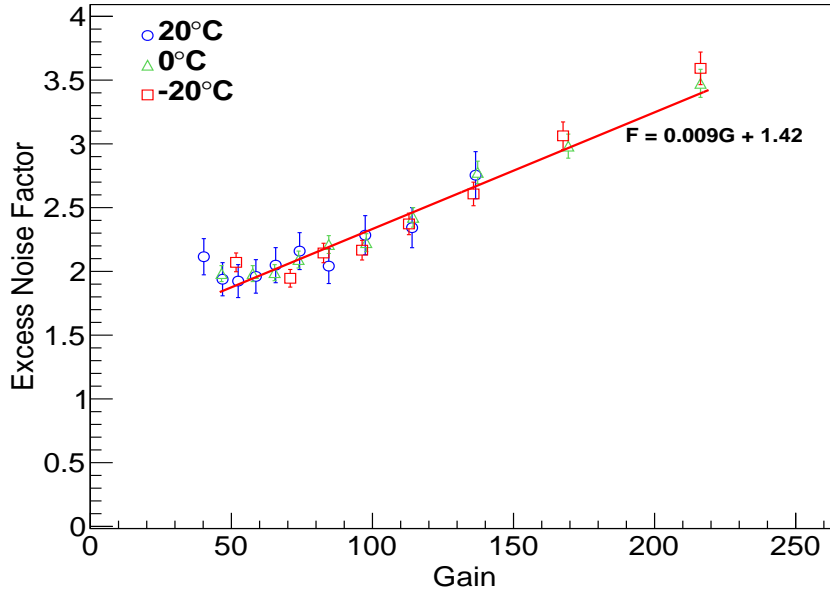


Figure 5.20: Excess noise factor (F) as a function of the APD gain (G), for different temperatures for the $5 \times 5 \text{ mm}^2$ prototype. The straight line represents a fit to all measurements for gains above 50.

5.6 Discussion

To summarize, two RT-APD prototypes from Hamamatsu, with $5 \times 5 \text{ mm}^2$ and $3 \times 5 \text{ mm}^2$ active areas, were investigated as low-energy X-ray detectors in order to evaluate their suitability for the muonic helium Lamb shift experiment. The best energy resolution achieved at room temperature was 11% for the larger prototype for a gain of 55. The energy resolution improves with decreasing temperature, reaching 9.5% at 0°C . The minimum detectable energy (MDE) improves with decreasing temperature and with increasing gain. The best value obtained is 0.25 keV; however, MDE is 0.9 keV in the gain region corresponding to the best energy resolution. The results obtained are similar to those reported in [23] for a round shape RT-APD with 3 mm diameter from Hamamatsu. Nevertheless, the behaviour is not exactly the same. The gain change with temperature increases with the applied bias voltage, varying between -1.0 % per $^\circ \text{C}$ and -1.7 % per $^\circ \text{C}$ when the bias voltage increases from 200 to 400 V. The gain non-linearity between X-rays and visible light pulses was also investigated, showing an increase with decreasing temperatures. In fact, for a gain of 200 V at -20°C , a gain non-linearity of 42% is obtained, whereas at 20°C it is only 30%. The excess noise factor was determined. The results obtained for the RT-APD with square area ($5 \times 5 \text{ mm}^2$) are in good agreement with those obtained and reported in [23]. Nonetheless, when comparing the ENF results with those from the LAAPDs from RMD [53], for the same gain, ENF is almost twice as high for the RT-APD. The non-uniformity was assessed. The result obtained is estimated in 2.5% in average, with a contribution to the energy resolution similar to the other ones reported in [53]. However, as the non-uniformity is highly dependent on the manufacturing process, differences between prototypes of the same series may be significant.

As a general conclusion, the RT-APD prototypes investigated have shown worse performance than the planar LAAPDs used before which have larger areas in order to maximize the solid angle inside the target. As a result, APDs from RMD were selected for the muonic helium Lamb shift experiment.

Chapter 6

The X-ray Detection System for the μ He Experiment

After the unfavourable results for RT-APDs from Hamamatsu Photonics, a detailed study of APDs from RMD for 8 keV X-ray detection was performed. This chapter is divided in two parts: one concerning the APD detectors themselves, and another concerning the new pre-amplifiers implemented in the experiment. Regarding the APDs from RMD, it is known that their efficiency for 8.2 keV X-rays is reduced to about 40 %, in comparison with about 90 % for 1.9 keV X-rays from muonic hydrogen [52]. A detailed characterization of all detectors, including detection efficiency, risetime, pulse shape, energy resolution and dependence on temperature, was carried out for 8 keV X-rays. Since the LAAPDs from RMD had already been investigated under intense magnetic fields and did not show any performance degradation [52, 53, 87], no further studies regarding the magnetic field were performed. Regarding the new pre-amplifiers, specifically designed and manufactured for our experiment by electronic technicians from the Swiss Federal Institute of Technology Zurich (ETH), a detailed study of several prototypes was performed and will be presented here. Two prototypes were tested, one with a single pre-amplifier and another one with an array of 5 pre-amplifiers. Optimal parameters were adjusted.

The signal shape, rise time, noise behaviour, pre-amplifier bias voltage and signal-to-noise ratio were determined and compared with the previous pre-amplifiers in view of their use in the new experiment.

6.1 Avalanche Photodiode for X-ray Detection

APDs from RMD were already used in the μH Lamb shift experiment [7, 9]. They presented, for temperatures below 0°C and for 2.3 keV X-rays, an average energy resolution below 25% [54]. For 8.2 keV X-rays, the detection efficiency drops by a factor of 2 due to the thin depletion region. Nevertheless this limitation is tolerable for the μHe experiment, since the lifetime and population of the 2S-state [22] are higher when compared to that of muonic hydrogen. The expected rate of 8 keV X-rays in resonance with the laser wavelength for $\mu^4\text{He}^+$ is 48 signal events per hour when compared to 6 signal events per hour maximum for μH [22].

6.1.1 Experimental Setup for APD Tests

The radioactive source used to investigate the response of RMD APDs was ^{65}Zn [96, 97], emitting X-rays of energies $K_\alpha = 8.0\text{ keV}$ and $K_\beta = 8.9\text{ keV}$. Table 6.1 shows the main decay products of the source, mainly by electron capture accompanied by the emission of X-rays of 8 keV and 8.9 keV, and gamma-ray photons of 1115 keV. Assuming $K_{\alpha 1}$ and $K_{\alpha 2}$ as one energy peak, since they are very close to each other, the relative K -line intensities are given by $I_\beta = 0.14 I_\alpha$ [96].

The experimental setup used for APD tests is schematically shown in 6.1 and is composed by:

- ^{65}Zn source;
- two series of 10 LAAPDs each from RMD;
- 20 RAL 108 A low-noise charge-sensitive pre-amplifiers [55];

Table 6.1: *The main types of radiation emitted during the ^{65}Zn decay [96].*

Contributions	Energy (keV)	Intensity per decay(%)
K X-photons		
$K_{\alpha 2}$	8.03	11.76(13)
$K_{\alpha 1}$	8.05	22.91(23)
K_{β}	8.91	4.82(7)
Auger electrons		
K-Auger	6.76-8.9	47.5(4)
L-Auger	0.7-1.0	126.7(6)
γ -Photons		
γ_1	1115.56(4)	50.60(22)
γ_2	511	2.84(4)
Conversion electrons	1106	0.0084

- one ORTEC spectroscopy amplifier [92];
- one multi channel analyser (Pocket-MCA 8000A) [93].

Photodiodes are very sensitive to light, including environment light, which increases the background, overlapping with the X-ray detector signal. To prevent this and for cooling purposes, the source, the detectors and the pre-amplifiers were placed inside a vacuum chamber. To move the source from one detector to another, a vacuum feedthrough was attached to it. The two arrays of large area avalanche photodiodes were designated as array A and array B, respectively. Each array is composed by 10 detectors and 10 pre-amplifier channels, with the respective number (starting from #0 to #9, depending on their location in the array, as seen in figure 6.2). The signal was then carried to a linear amplifier with shaping time constants (integration and differentiation) of $0.5\mu\text{s}$ and a fixed gain of 200. At the end of the amplifier there are two outputs, one for energy studies connected to a multi-channel analyser with acquisition time of 1800 seconds (figure 6.1), and another for rise time and signal shape analysis directly connected to the oscilloscope.

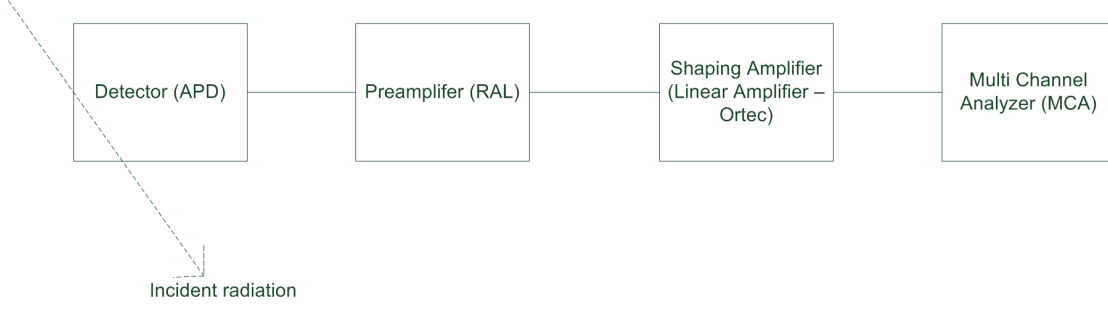


Figure 6.1: Schematic diagram showing the experimental setup used during measurements. The detectors and pre-amplifiers are inside a vacuum chamber and the other electronic devices are outside.

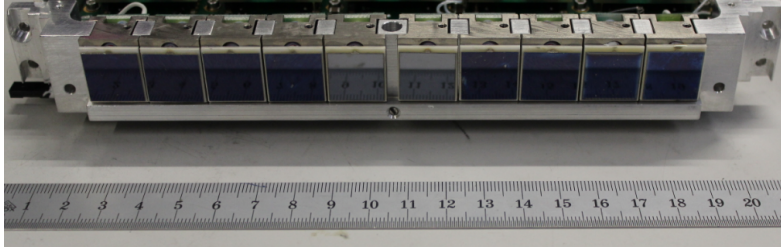


Figure 6.2: Array of 10 LAAPDs to be tested inside the vacuum chamber.

For these studies, two different holders for the ^{65}Zn source were used, one with a hole collimator of 1 mm diameter for detection efficiency studies (explained later), and another with no collimation for the remaining studies, as seen in figures 6.3 and 6.4.

The source activity at the time of the measurements was 2.3×10^5 cts/s. The respective solid angle considering the distance between the source and the top of the collimator of 23 mm is (see figure 6.3):

$$\frac{\Omega}{4\pi} = 0.5 \times \left(1 - \cos\left(\arctan \frac{5}{23}\right)\right) = 1.142 \times 10^{-2} \text{sr} \quad (6.1)$$

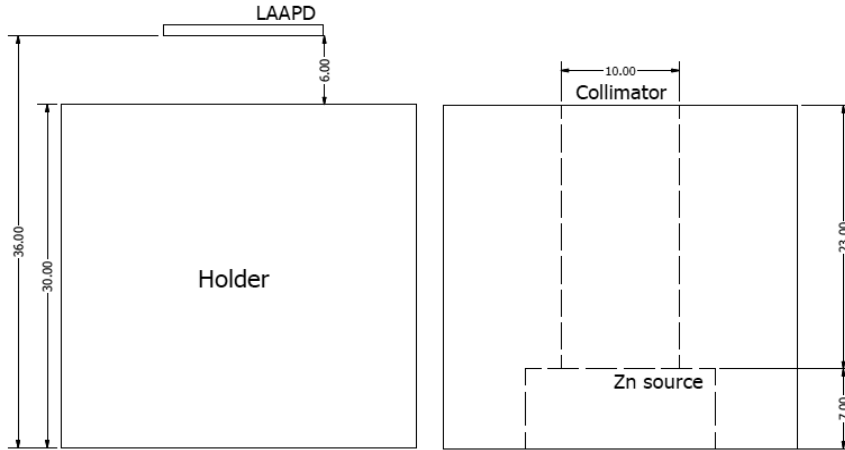


Figure 6.3: Holder for the ^{65}Zn source with a collimator of 10 mm diameter to determine the detection efficiency for all detectors. All the dimensions are given in mm.

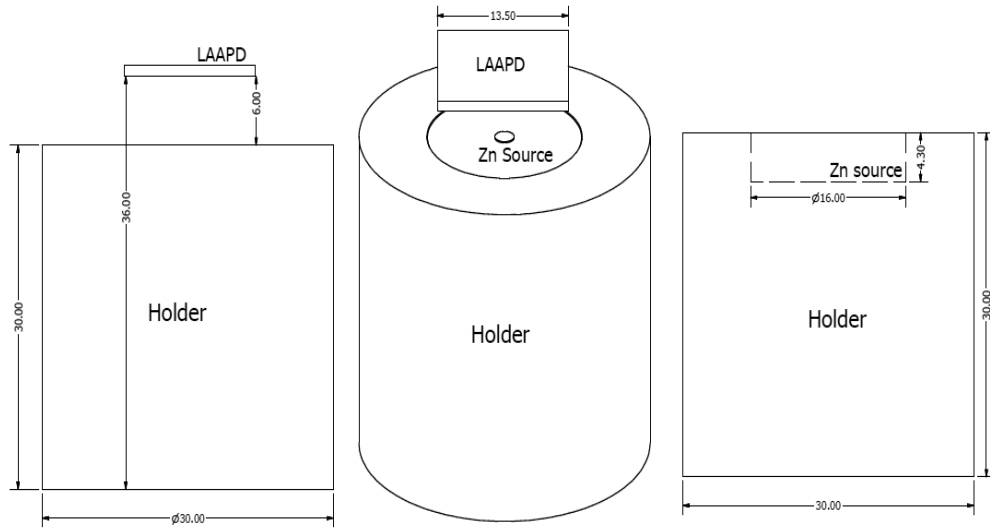


Figure 6.4: Holder for the ^{65}Zn source with no collimation for energy resolution measurements. All the dimensions are given in mm.

6.1.2 Preliminary Tests

A selection of 20 APDs used in the muonic hydrogen Lamb shift experiment was made for a preliminary test as 8 keV X-ray detectors. The voltages applied to the APDs

were slightly lower than those used during the run in 2009, 20 V less in each detector, in order to prevent irrecoverable damages. Consequently, they were not operated in the best gain region. Operational parameters, such as high voltage, dark current and rise time were measured and are listed in table 6.2. The energy resolution was determined for each LAAPD and is also listed in table 6.2. The pulse rise time after the pre-amplifier was found to be 100 – 200 ns, similarly to the values obtained in the 2009 run for 1.9 keV X-rays. The definition adopted for the rise time is the time interval between 10% and 90% of the signal amplitude. The dark current values are consistent with the ones measured in the 2009 run.

In figure 6.5, the energy spectra from the 20 LAAPDs tested are plotted for the bias voltages reported in table 6.2. During the data acquisition A0 presented fluctuations in the dark current from 5 nA up to 200 nA. Some discharges were also observed, compromising the detector's overall performance. Detector A4 showed a strange rise time behaviour composed by two different stages. Up to 60 % of the signal amplitude, the rise time measured was 100 ns, increasing to about 2 μ s (round-shape). A8 presented a larger asymmetry on the left part of the 8 keV X-ray peak which is not quite well visible in the plot.

Concerning array B, during the data acquisition phase, a larger noise level was observed at the pre-amplifier's output. The noise and pick up were attenuated when the pre-amplifier was connected to the amplifier. It was perhaps due to ground connections, since it was a general behaviour for array B. The spectrum from B9 is the widest and the most asymmetric one. The peak asymmetry in the right part is clearly the K_β X-ray line from the ^{65}Zn source (8.9 keV). Regarding the dark current, as seen in table 6.2, B7 and B9 APDs present the highest values from all 20 APDs. Nonetheless, the dark current values are consistent with the ones measured during the 2009 run, even for those detectors. The tail observed in the left part of all spectra may be due to radiation absorption directly in the avalanche region of the LAAPD, resulting in fast and partially amplified signals, with lower gain and thus lower amplitude. Some pulses from the tail may have origin in X-rays absorbed in

6.1. Avalanche Photodiode for X-ray Detection

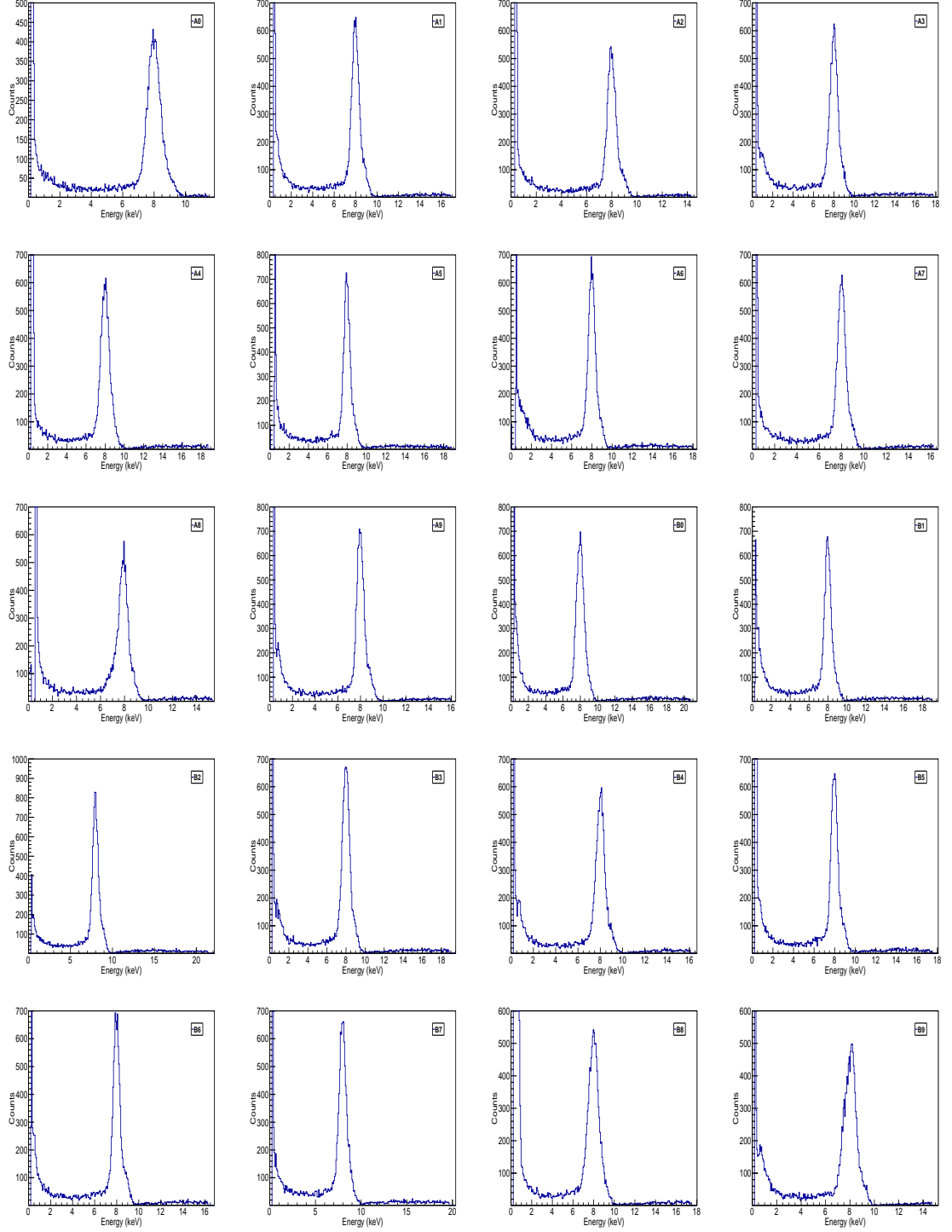


Figure 6.5: Energy distributions obtained with 20 APDs tested, from arrays A and B, for 8 keV X-rays at -30°C . The bias voltages applied are listed in table 6.2.

Table 6.2: Operational characteristics for 20 APDs used during the μp experiment in 2009. The temperature was maintained constant at -30°C . Rise time and energy resolution values were obtained for 8 keV X-rays signals.

Position	HV(V)	DC(nA)	Rise Time(ns)	En. Res.(%)
A0	1600	5	100	13.0
A1	1660	2	150	11.5
A2	1600	3	200	11.0
A3	1600	2	100	12.3
A4	1600	3	2000	13.6
A5	1600	4	100	11.0
A6	1600	3	150	10.4
A7	1600	3	150	11.8
A8	1600	4	100	11.2
A9	1660	4	150	9.5
B0	1660	2	100	13.1
B1	1660	2	100	11.6
B2	1600	2	100	11.8
B3	1600	3	100	11.8
B4	1600	2	150	11.0
B5	1600	3	150	10.1
B6	1600	3	100	8.9
B7	1660	14	100	11.6
B8	1660	3	100	11.6
B9	1660	22	100	16.2

the drift layer of the APD. As a result, part of the electrons created in the silicon may recombine before drifting to the multiplication region.

The energy resolution for 8 keV X-rays was determined. The best value obtained was 8.9% for B6. The worst values of 13.6%, 13.1% and 16.2% were obtained in A4, B0 and B9, respectively. The values attained are consistent with those from the 2009 run. After a few months without working, the APDs have shown a remarkably consistent behaviour, with no relevant ageing effects.

6.1.3 Detection Efficiency

The detection efficiency of a large area avalanche photodiode from RMD is about 40% for 8 keV X-rays. The detection efficiency is the fraction of X-rays incident in the detector active area which originates a detectable signal. The total detection efficiency of a LAAPD in the experiment is given by:

$$\epsilon_t = \Omega \epsilon_d, \quad (6.2)$$

where Ω is the solid angle subtended by the detector and the source position, and ϵ_d is the X-ray detection efficiency, which is energy dependent.

Selecting a detector with known efficiency for 8 keV X-rays, for example the Si-PIN XR-100CR detector from AmpTek [98], in the same experimental conditions as the LAAPD, both with the same solid angle, the APD efficiency can be determined from the ratio between the count rates for useful signals detected in the APD and the Si-PIN detector. The holder used for this purpose, shown in figure 6.6, was made with a 1.1 mm diameter hole because the SI-PIN detector has an active area between 6 mm² and 25 mm² (notice that this was not made clear from the available specifications). The respective solid angle, given the distance between the source and the end of the collimator, of about 16.2 mm, is:

$$\frac{\Omega}{4\pi} = 0.5 \times (1 - \cos(\arctan \frac{0.55}{16.2})) = 2.879 \times 10^{-4} sr. \quad (6.3)$$

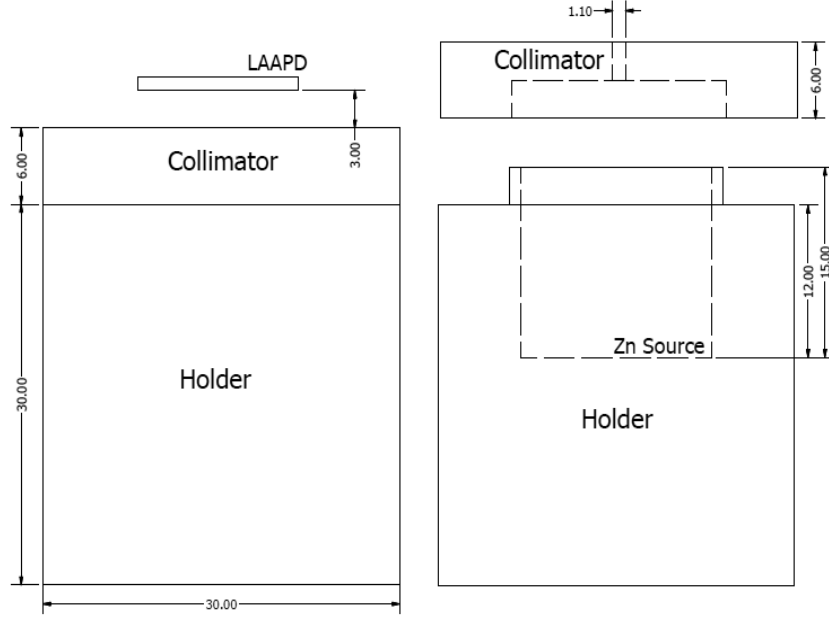


Figure 6.6: Holder used to determine the detection efficiency of an APD from RMD with 1.1 mm collimator diameter was used. All the dimensions are given in mm.

6.1.3.A Response of the Si-PIN Detector

The Si-PIN detector has approximately a 100% efficiency for 8 keV X-rays, as seen in figure 6.7. The main specifications of the detector are listed in table 6.3.

Table 6.3: Relevant specifications for Si-PIN detectors from AmpTek [98].

Detector Type	Si-PIN
Detector Size	From 6 mm ² to 25 mm ²
Silicon Thickness	300 μm and 500 μm
Collimator	Multilayer
En. Resolution for 5.9 keV	145 eV to 230 eV (FWHM)
Background Counts	$< 3 \times 10^{-3}/s$
Detector Be Window Thickness	25 μm or 12.5 μm
Charge Sensitive pre-amplifier	Amptek custom design
Gain Stability	$< 20\text{ppm}/^\circ\text{C}$ (typical)
Case Size	$7.6 \times 4.4 \times 2.9$ cm

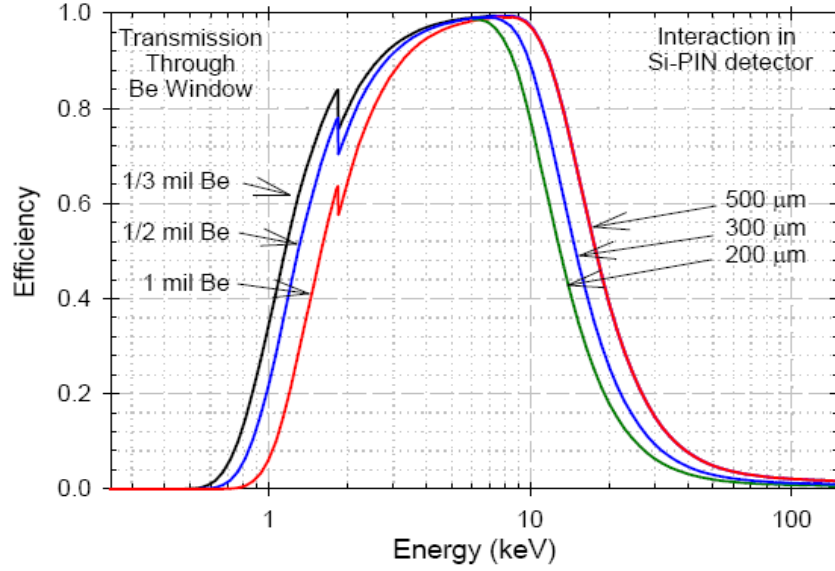


Figure 6.7: The intrinsic full energy detection efficiency for the XR-100CR detector.

The ^{65}Zn source and the holder with the collimator were placed in front of the Si-PIN detector and aligned with the centre of its active area. The Si-PIN detector was biased to 200 V. As seen in the energy distribution shown in figure 6.8, there are no significant tails to the left and to the right of the 8 keV peak, contrasting with the distributions obtained with the APD (see figure 6.5). This is due to an efficiency of almost 100 % for 8 keV. For calculation purposes, an efficiency of 98 % for 8 keV was assumed (see figure 6.7). The small peak just before the 8 keV peak is due to a slow charge collection time, since there are few charges originated near the back contact of the undepleted detector [98]. The two peaks from the ^{65}Zn source, K_α and K_β , with 8.0 and 8.9 keV energies, respectively, are well distinguished in comparison to the spectrum obtained with the LAAPDs (figure 6.5).

The count rate obtained for the 8 keV peak was 5.87 cts/s. Taking both peaks into account (8 and 8.9 keV peaks), the total count rate attained, discarding the small peak before the 8 keV, was 6.18 ± 0.02 cts/s.

A scan along the active area of the Si-PIN detector was performed in order to verify the influence of the source's position in the detector's efficiency. A mechanical

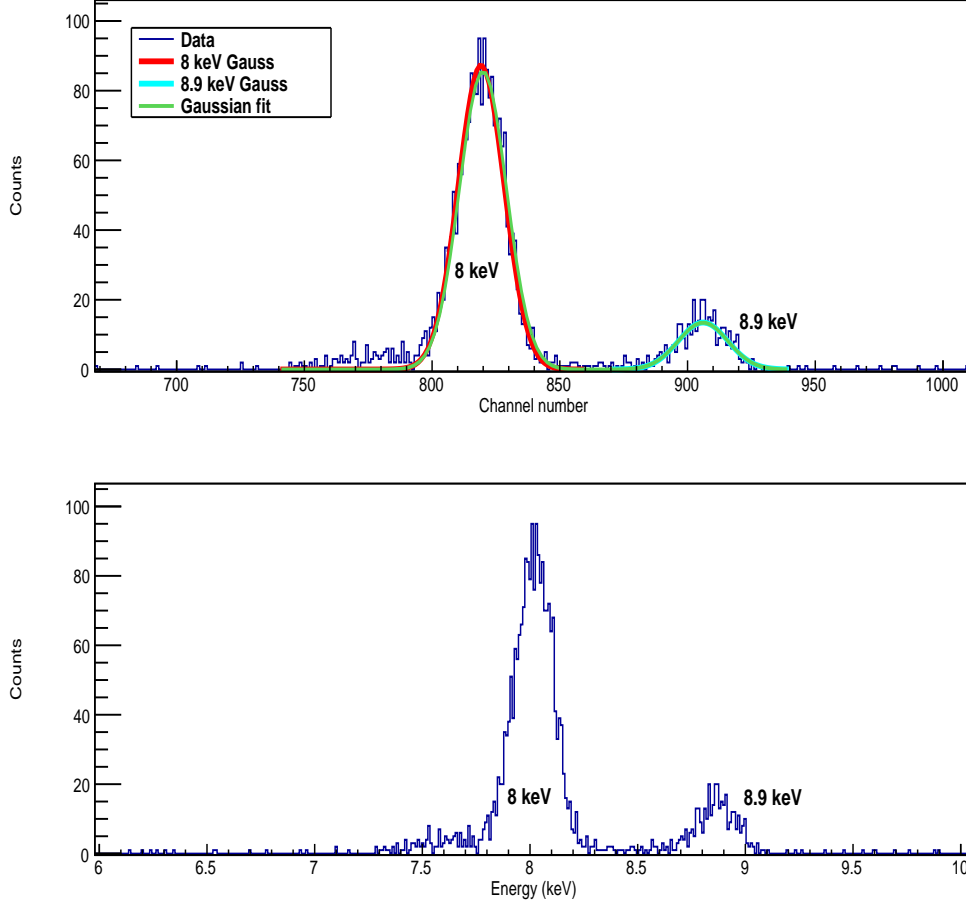


Figure 6.8: Energy spectrum for the Si-PIN detector for X-rays from a ^{65}Zn source at room temperature and a bias voltage of 200 V. The red line is the Gaussian fit to the 8 keV peak, the blue line is the fit to the 8.9 keV peak and the green line is the fit to the total distribution. Bottom figure is normalized to the energy.

table was used for stabilization and precise measurements. However, it was only able to move along one direction (X axis). As seen in figure 6.9, the efficiency decreases as the distance to the centre increases. Assuming a circular detector with a sensitive area of 6 mm^2 , corresponding to a diameter of 2.8 mm, it is expected that the efficiency stays at 98 % within $\pm 0.7\text{ mm}$ and then drops down to 0 % within $\pm 2.1\text{ mm}$. The data points approximately agree with this expectation, except for the two points at

6.1. Avalanche Photodiode for X-ray Detection

$\pm 0.5\text{ mm}$ which are at 96 %, probably due to non-uniformities over the detector's surface.

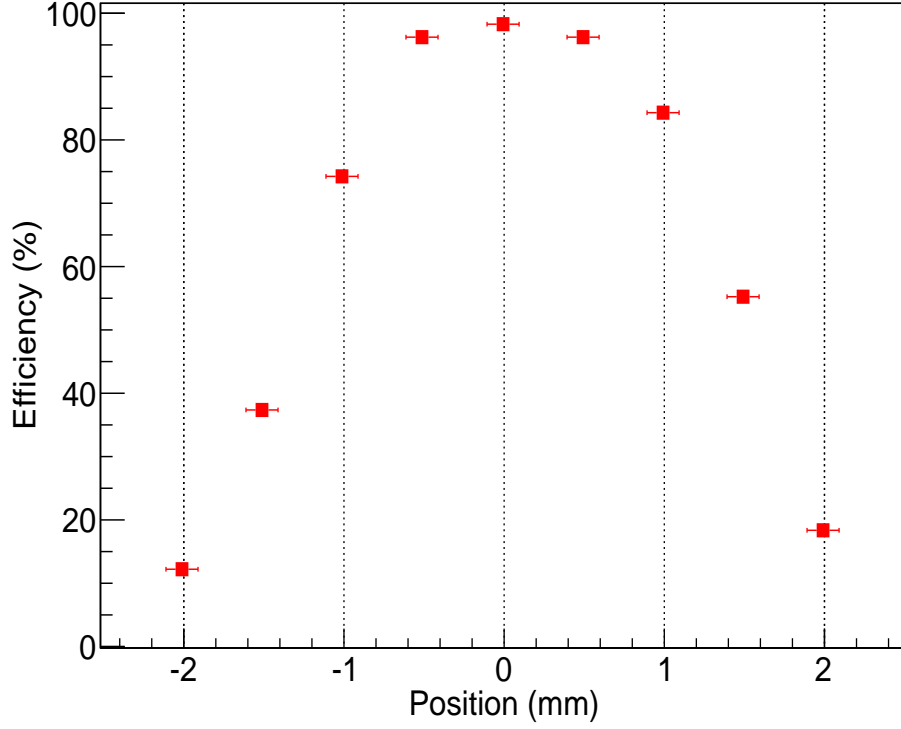


Figure 6.9: Detection efficiency of the Si-PIN detector as a function of the source position relative to the centre of the detector along the X axis.

6.1.3.B Response of the Avalanche Photodiodes

The APD selected for this study was B6 in table 6.2, due to its good result for energy resolution. The areas under the 8 keV and 8.9 keV peaks were determined in order to estimate the absolute efficiency (see figure 6.10). The low energy tail observed is an intrinsic feature of the LAAPD. It arises either from the partial collection of the charges created in the detector by the incident X-ray, or from the interaction of the X-ray in the vicinity or inside the avalanche region, leading to non-fully amplified pulses. The fitting method implemented used two Gaussian functions, one for $K_{\alpha} = 8\text{ keV}$

and another for $K_\beta = 8.9\text{ keV}$, as well as a Gaussian complementary error function, representing the low energy tail.

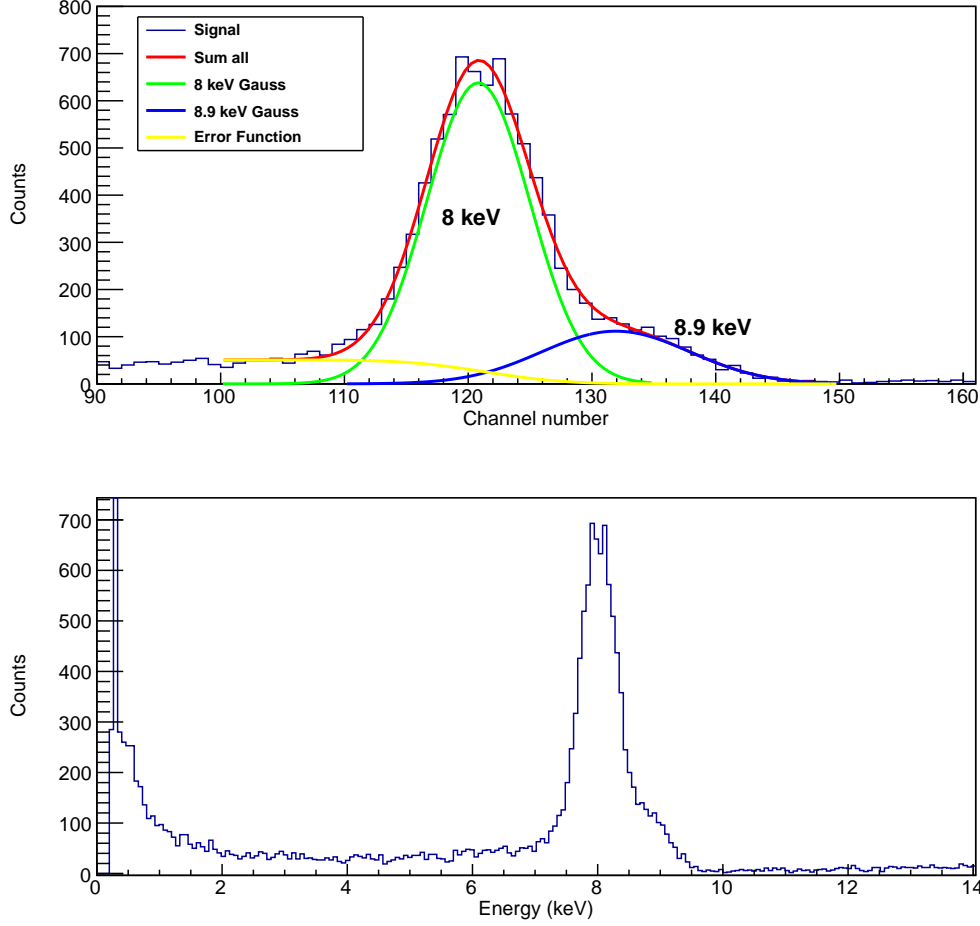


Figure 6.10: Energy spectrum for the B6 APD at -30°C with no collimator. Two Gaussian functions were fitted to the 8 keV and 8.9 keV peaks, together with a Gaussian error function to account for useful events with smaller amplitudes.

A new spectrum was obtained for the collimator with 1 mm diameter. The acquisition time for the spectrum of figure 6.11 is 3600 s and the detector was polarized with a bias voltage of 1600 V. The fitting method was similar to the one used previously with no collimator. However, two more functions were needed: a linear function for higher amplitudes, to the right of the 8.9 keV peak, and a constant

function (as shown in figure 6.11). In total, 5 functions were fitted: a Gaussian for the 8 keV peak (green), a Gaussian for the 8.9 keV peak (blue), a Gaussian error function (yellow), a flat background (pink) and a linear function (purple) to subtract high-energy background.

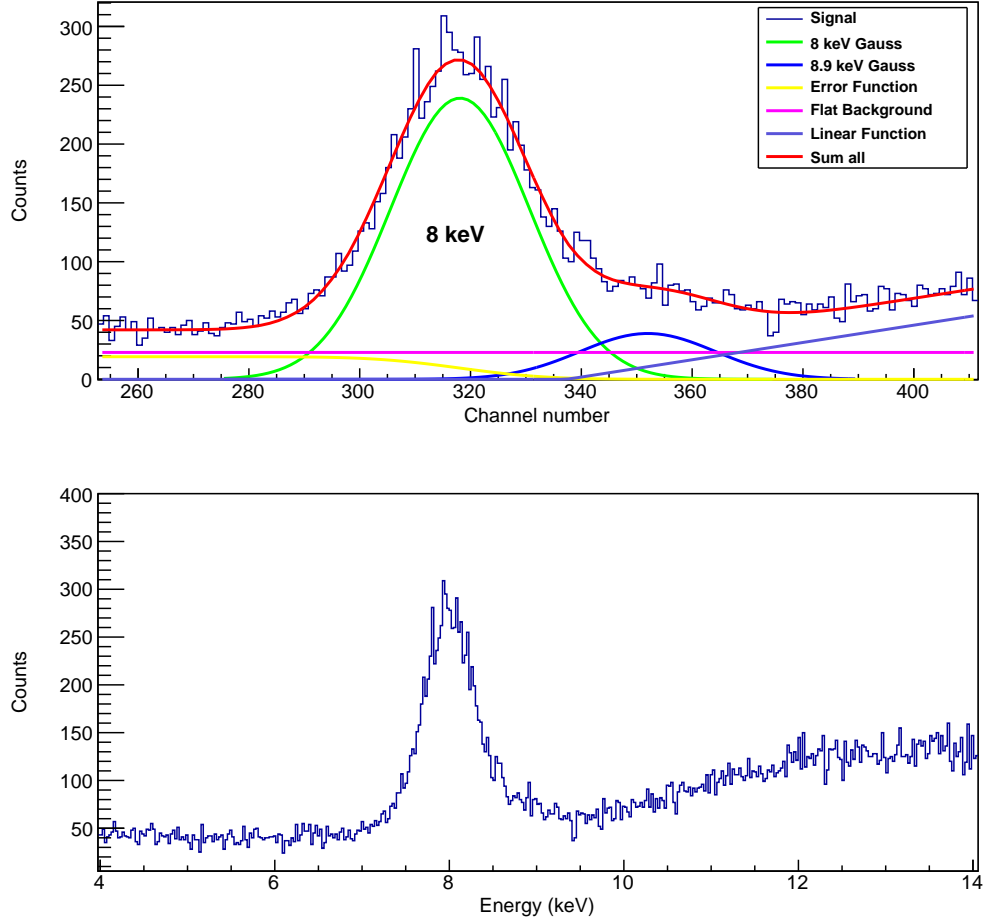


Figure 6.11: Energy spectrum obtained in the APD B6 using the collimator with 1.1 mm diameter at -30°C . Two Gaussian functions were fitted to the 8 keV and 8.9 keV peaks, together with a Gaussian error function, a constant function and a linear function to account for background events.

When comparing figures 6.11 and 6.10, we observe that the spectrum with the collimator presents a higher background in the high energy region. This is due to

the secondary process from high energy gammas emitted by the ^{65}Zn source, which penetrate the aluminium piece (collimator). The area estimated under the 8 keV and 8.9 keV peaks is 9457 counts, corresponding to a rate of 2.63 ± 0.04 cts/s.

6.1.3.C Analysis

Assuming an efficiency of 98% for the Si-PIN detector at 8 keV, and considering the count rate obtained of 6.18 ± 0.02 cts/s, a count rate of 2.63 ± 0.04 cts/s in the APD corresponds to a detection efficiency of $41.7 \pm 1.5\%$, assuming a 0° incident angle (normal incidence). It is important to note that the total area determined for the LAAPD using the ^{65}Zn source was for both 8 keV and 8.9 keV peaks. Therefore, the efficiency calculation takes into account the sum of the two K-lines in both detectors.

The sum of 8 keV and 8.9 keV events measured in each APD (without collimator) was determined from a fit of the corresponding energy spectrum similar to the one shown for B6 in figure 6.10. The absolute efficiency was determined by comparing the results obtained for all LAAPDs with the already determined result for APD B6, as seen in table 6.4.

The LAAPD's detection efficiency depends strongly on the thickness of the drift region inside the detector and on the X-ray energy. The total X-ray detection efficiency is given by:

$$\varepsilon = [1 - e^{-\frac{\bar{A}d}{\lambda(E_x)}}], \quad (6.4)$$

where \bar{A} considers the effect of the angular distribution (corresponding to an average angle α , at which the X-rays reach the LAAPD surface according to $\bar{A} = 1/\cos \alpha$), d the thickness of the drift region, and λ the attenuation length in Si at the X-ray energy E_x [27]. Taking into account the B6 APD efficiency measured of $41.7 \pm 1.5\%$ for 8 keV X-rays, considering $\bar{A} = 1$ and $\lambda = 75\mu\text{m}$ (see figure 6.12), using equation 6.4, a value of $40.5\mu\text{m}$ for d is obtained. However, the angular distribution parameter for the muonic helium Lamb shift is equal to 1.60 ± 0.05 (assuming the same values as the

Table 6.4: Count rates and efficiencies for 8 keV X-rays attained in all APDs from array A and array B. The parameter \bar{A} considers the effect of the angular distribution.

Array#LAAPD number	Cts/sec	Effic. $\pm 1.5(\%)$ [$\bar{A}=1$]	Effic. [$\bar{A}=1.6$]
A0	99.31	44.8	62.3
A1	94.12	42.5	59.1
A2	88.52	40.0	55.7
A3	91.69	41.4	57.6
A4	97.89	44.2	61.5
A5	87.60	39.6	55.1
A6	93.48	42.2	58.7
A7	97.33	43.9	61.1
A8	98.21	44.3	61.6
A9	95.79	43.3	60.3
B0	95.23	43.0	59.8
B1	84.63	38.2	53.2
B2	90.32	40.0	55.7
B3	94.23	42.6	59.3
B4	93.02	42.0	58.5
B5	86.70	39.2	54.6
B6	92.38	41.7	58.0
B7	91.68	41.4	57.6
B8	100.87	45.5	63.3
B9	103.25	46.7	65.0

ones of muonic hydrogen), as Monte Carlo simulation showed previously [27], leading to a different value for the detection efficiency for 8 keV X-rays.

Therefore, for an angular distribution of $\bar{A} = 1.6$ and $\lambda = 75\mu m$, the efficiency achieved for the 8 keV peak is 58.0 % for APD B6. Since the efficiency was determined for the whole area under the peaks (8 keV and 8.9 keV), the average energy is not 8 keV, but approximately 8.1 keV. The small difference between this energy and the μ He X-ray energy, of about 8.2 keV, can be neglected.

Figure 6.13 shows the resulting efficiencies for all APDs and the two relevant distributions of incident angles, corresponding to $\bar{A} = 1.0$ for source measurements and $\bar{A} = 1.6$ for μ He measurements. The resulting efficiencies, averaged over all APDs

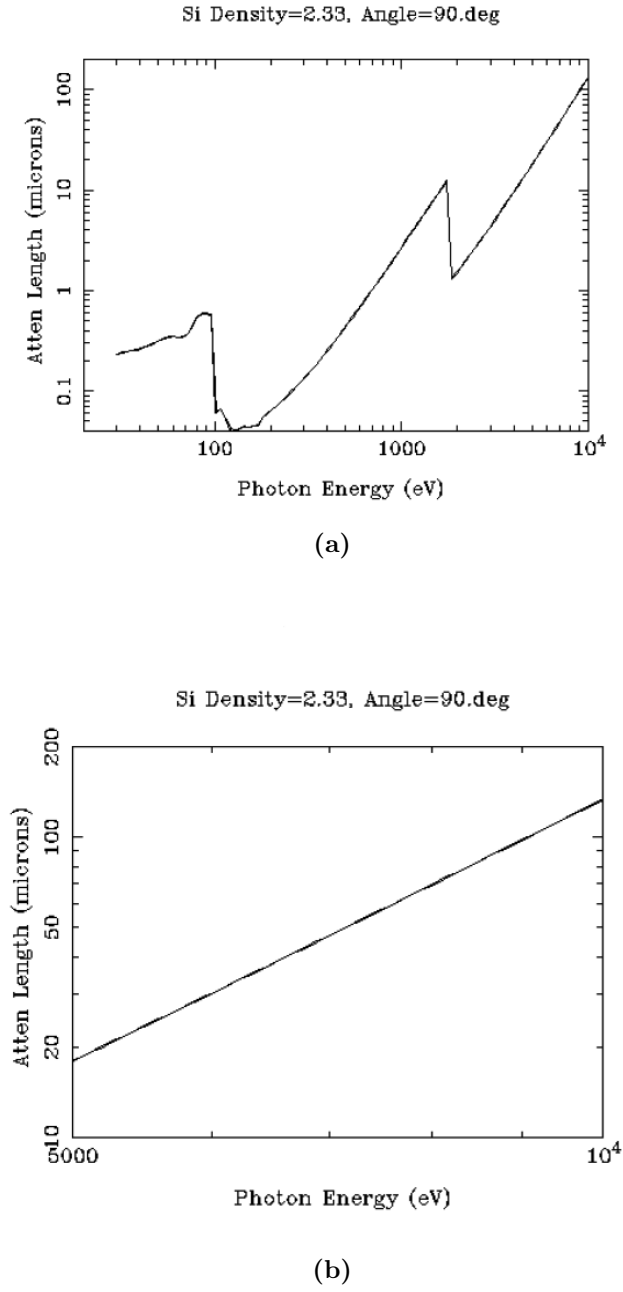


Figure 6.12: (a) Photon attenuation length in silicon as a function of energy. (b) X-ray attenuation length in the region 5 – 10 keV [99].

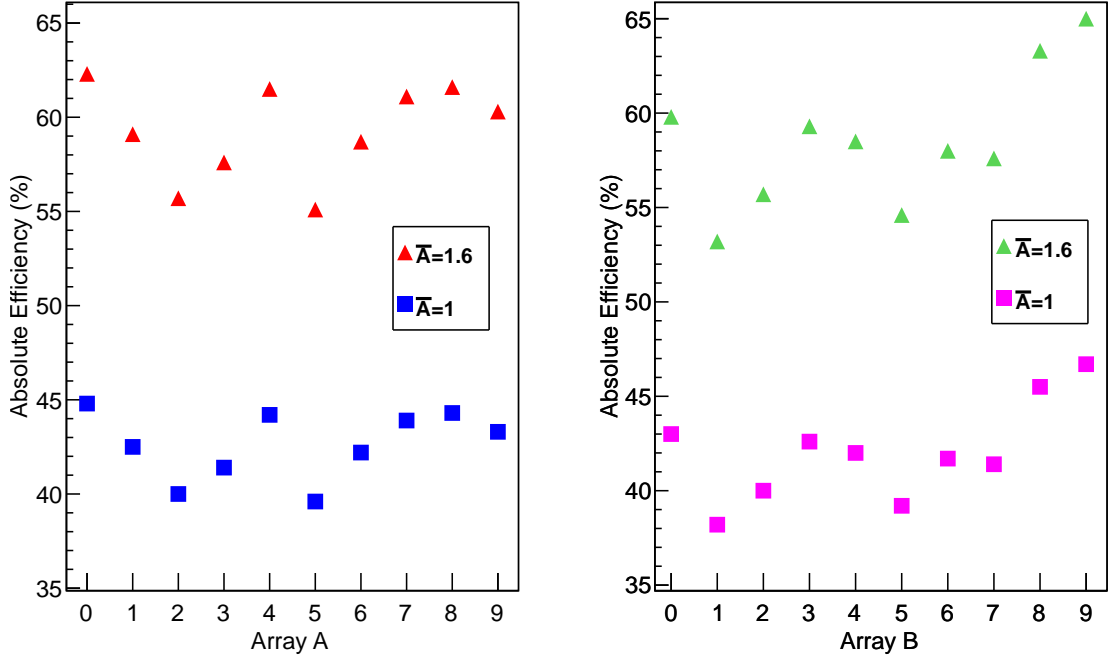


Figure 6.13: Absolute efficiency (%) versus APD number in the respective array, A or B, obtained for $\bar{A} = 1$ and $\bar{A} = 1.6$ for 8.2 keV X-rays.

are 42.3 ± 1.5 %, for $\bar{A} = 1$, and 58.9 ± 1.5 % for $\bar{A} = 1.6$. The latter looks favourable for the μHe Lamb shift experiment.

6.1.4 Spatial Non-Uniformity

The non-uniform resistivity through the Si wafer of the LAAPD induces local gain variations, consequently affecting the energy resolution and the detector overall performance. This parameter was investigated for LAAPDs B1, B2 and B6 polarized to nominal bias voltages of 1680, 1620 and 1620 V, respectively. The gain non-uniformity was obtained using a collimator with 1 mm diameter in 5 points distributed along one diameter of the detector's active area, one in a central position, 2 at 0.2 cm from the centre, and 2 points at 0.5 cm from the centre.

Table 6.5: *Distribution of the normalized amplitude for 8 keV X-rays using the 1 mm diameter collimator placed along the X axis of the detector active area in 5 different points.*

LAAPD	Normalized Amplitude						σ
	0.98	0.99	1	1.01	1.02	1.03	
B1	0	2	1	2	0	0	0.009
B2	2	1	0	1	0	1	0.022
B6	1	0	2	2	0	0	0.012

The gain distributions for the three APDs were obtained normalizing the amplitudes to the average value, as seen in table 6.5, and counting the number of values in intervals of 0.01. The X-ray pulse amplitudes have fluctuations of about $\pm 1\%$, $\pm 3\%$ and $\pm 2\%$ for B1, B2 and B6, respectively, due to non-uniformities. For LAAPD B1, all the values are within $\pm 1.5\%$ of the average. Nevertheless, for the APD B2 more than 50% of the amplitudes are located outside this range. The standard deviation associated to the amplitude fluctuations was also determined. This values cannot be seen as the APD overall gain non-uniformity since it is an average of 5 points only, not describing the uniformity over the whole active area of the APD. In any case, the values obtained, between 1 and 2.2%, give an idea of the order of magnitude of the non-uniformity. Nevertheless, these values are in good agreement with those reported in [49, 53, 95].

6.1.5 Energy Resolution for 8 keV X-rays

For all LAAPDs, the X-ray distribution was fitted to two Gaussian functions, one for the 8 keV peak and another one for the 8.9 keV peak. A typical example is shown in figure 6.10. No background was considered. The centroid and the FWHM of each Gaussian distribution were determined, and consequently the energy resolution. The

6.1. Avalanche Photodiode for X-ray Detection

bias voltage applied was between 1580 V and 1660 V, and dark currents between 4 and 10 nA were measured, depending on the detector.

Table 6.6: *Best energy resolution obtained for 8 keV X-rays for APDs from array A and array B at -30°C .*

LAAPD	En. Resolution (%)
A0	13.0
A1	11.5
A2	11.0
A3	12.3
A4	13.6
A5	11.0
A6	10.4
A7	11.8
A8	11.2
A9	9.5
B0	13.1
B1	11.6
B2	11.8
B3	11.8
B4	11.0
B5	10.1
B6	8.9
B7	11.6
B8	11.6
B9	16.2

Table 6.6 shows the best energy resolution obtained for 8 keV X-rays for each APDs. As seen here, all the values for the energy resolution are between 9% and 16% at -30°C . The majority of the detectors have energy resolution values between 11% and 13%, and few of them have the best energy resolution attained, of about 9%.

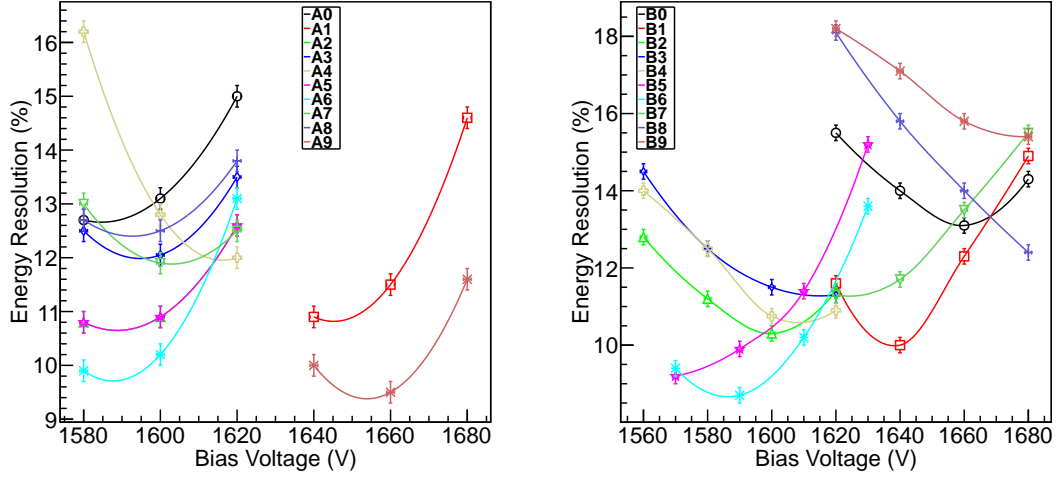
The dependence of the energy resolution for 8 keV X-rays on temperature was studied at low temperatures, in particular at -20°C and -30°C . The purpose was to check if there was a significant improvement of the energy resolution for the lowest

temperature or if -20°C is good enough to achieve the best performance. One of the modifications to the X-ray detection system for the muonic helium experiment is to replace the cooling system used in the muonic hydrogen experiment (homemade) by a commercial one. However, the energy resolution should not be compromised. The commercial cooling systems available have reliable operation at temperatures down to -20°C .

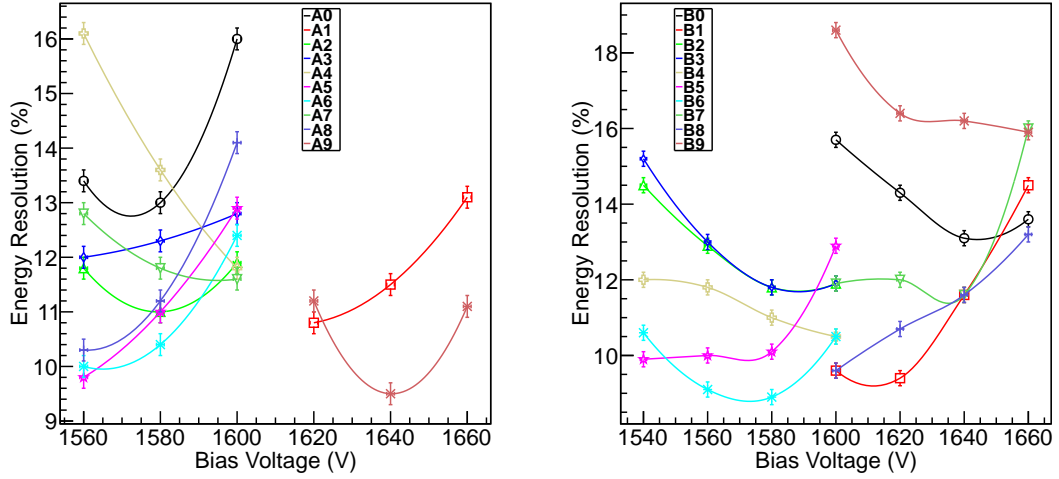
Figure 6.14 shows the energy resolution as a function of the bias voltage for the two temperatures investigated, -20°C and -30°C .

The dark current differences between -20°C and -30°C are typically 4 nA for the same bias voltage applied. For -20°C , as seen in figure 6.14 (a), APD A4 has a different behaviour in comparison with other detectors from the same array, as the energy resolution improves with increasing bias voltage. The APD has a lower signal amplitude and consequently a lower gain compared to other APDs with the same bias voltage applied. Please note that there are two different series of APDs manufactured at different times, which have different operational voltages, typically 60 V away to deliver the same gain. Regarding array B, two detectors, B8 and B4, show the worst performance. Both have shown asymmetries in the amplitude distributions. B8 also shows signals with lower amplitude, in comparison to the remaining APDs.

At -30°C , as seen in figure 6.14 (b), the behaviour is in general the same as for -20°C . There is no significant improvement of the energy resolution. For example, for B1, the best energy resolution achieved at -30°C was 9.4 % for a bias voltage of 1600 V, while at -20°C it was 10 % for 1640 V. The difference is not significant to justify the use of -30°C for cooling down the detectors instead of -20°C . To get the same gain at -20°C , 20 V more should be applied to the APD bias voltage compared to -30°C . The dark current increase is small.



(a) $T = -20^\circ \text{C}$



(b) $T = -30^\circ \text{C}$

Figure 6.14: Energy resolution as a function of the bias voltage applied for all detectors at (a) -20°C and (b) -30°C .

6.2 The Pre-Amplifier System

The pre-amplifier is the first electronic amplification stage after the detector's signal generation. It is placed adjacent to the detector's output to avoid an increase in the

noise level and signal loss. The pre-amplifier used since 2003 in the muonic hydrogen Lamb shift experiment was the RAL 108A pre-amplifier from Rutherford Appleton Laboratory [55]. However, a crosstalk between adjacent channels and ringing effects were observed during the experiment and confirmed in data analysis [32]. With the aim of preventing such outcomes and to provide faster signals, the development of new pre-amplifier for the muonic helium experiment was initiated.

There is a high background coming from the experiment environment, such as α particles, laser light and even plasma discharges in the avalanche gain, among others. This may create some problems to the experiment, such as pre-amplifier saturation, long pre-amplifier dead times, large dark current fluctuations in the APDs, oscillations in the neighbouring LAAPDs and pre-amplifiers [32], which may compromise the outcome of the experiment.

The pre-amplifier system used during the μ H experiment campaigns, made of 20 RAL 108A low-noise charge-sensitive preamplifiers (see figure 6.15), was specifically designed as one of the components of a modular amplifier system for the readout of silicon strip detectors. Each pre-amplifier channel is a low noise charge sensitive device, amplifying negative input signals and giving positive signals at the output. Since α particles have considerably larger amplitudes than X-rays, two high-conductance ultra fast Zener diodes with fast recovering time ($5\mu\text{s}$) were set at the pre-amplifier's input. At the output, the pre-amplifier has a resistor of 100Ω and not 50Ω because of the twisted pair cable used in the RAL 108A pre-amplifier. This reduces the output signal seen by the amplifier from $1/2$ to $1/3$, due to the voltage divider $R_{\text{out}}/R_{\text{cable}}=100/50$ [100].

A typical signal at the output of RAL pre-amplifiers has a rise time between 100 and 300 ns, fall times longer than 100 μs and amplitudes between 100 and 200 mV.

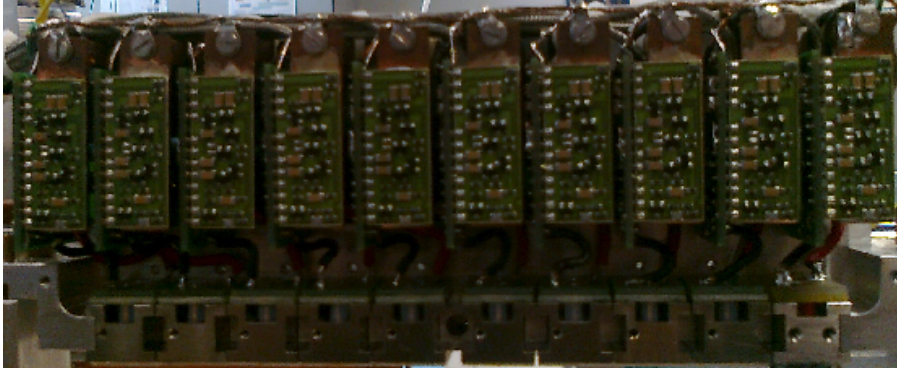


Figure 6.15: Array of 10 large area avalanche photodiodes (bottom) and 10 RAL 108A low-noise charge-sensitive pre-amplifiers (top).

6.2.1 The New Pre-Amplifier Concept

The main requirements for the new charge sensitive pre-amplifier prototype for the muonic helium experiment are:

- fast rise time in order to be more sensitive to the duration of the pulses formed in the detector;
- low noise level, so that the signal-to-noise ratio is not compromised;
- low power consumption, to reduce the heat load;
- small size, as space is limited around the target in the experiment.

Regarding the input characteristics, the match between the pre-amplifier capacitance and the LAAPD one (of about 120 pF) must be taken into account to convert a typical charge of $7 \times 10^{-14} \text{ C}$ (corresponding to 5×10^5 electron-hole pairs, for an usual LAAPD gain of 200 and for 8.2 keV X-rays). Zener diodes should be considered to protect the Field Effect Transistor (FET) against large signals in the input stage of the pre-amplifier. Other relevant parameter is the dynamic input capacitance, which must cover energies between 1.5 and 10 keV, corresponding to charges of 1.3 to $8.7 \times 10^{-14} \text{ C}$ for a typical LAAPD gain of 200.

Concerning the output characteristics, the pulse should have a rise time of about 10 – 50 ns and fall time of about 50 – 100 ns. The output polarity depends on the subsequent stage of amplification, which takes place in the post-amplifier. In the previous experiment, the post-amplifier accepted positive signals from the pre-amplifier and the signal was inverted at the output for further processing.

Another important parameter is the size and arrangement of the preamplifier's channels in the array. There are two face-to-face arrays of 10 LAAPDs, each with the respective pre-amplifier around the gas target, with a total dimension of $5 \times 12 \times 194 \text{ mm}^3$. The power consumption should be less than 0.5 W for each pre-amplifier to prevent as much heating as possible. The pre-amplifiers should have no performance degradation under intense magnetic fields and they should be able to work in vacuum. They should be operational under a temperature range between -40°C and 50°C . Filters for high voltage should be considered, as well as a good grounding scheme to avoid pick-up noise as much as possible.

6.2.2 Pre-Amplifier Prototypes

Figure 6.16 shows the first pre-amplifier prototype installed in an aluminium box with two preamplifier channels in the same plate (P2), developed at the Swiss Federal Institute of Technology Zurich (ETH). One of the pre-amplifier channels was connected to one LAAPD, since both pre-amplifiers share the same power supply. For safety reasons, one pre-amplifier was disconnected. The pre-amplifier's output signal characteristics, specified by the manufacturer for a regular signal generator, are for a pre-amplifier power supply of 5 V (presenting a 18 mA current, and therefore consuming about 0.1 W), positive polarity with amplitudes in the order of 30 mV, 5 ns rise time and 30 ns fall time, using a RC filter with 100 ns integration constant and with no differentiation.

A second prototype (see figure 6.17) with 5 pre-amplifier boards (each one with 2 channels), was built with the geometry suitable for the target used in the muonic

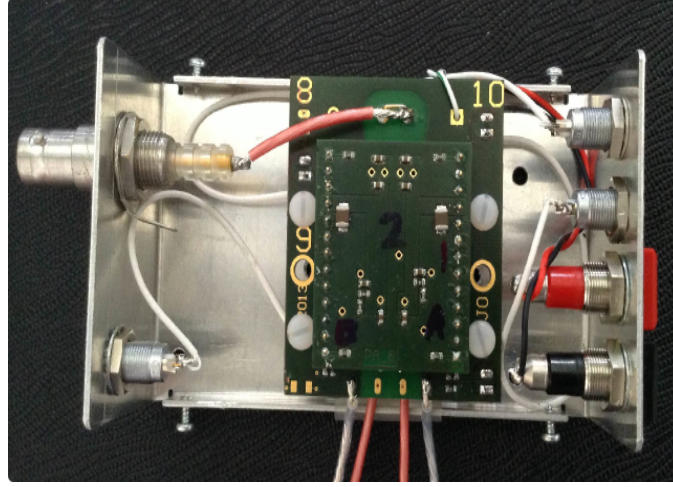


Figure 6.16: First pre-amplifier prototype made of 2 channels mounted sideways in the same plate (P2). The connections for high voltage, ground, pre-amplifier power supply and signal are placed in the bottom board. The integration and differentiation components are in the top plate.

helium experiment. The prototype was tested, evaluated and improved, giving origin to the last prototype seen in figure 6.18. As already mentioned, crosstalk between adjacent pre-amplifiers and ringing effects ought to be avoided. Five capacitors were used (470 pF, 220 pF, 1 nF, 1.5 nF and 2.2 nF), all of them connected to a resistor of $100\ \Omega$ for differentiation (the corresponding differentiation times are 47 ns, 22 ns, 100 ns, 150 ns and 220 ns, respectively). Each pre-amplifier board (P10, P11, P12, P13 and P14 respectively) has a specific differentiation constant. Only one channel in each board was connected to an APD for test (figure 6.17).

In order to test the two pre-amplifier prototypes, the detector pre-amplifier system was connected to electronic modules to mimic the electronics used in the Lamb shift experiment, as seen in figure 6.19. The signals were evaluated at the output of each electronic component of the data acquisition system. Radioactive ^{65}Zn or ^{55}Fe sources, the latter emitting 5.9 keV X-rays, were installed inside the chamber in such a way that the full active area of each detector was irradiated.

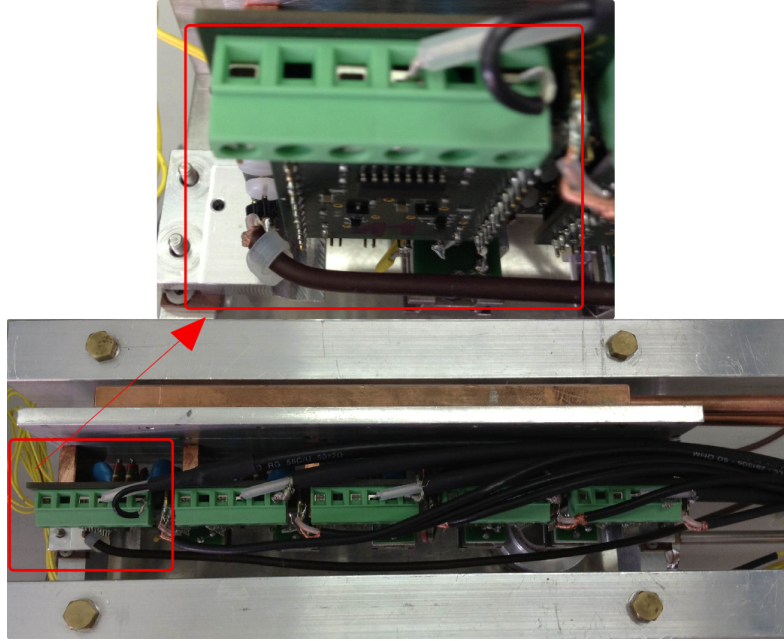


Figure 6.17: Second pre-amplifier prototype made of 5 pre-amplifier boards with different differentiation constants. In the top figure, one pre-amplifier channel is connected to one detector. The high voltage power supply, pre-amplifier power supply and ground cables are visible. In the bottom figure, 5 channels connected to APDs and respective cables, are shown. The copper piece is the alcohol cooler attached to the pre-amplifier housing for low temperature operation.

After the first amplification stage in the pre-amplifier, the signal is carried to a post-amplifier for signal shaping and amplification. The amplified signal is sent to a signal distributor Fan-out and split in two different paths. One is for the Waveform Digitizer (WFD), where all the important signal information, such as the amplitude and the timing parameters, is saved in a “raw file”. The second path is for further shaping and discrimination. This part will be responsible for deciding if the signal will be recorded in the WFD or discarded. If the event is understood as an 8 keV X-ray, a trigger signal will be sent and an Event Gate (EVG) will open for a fixed period of time. All relevant information will be recorded and at the end of that period of time, End of Event Gate (EEVG), the WFD will stop recording the signal and the

6.2. The Pre-Amplifier System

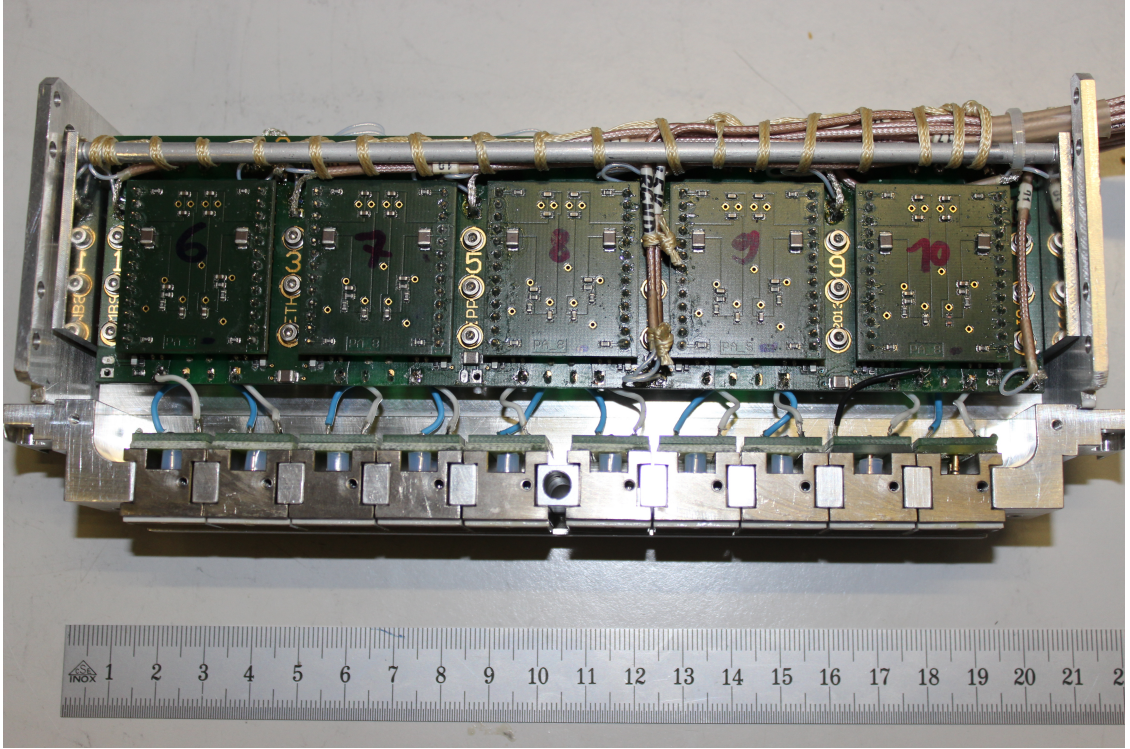


Figure 6.18: Final version of the pre-amplifier array to be used in muonic helium experiment, connected to the respective detectors. There are 5 boards (P6, P7, P8, P9 and P10), each one with 2 distinct pre-amplifier channels.

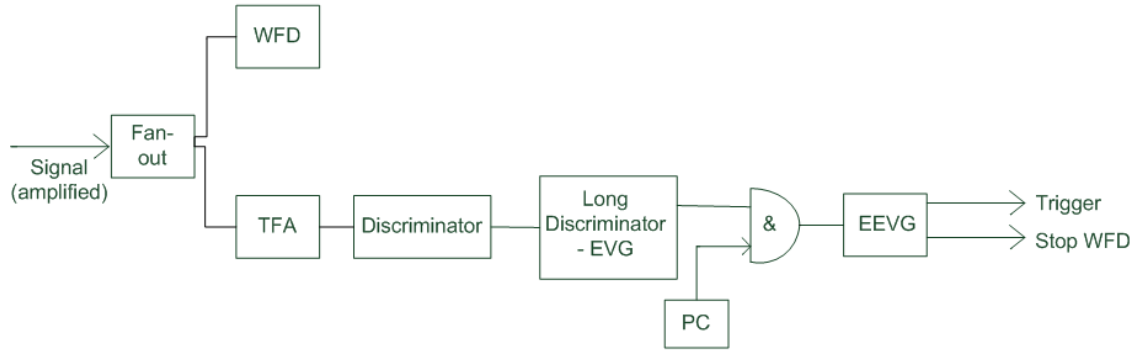


Figure 6.19: Schematic diagram of the data acquisition system used to analyse the pulses coming from the detector and further amplification stages, pre-amplifier and post-amplifier, during the pre-amplifier tests.

system will be ready to receive more data. During these tests the EVG was manually controlled.

Five new LAAPDs were selected for this pre-amplifier study, labelled as T60, T61, T62, T63 and T64. The parameters considered to select the best APDs are the energy resolution for 8 keV X-rays, pulse shape and rise time. The RAL pre-amplifier was used for the selection and general characterization of the APDs.

Table 6.7: *Summary of the operational LAAPD parameters for the pre-amplifier study. These values were obtained with the RAL pre-amplifier at -30°C .*

LAAPD label	Bias voltage (V)	8 keV resolution (%)	Rise time (ns)
T78	1600	13	120
T60	1600	15	120
T61	1600	12	100
T62	1600	14.5	120
T63	1600	16	80
T64	1600	13	100

A new post-amplifier module with gain of 4 and 10 inputs/outputs was also manufactured. The post-amplifiers (PA) were labelled PA1,...,PA10. Most of them have an integration time of 10 ns (capacitor with 100 pF and a resistor of 100 Ω), except PA2, PA3 and PA4 with 4.7 ns, 15 ns and 50 ns integration times, respectively.

6.2.3 Pre-Amplifier Tests and Results

The first prototype was tested so that some initial characteristics could be amended to fulfil the pulse shape requirements for the experiment. The changes were afterwards implemented in the second prototype. The signals at the output of all electronic devices were observed and analysed.

6.2. The Pre-Amplifier System

The detector pre-amplifier prototypes were installed inside the vacuum chamber and each APD active area was fully irradiated with the ^{65}Zn or ^{55}Fe radioactive sources positioned inside the chamber below the APD. For the first tests, the pre-amplifier bias voltage was 6 V.

With regard to the first prototype (figure 6.16), the LAAPD selected was T78 biased to 1600 V. At room temperature, the detector presented a dark current of about 350 nA. The noise level was very high, as seen in figure 6.20, probably due to the large dark current and also to pick up noise arising from surrounding machinery. Still, 8 keV X-rays were visible (pulses with amplitude around 200 mV), as well as electrons (with amplitudes higher than 800 mV).

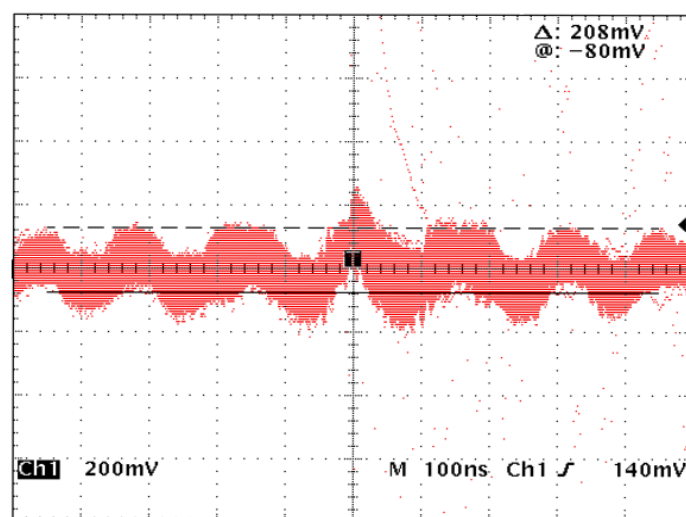


Figure 6.20: Pre-amplifier signals for the first prototype using the ^{65}Zn source at room temperature. Pulses from 8 keV X-rays and electrons are visible. Some pick up noise is also visible.

The pulses at the pre-amplifier output have amplitudes between 200 mV and 1 V, depending on the particle detected, and an intrinsic noise level of about 200 mV peak-to-peak. The rise time is 10 – 20 ns, one order of magnitude lower than the one

reported in table 6.2 for RAL pre-amplifiers. The pulses fall time is $75 - 100$ ns, much shorter than for RAL pre-amplifiers.

The pre-amplifier was tested at low temperature. At -30°C , the dark current decreased to values lower than 10 nA , and the noise level was significantly lower. In addition, no pick up noise was observed. In figure 6.21 (a) it is well visible the X-ray signals with lower amplitude, about 250 mV , and the electron signals, with higher amplitude. The X-ray signals present rise times of 20 ns and fall times of $100 - 200\text{ ns}$, consistent with the results obtained at room temperature. Figures 6.21 (b) and (c) show how the amplitude and risetime of the X-ray pulses are measured.

The next step was to test the pre-amplifier's array connected to the rest of the acquisition system, using the second prototype with 5 different pre-amplifier boards with different capacitors: $C=0$ (no differentiation), $C=220\text{ pF}$, $C=1\text{ nF}$, $C=1.5\text{ nF}$ and $C=2.2\text{ nF}$. One channel in each board was connected to one APD, as seen in table 6.8. The radiation source used for this study was ^{55}Fe emitting 5.9 keV X-rays.

Table 6.8: *LAAPDs and corresponding pre-amplifier boards, with different time constants (differentiation).*

LAAPD label	Pre-amplifier board	Time constant (ns)
T61	P2	0
T63	P11	22
T62	P12	100
T60	P13	150
T64	P14	220

The noise behaviour at the pre-amplifier output is of major importance. The pick up noise sources should be reduced as much as possible. The noise was checked at room temperature with and without bias voltage applied to the APDs. The pre-amplifier was biased with 6 V . When the LAAPDs were polarized, dark currents of

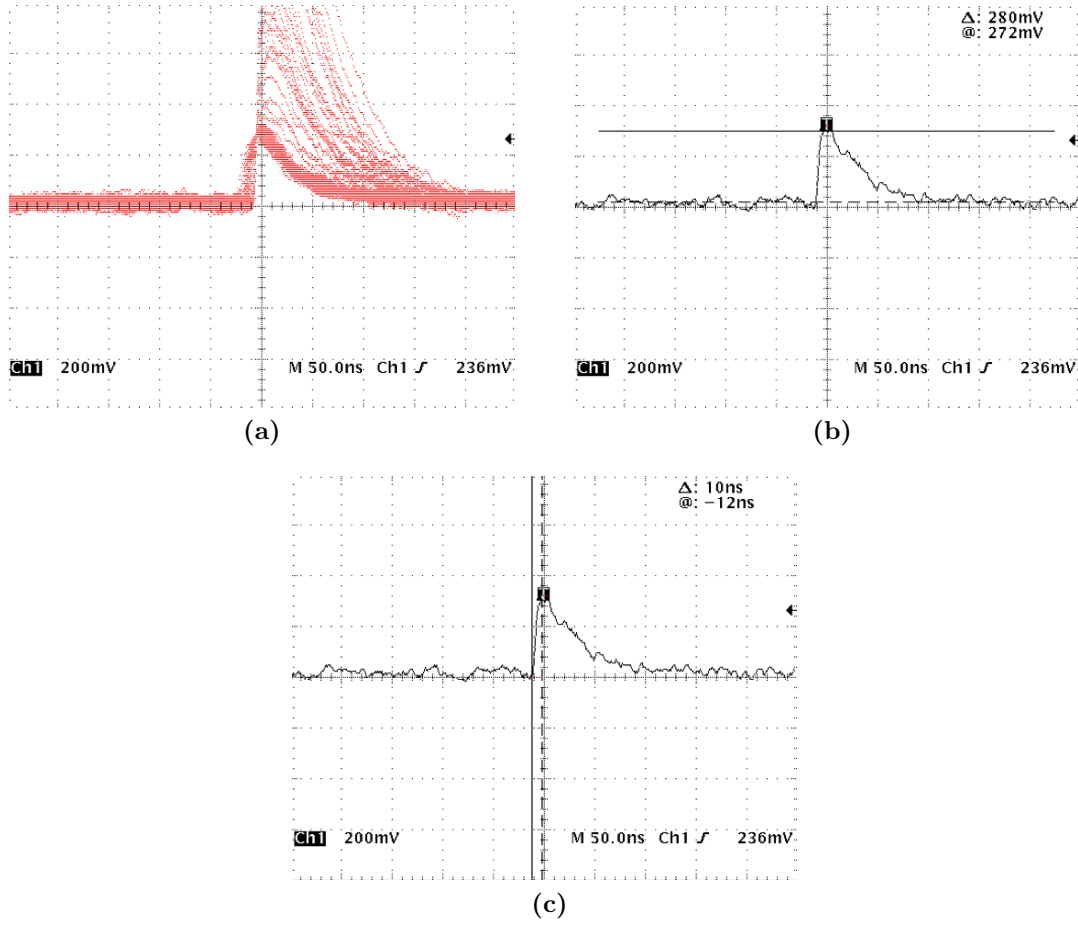


Figure 6.21: Pre-amplifier output pulses for the first prototype using the ^{65}Zn source at -30°C . (a) Signals from 8 keV X-rays and electrons in persistent mode. (b) Amplitude measurement of one X-ray signal. (d) Risetime measurement of one X-ray signal.

the order of 300 nA were measured. Figure 6.22 shows three different signals. The yellow trace (channel 1) is from APD T63 with the whole active area irradiated. The blue trace (channel 2) is from APD T62 with no source irradiating the active area. The green trace (channel 4) is from the pre-amplifier without any APD connected.

Figure 6.22 shows two different situations: without bias voltage in the APD (a) and with 1600 V applied to the APD (b). Channel 1 presented an increase of $1/3$

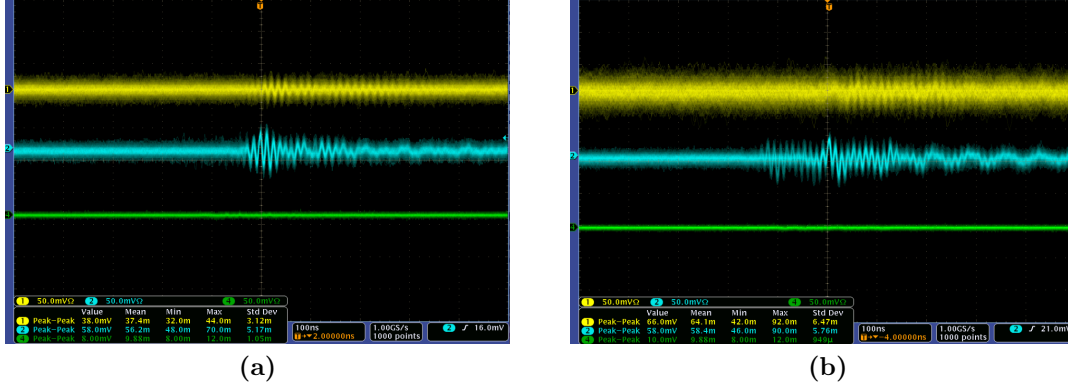


Figure 6.22: Noise at the pre-amplifier output for 3 channels in 3 different conditions, channel 1 with all the whole APD active area irradiated, channel 2 with no source irradiating the APD active area and channel 4 without any APD connected. (a) LAAPDs with no bias voltage applied. (b) LAAPDs biased with 1600 V. The time scale (X axis) is 100 ns per division and the amplitude scale (Y axis) is 50 mV per division.

in noise amplitude, from 40 mV to 66 mV, when the LAAPD was biased. Channel 2 maintained the noise level value of 58 mV. Channel 4 increased the noise level from 8 mV to 10 mV, which is not significant. The pick-up noise presented in channels 1 and 2 may have origin in the turbo pump or grounding connections, as already pointed out.

The 5 different configurations of the pre-amplifier were analysed in order to decide which one was the best for the experiment. Signal shape, rise time and fall time, as well as signal to noise ratio (SNR) and energy resolution, were evaluated and compared for all pre-amplifiers.

Results are presented in table 6.9, where a deterioration of the energy resolution and SNR are observed with increasing differentiation constants (see table 6.8). Comparing the extreme differentiation constants for boards P2 and P14, the first one shows a better performance. The energy resolution is 15.2% against 22.4%, and the SNR is 6.5 against 2.8, even if the rise time and the noise level were lower for

6.2. The Pre-Amplifier System

Table 6.9: Pre-amplifiers output signal characteristic with differentiation constants at -20°C . All LAAPDs were polarized with 1620 V. All pre-amplifiers were biased with 4.5 V.

Pre-amplifier board	SNR	Energy Res. (%)	Rise Time (ns)	Noise (mV)
P2	6.5	15.2	10	25
P11	4.8	16.7	10	20
P12	4.6	22.3	10	30
P13	4.2	20.4	10	20
P14	2.8	22.4	6	17

P14. Another relevant parameter was the signal shape, in particular the presence of an undershoot in the signal fall. The undershoot can stay for long periods of time, and if some pulse arrives during this time, it will be superimposed to the undershoot, thus introducing an error in the amplitude measurement. All the pre-amplifiers have shown a significant undershoot excluding P2.

The pre-amplifier selected for the experiment was P2, with no differentiation and with 100 ns integration time. From this moment on, the tests were carried out with this pre-amplifier configuration.

The bias voltage of the pre-amplifier to be used was studied in view of providing the best SNR. A range from 2.5 V to 7 V was swept and the relevant information was analysed. Figure 6.23 shows the pre-amplifier signals from 5.9 keV X-rays for 3 different pre-amplifier's bias voltages applied. It is visible that higher voltages lead to a considerable increase in the noise level, in particular for 6 V when compared to 4 V.

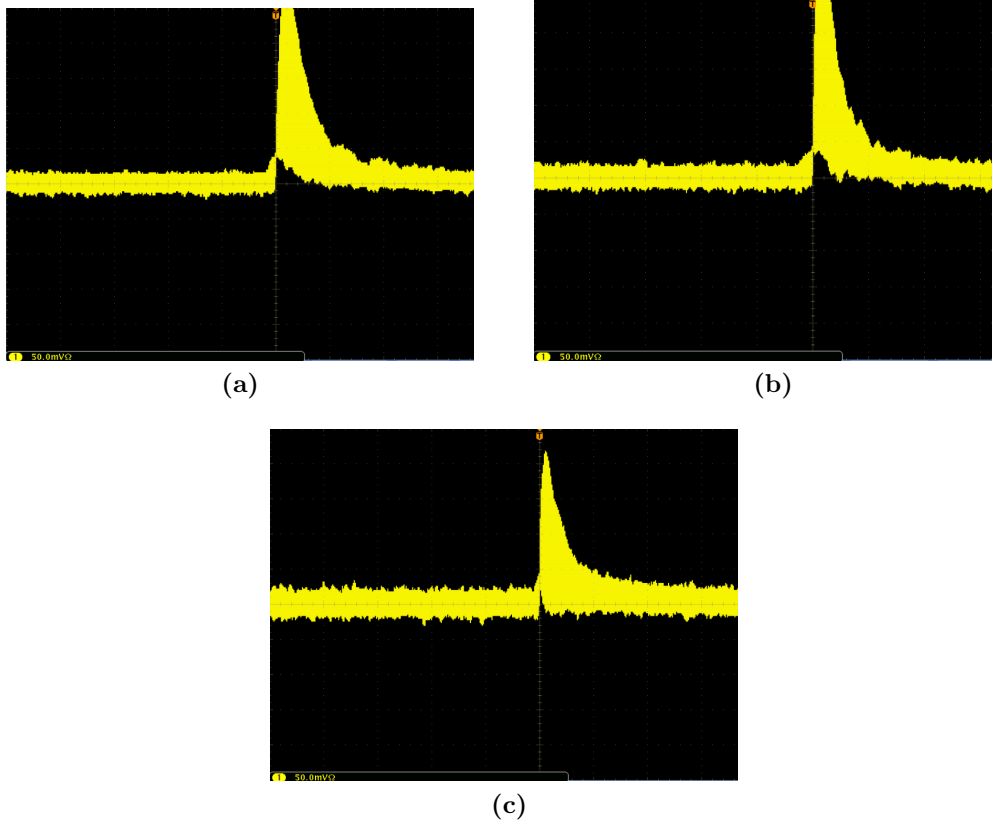


Figure 6.23: Output signals obtained using envelope mode in the oscilloscope for different pre-amplifier's bias voltages: (a) 4 V; (b) 5 V; (c) 6 V. The vertical scale is 50 mV and the horizontal one is 100 ns per division.

Figure 6.24 shows the influence of the bias voltage on the energy resolution and SNR values, and consequently in the system overall performance. For 3 V, the energy resolution has the lowest value of 14.1% and the SNR is one of the highest (7.4). For a bias voltage of 7 V, the energy resolution is 16.2% and the SNR is 5.4. For 6 V, the bias voltage value recommended by the manufacturer, the energy resolution and the SNR values are 15.8% and 5.7, respectively. The best energy resolution is obtained for lower bias voltage, in the range 2.5 – 4 V, where the SNR is maximal.

Despite the higher amplitude achieved for higher pre-amplifier's bias voltages, which means a higher pre-amplifier gain, the high bias voltage values deteriorate the

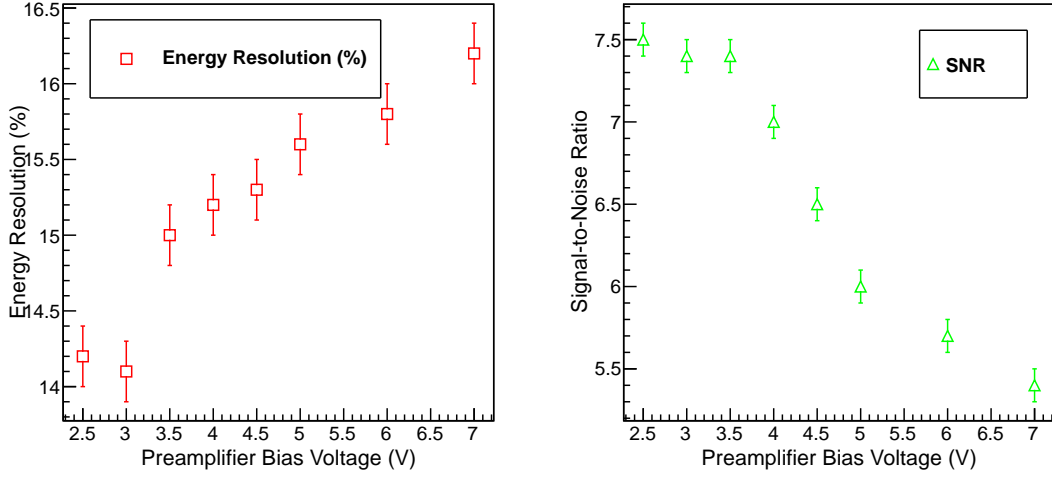


Figure 6.24: Energy resolution (left) and SNR (right) as a function of the pre-amplifier bias voltage at -30°C .

SNR and the energy resolution, thus compromising the performance of the system. The voltage selected to polarize the pre-amplifier, taking into account the results obtained, was 3 V, having another advantage, the low power dissipation in vacuum when comparing with the high voltage values.

The post-amplifier, the electronic component following the pre-amplifier in signal processing, was also studied. It is responsible for signal shaping, and amplification, together with some noise filtering. As mentioned before, a new post-amplifier module with 10 inputs/outputs and a gain of 4 was ready for testing. The LAAPD and pre-amplifier used were T61 and P2, and the source used was ^{55}Fe . Pulses from post-amplifier channels with different integration constants were compared. Results are shown in figure 6.25, which displays a risetime increase with increasing integration constants. As seen in figure 6.25, for a 4.7 ns integration constant, the rise time obtained was 9.5 ns, for 10 ns it was 10.5 ns, for 15 ns it was 13.5 ns and for 50 ns it was 23.5 ns. The lowest integration constant is not adequate due to the small rise time presented at the post-amplifier output, which compromises the signal of the detector.

10 ns integration constant, delivering signals with rise times of about 10-12 ns. Two arrays, each one with 10 detectors and 10 pre-amplifiers, were used in the muonic helium Lamb shift experiment, as well as two modules of 10 post-amplifier channels.

6.3 Discussion

Large area avalanche photodiodes from RMD were investigated as low-energy X-ray detectors in order to evaluate their suitability for the muonic helium Lamb shift experiment. It is well-known that their detection efficiency drops by a factor of 2 from 2 keV to 8 keV X-rays. Even so, the values were not as low as initially expected. Since the angular distribution of 8 keV X-rays from μHe leads to an increase of the absorption layer thickness by a factor $\bar{A} = 1.6$, absolute efficiencies between 53 and 65 % are achieved. Concerning the energy resolution for 8 keV X-rays, at -30°C , values below 20 % were attained and one prototype has shown an even much lower result, of about 9 %. The study of the energy resolution dependence on temperature has shown that, between -30°C and -20°C , the dark current difference is not so significant for the degradation of the energy resolution. This enables the use of commercial cooling systems operating at -20°C , which is easier and more reliable to manipulate than the old one. New pre-amplifier arrays and post-amplifier modules, were developed in view of avoiding crosstalk between adjacent detectors and ringing effects, and to make signals faster than the ones from the muonic hydrogen Lamb shift experiment. Several prototypes, with different integration and differentiation constants fulfilling the main requirements for the muonic helium experiment, were developed and tested. The best pre-amplifier post-amplifier configuration was chosen. The pre-amplifier with no differentiation and with 100 ns integration time was selected due to the good energy resolution (about 16 % for a typical APD) and high SNR (about 6.5), as well as to the absence of undershoot. The pre-amplifier's bias voltage was set to 3 V, which gives the best performance. The best post-amplifier was the one

with 10 ns integration constant, allowing rise times of 10 – 12 ns, which was similar to the ones in the pre-amplifier stage.

Chapter 7

Preliminary Results of the Muonic Helium Experiment

The muonic helium Lamb shift experiment aims to achieve the measurement of the two transitions in $\mu^4\text{He}^+$ ions, $2S_{1/2} - 2P_{3/2}$ and $2S_{1/2} - 2P_{1/2}$, with 813 nm and 899 nm respectively. The first transition was measured in the second half of 2013 and the second one in 2014. Afterwards, the experiment was extended to the $\mu^3\text{He}^+$ ion to measure the several transitions $2S_{1/2} - 2P_{3/2}$ and $2S_{1/2} - 2P_{1/2}$, outside the scope of this thesis. The preliminary results of this experiment are described in this chapter, in particular the first transition measured and the X-ray performance during beam time.

In brief summary, a muon entering in the apparatus is recorded by muon detectors, before stopping in the gas target. It will trigger the data acquisition system, opening the Event Gate (EVG), as well as the laser system. The X-rays detectors (LAAPD) and electron detectors are ready to record this specific event. After the event gate time, all information is recorded by WFDs and TDCs and stored as “raw data” by the MIDAS for posterior offline analysis in the backend computer.

The LAAPD’s current signal is converted in a negative voltage signal by the pre-amplifier, which is carried to be digitized by the WFDs. The amplitude of the pulse

is proportional to the energy deposited by the radiation in the detector. The data is monitored in real time (online analysis). Energy and time histograms of the pulses detected are stored and checked. During this time, no detailed analysis is carried out. More specifically, no time and energy calibrations for all detectors take place, and no energy and muon cuts are applied for event class discriminations. In the end, there will be a detailed analysis, which will provide a valuable contribution to measure the resonance curve, by significantly reducing the background superimposed to the resonance peak, thus improving the SNR and overall statistics. For more details concerning the offline data analysis procedure and methods that were carried out, see [32].

Figure 7.1 shows one long run, of about 2 hours of data taking, per LAAPD from Arrays A and B during the $\mu^4\text{He}^+$ experiment run. As seen, APD B8 presents a very low rate of events, due to a problem during the experiment and was not replaced. In general, all other LAAPDs presented a number of pulses in the same order of magnitude. However, the LAAPDs placed in the centre from both arrays (3, 4, 5 and 6 positions), present a slightly higher number of pulses (i.e more muons stop in front of those detectors) than in the average for both arrays. Also for array A there are about 10 % more events than for array B. This could be due either to an average difference in the APD efficiency or to a small difference, of about 0.5 mm, in the muon beam axis between array A and between array B in the axis of the target vessel.

Particles are distinguishable by their amplitude, which is proportional to the energy deposited in the detector material, and by the time they are detected. These LAAPDs detect not only X-rays but also particles with energies between a few hundred eV to a few MeV. Figure 7.2 shows the 2D energy versus time histogram for LAAPDs A8 and B8. There is a large concentration of pulses around 8 keV and 1.5 keV, at times between 0.15 and 0.4 μs . Those two well-distinguished X-ray concentrations are from 8.2 keV K_{α} and 1.5 keV L_{α} X-rays. For energies higher than 8 keV, a significant number of pulses are noticeable in the full time range. These

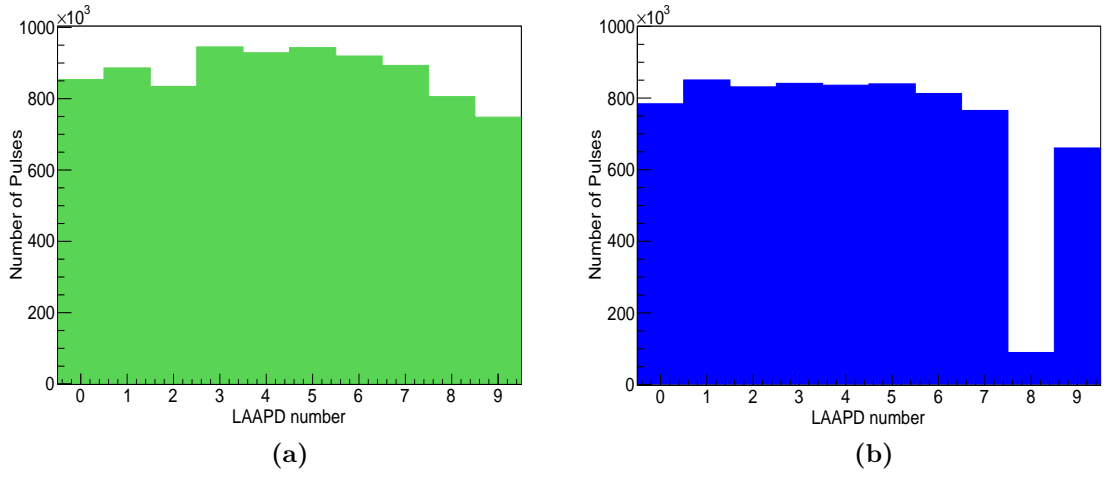


Figure 7.1: Number of detected pulses per LAAPD. Figures (a) and (b) are for array A and array B, respectively.

events are electron hits. In figure (b) there is a concentration of events with exactly the same energy and time ranges as in (a).

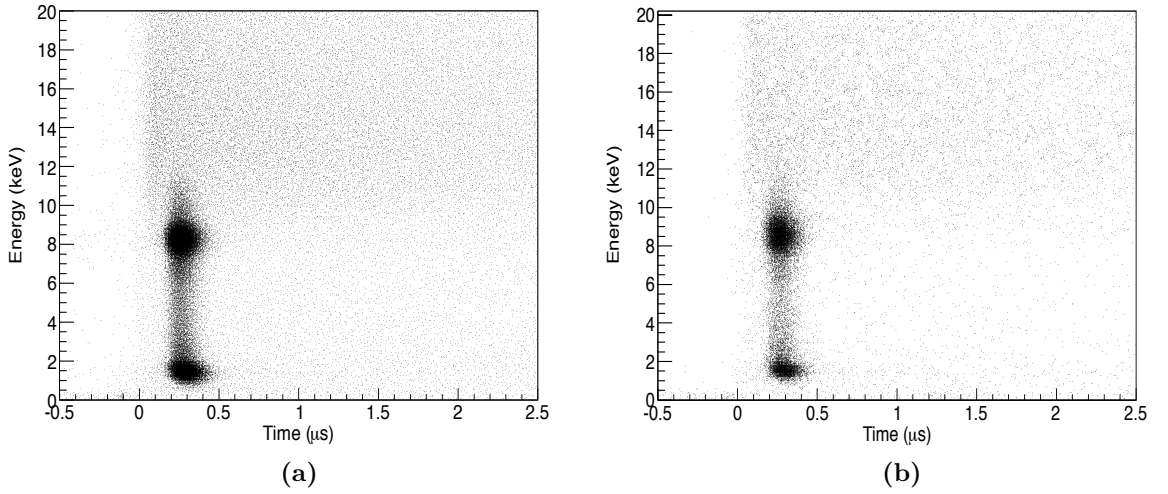


Figure 7.2: 2D plot of energy versus time for all particles detected in the LAAPDs A8 (a) and B8 (b).

Figure 7.3 shows pulses for LAAPD A6 directly from the WFD. Two distinct signals are visible, at approximately 970 time bins ($3.8\mu s$), with an amplitude of about 400 channels (which corresponds to 100 mV), and at 1380 time bins ($5.5\mu s$), with higher amplitude, about 1450 channels (350 mV). The first signal corresponds to an X-ray event, while the second one is from an electron probably originated from muon decay.

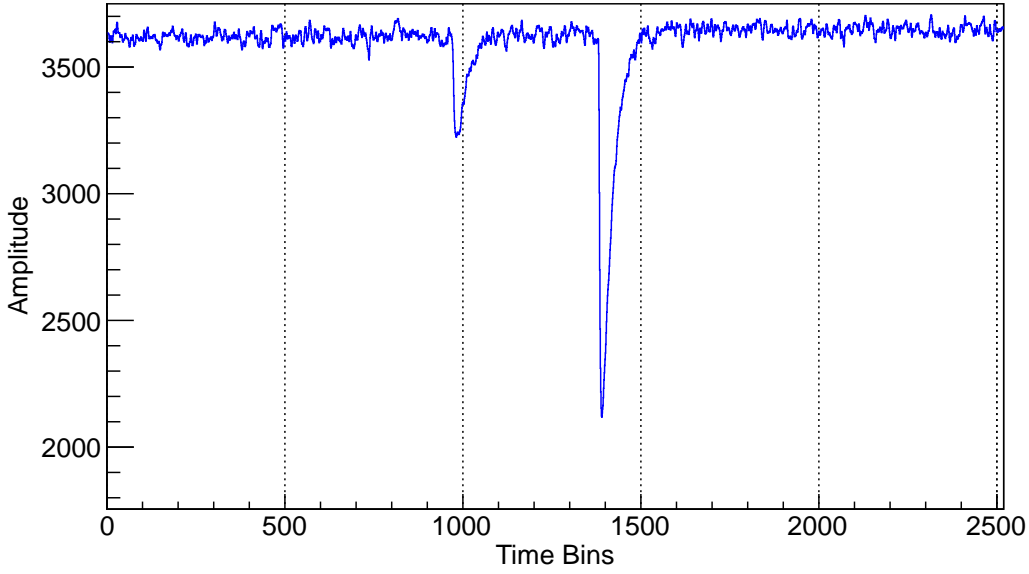


Figure 7.3: LAAPD A6 pulses in the muonic helium experiment. At about 970 time bins it is visible one pulse from an X-ray and at 1380 time bins a second one from an electron hit. In the XX axis, 1 time bin is 4 ns and in the YY axis 4096 channels correspond to 1 V.

The energy distribution of pulses detected in all LAAPDs (except B8) is shown in Figure 7.4. The 8.2 keV X-ray K_{alpha} peak and the 1.5 keV X-ray L_{alpha} are well defined in the distribution. For energies above 10 keV it is well noticeable the electron contribution originated from muon decay. The energy resolution obtained for 8.2 keV X-rays, taking into account the region 7.2–9.2 keV, is 18.2%. This value demonstrates the overall good performance of the LAAPDs, in agreement with studies performed

before with APDs used in the former muonic hydrogen experiment, as presented in chapter 6.

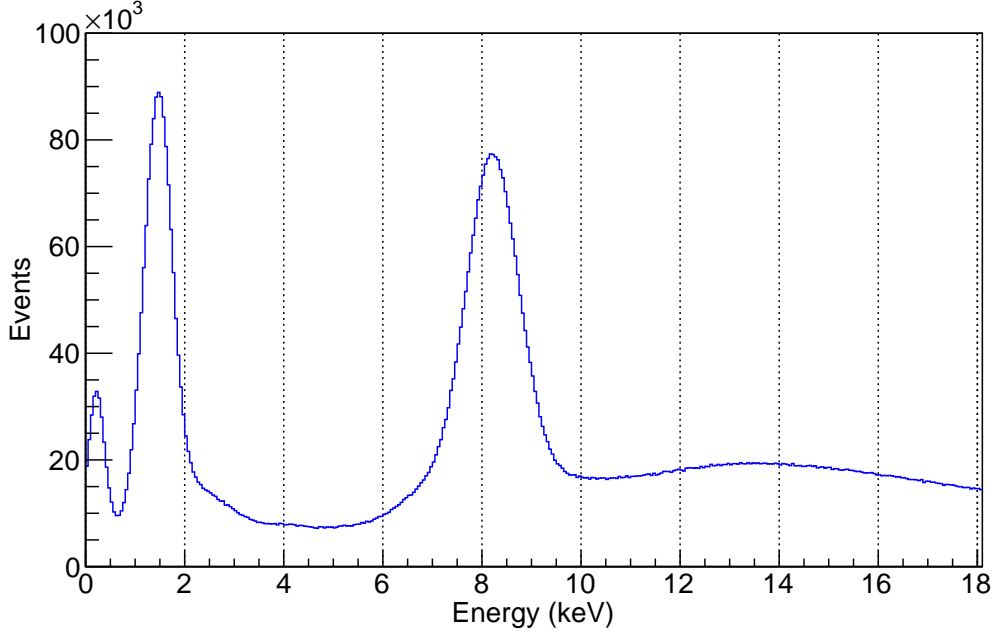


Figure 7.4: Energy distribution of the pulses obtained in all LAAPDs (except B8) during beam time of the muonic helium Lamb shift experiment. The 8.2 keV and 1.5 keV X-ray peaks are well visible.

The time spectrum of all events in the APDs (with no applied cuts) is shown in figure 7.5. The peak between 0.1 and 0.6 μ s is from "prompt" events originated from the muon cascade. When muons are stopped in the helium gas target, muonic atoms in excited states are formed, decaying promptly to the ground state, emitting 8.2 keV X-rays. The electrons from the subsequent muon decay give rise to APD signals with relative large amplitudes at delayed times. The typical exponential behaviour from muon decay is noticeable in the spectrum.

Figure 7.6 shows different time spectra in two different situations: laser off resonance (top figures) and laser on resonance (bottom figures). To reach this level of discrimination, energy and time calibrations were introduced, and energy and time

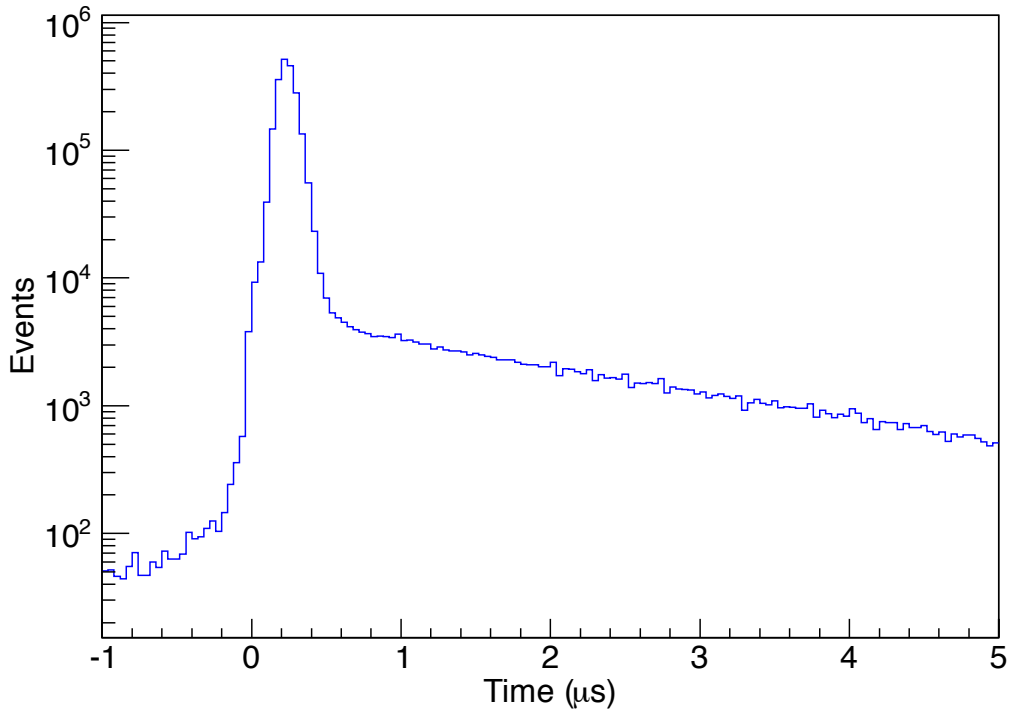


Figure 7.5: Time spectra of all hits in the LAAPDs. The peak corresponds to prompt events.

cuts were applied. The events plotted here are from detected X-rays which belong to Class 110 ("golden events"), with the exception of the second muon cut, which was not introduced for analytical purposes at that moment. For information concerning the event structure, see appendix A.

The first remarkable difference between figure 7.5 and figure 7.6 is the background level. In the first one, for times around $5 \mu s$, the background level is about 10^3 events, whereas in the second one it is about 50 events only, i.e 200 times less.

On resonance, there were about 13 laser-induced events per hour, considerably less than initially estimated (48 events per hour on resonance) [22]. The main reason for this reduced event rate is because the laser had to be operated at lower intensities

than foreseen, in order to avoid optical surface damage of mirror components in the gas target.

Looking at figure 7.6, top and bottom distributions, the peak with the laser ON resonance is clearly perceptible, opposite to the laser OFF resonance case. The large peak at early times, visible in both figures, is the "prompt peak" already visible in figure 7.5. However, about $1\ \mu s$ after, a smaller peak is visible, which is the "resonance peak". The number of measured events on resonance was about 300 in total, although the background still needs more discrimination, since the SNR is about 1 and should be improved by a refined analysis.

A very preliminary result from the laser spectroscopy in muonic helium is shown in figure 7.7. The resonance obtained for the first transition measured, corresponds to the energy difference between the $2S_{1/2}$ and $2P_{3/2}$ states in $\mu^4\text{He}^+$ ions. The resonance curve was obtained by plotting the number of 8.2 keV X-rays recorded within the laser time window, normalized to the total number of prompt events, as a function of the laser detuning from the fitted centre position (frequency). At this time, the real scale of the frequency is not revealed. A detailed analysis is needed in order to obtain the accurate values and the results will be published only afterwards.

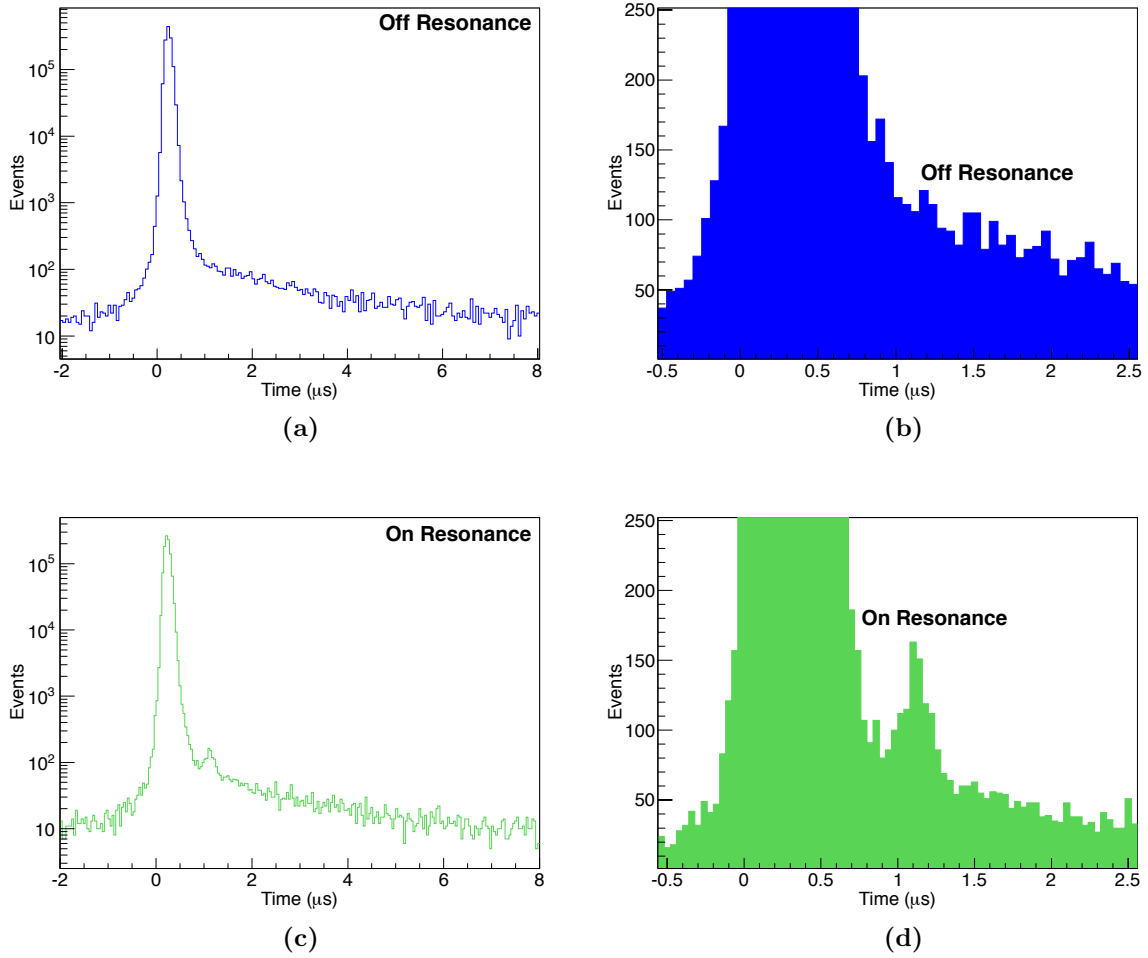


Figure 7.6: Time spectra of all X-ray events from Class 110 detected in two different situations: Laser Off resonance (a,b) and Laser On resonance (c,d).

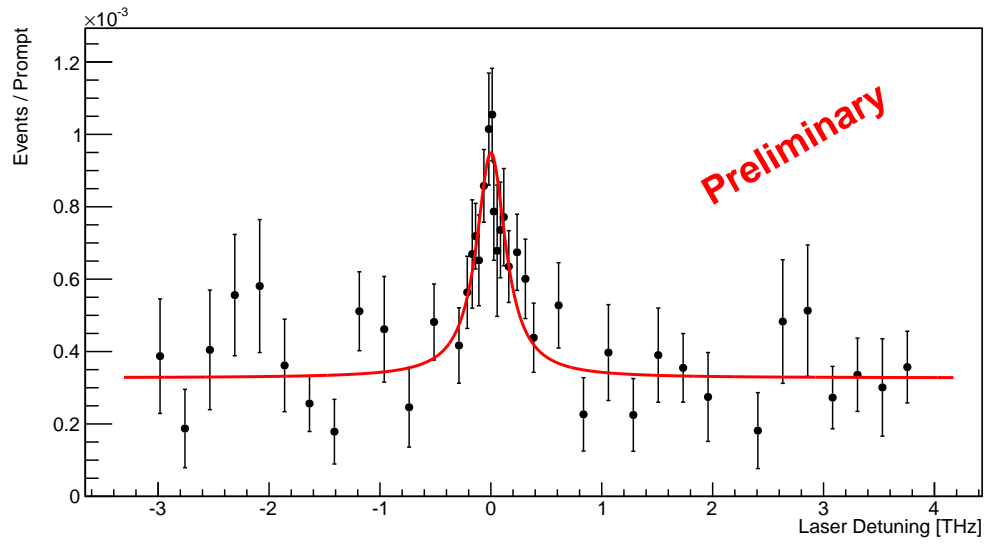


Figure 7.7: Very preliminary resonance curve corresponding to the first transition measured in $\mu^4\text{He}^+$ ions in the 2013-2014 campaign of the experiment, showing the number of delayed 8.2 keV X-rays, normalized to the total number of prompt X-rays, recorded within the laser time window, as a function of the laser detuning.

Chapter 8

Conclusions

This thesis presents the R & D studies carried out for the X-ray detection system to be implemented in the muonic helium Lamb shift experiment. It also offers some preliminary results for the $\mu^4\text{He}^+$ transition, $2S_{1/2} - 2P_{3/2}$, with a particular focus on the detectors' performance during beam time.

Two different semiconductor detectors, large area avalanche photodiodes (LAAPD) and the reach-through avalanche photodiodes (RT-APD), were investigated for the detection of 8 keV X-rays. The main difference between these two types of APDs is the thickness of the depletion region, with the RT-APD presenting the thicker one. The operational parameters of both types of detectors were investigated at room temperature and lower temperatures (0°C , -20°C and -30°C).

The RT-APD has shown the best energy resolution of 9.5% at 0°C and a minimum detectable energy of 0.25 keV. Nonetheless, for the gain region of interest (corresponding to optimal energy resolution), the minimum detectable energy was 0.9 keV. The gain variation with temperature was found to increase with bias voltage, increasing from -1.0% per $^\circ\text{C}$ to -1.7% per $^\circ\text{C}$ for 200 V and 400 V, respectively. The gain non-linearity between X-rays and visible light pulses was also investigated, showing an increase with decreasing temperature. Indeed, for a gain of 200 V at -20°C , a gain non-linearity of 42% was obtained, against 30% at 20°C . As a result, the

RT-APD prototypes investigated have displayed worse performance than the planar APDs used before in the muonic hydrogen experiment. In addition, larger prototypes would be needed to cover the solid angle around the helium target in the experiment. For those reasons, it was decided to test the LAAPD already used in the previous experiment for the detection of 8 keV X-rays.

The LAAPDs used in the muonic hydrogen Lamb shift experiment proved to be a good option for the muonic helium Lamb shift experiment, despite the lower detection efficiency for 8 keV in comparison to 2 keV. This limitation could be overcome by increasing the population of the $2S$ state. The use of -20°C instead of -30°C was also confirmed, with almost no performance degradation, thus enabling the use of a commercial cooling system, more reliable than the home-made system that was used before.

New pre-amplifier and post-amplifier arrays were developed. The pre-amplifiers are faster than the previous ones from RAL, preserving important signal characteristics and parameters such as signal shape, energy resolution and SNR. In what concerns the post-amplifier, the new ones allow pulse risetimes of 10 – 12 ns, matching the pre-amplifier parameters, thus preserving the signal information.

The $2S - 2P$ resonance curve was obtained in $\mu^4\text{He}^+$ ions. The energy resolution attained for LAAPDs during beam time for 8.2 keV X-rays was about 18%, confirming their good performance, and therefore endorsing the work carried out during this PhD research.

The next step in this Collaboration is to analyse the muonic helium data and compare it with the muonic hydrogen results to see if they are consonant. It is expected that this will help to solve the proton radius puzzle, which has been widely discussed for the past 4 years, as well as to understand the several contributions to the Lamb shift in full detail. In addition, the helium RMS charge radius, as well as the fine structure and the magnetic moment distribution, will be revealed.

It is already under discussion what will be the next step for the CREMA Collaboration after the muonic helium Lamb shift experiment. One possibility is

to repeat the muonic hydrogen experiment to consolidate the results obtained in the previous experiment. Nonetheless, the most probable activity is to assess a new element, for example μLi^+ , and prepare a new experiment. Energies at 18 keV and 20 keV need to be detected and the LAAPDs present a low efficiency for those energies. One possibility could be the use of the RT-APDs or even the use of CZT detectors which present advantages such as high sensitivity for X-ray and gamma-rays, operation in direct conversion mode at room temperature and they can be manufactured into different shapes.

Appendix A

Event Structure

The event structure for further analysis is a complex and detailed process which is beyond the scope of this work, as explained and described in [32]. Nevertheless, it is fundamental to provide here some background regarding this issue, in order to better understand the preliminary results already presented in chapter 7. As mentioned in the beginning of that chapter, when the acquisition system is with the EVG open, all LAAPDs and electron detectors collect signals from particles that are hitting them. As mentioned before, only a few good events per hour on resonance are expected in the total amount of events. Therefore, efficient techniques need to be implemented in order to discriminate useful and non-useful events at this stage. It is now helpful to differentiate hits from events.

Hits are thereby further interpreted by the "Analyzer" program which will cross all the data in the "raw data" files (recorded and stored in the WFD) with a "parameter file". The latter will contain all the detailed information concerning the energy of the particles of interest (interpreted as an "energy cut") and their times of arrival at the detectors ("time cut"). This intertwined information will give rise to the construction of the event. Those events, depending on the parameters which define the calibrations and cuts, will then be structured and grouped into different classes. The event classes are discriminated according to the number and order in time of the

X-rays and electrons from muon decay. The class of events which defines the transition $2S_{1/2} - 2P_{3/2}$ in $\mu^4\text{He}^+$ is called Class 110, where one X-ray with 8.2 keV energy is detected, and consequently an electron from muon decay in laser coincidence. Many more classes are possible, for example the Class 113, where an electron is detected before the 8.2 keV X-ray or, for instance, the Class 120 characterized by the detection of an 8.2 keV X-ray with further electron detection. However, in this case, 2 electrons are detected. Table A.1 summarizes the most relevant event classes. For further details, see [32].

Table A.1: *Event Classes and description. The event classes are distinguished according to the number and order in time of the X-ray and electron detected [32].*

Event Class	Description
01	e^-
02	$2e^-$
10	X
11(#)	$X+e^-$
110	$X+e_{\text{delayed}}^-$
111	$X+e_{\text{early}}^-$
112	$X+e_{\text{late}}^-$
12(#)	$X+2e^-$
120	$X+e_{\text{delayed}}^-+e^-$
121	$X+e_{\text{early}}^-+e^-$
122	$X+e_{\text{late}}^-+e^-$
123	e^-+X+e^-
20	2X

Bibliography

- [1] W. E. Lamb and R. C. Retherford, “Fine structure of the hydrogen atom by a microwave method,” *Phys. Rev.*, vol. 72, Aug 1947. 1, 9
- [2] E. Borie and G. A. Rinker, “The Energy-Levels of Muonic Atoms,” *Reviews of Modern Physics*, vol. 54, no. 1, pp. 67–118, 1982. 1
- [3] E. Borie, “Lamb shift in light muonic atoms - Revisited,” *Annals of Physics*, vol. 327, pp. 733–763, 2012. 1, 2, 10, 11, 12
- [4] A. P. Martynenko, “Lamb shift in the muonic helium ion,” *Physical Review A*, vol. 76, JUL 2007. 1, 13, 15
- [5] I. Sick, “Precise root-mean-square radius of ^4He ,” *Phys. Rev. C*, vol. 77, p. 041302, 2008. 1, 10, 13, 14, 15
- [6] F. Kottmann, W. Amir, F. Biraben, C. Conde, S. Dhawan, T. Hansch, F. Hartmann, V. Hughes, O. Huot, P. Indelicato, L. Julien, P. Knowles, S. Kazamias, Y. Liu, F. Mulhauser, F. Nez, R. Pohl, P. Rabinowitz, J. Dos Santos, L. Schaller, H. Schneuwly, W. Schott, D. Taqqu, and J. Veloso, “The muonic hydrogen Lamb shift experiment at PSI,” *Hyperfine Interactions*, vol. 138, no. 1-4, pp. 55–60, 2001. 1
- [7] R. Pohl, A. Antognini, F. Nez, F. D. Amaro, F. Biraben, J. M. R. Cardoso, D. S. Covita, A. Dax, S. Dhawan, L. M. P. Fernandes, A. Giesen, T. Graf, T. W. Hänsch, P. Indelicato, L. Julien, C.-Y. Kao, P. Knowles, E.-O. Le Bigot,

- Y.-W. Liu, J. A. M. Lopes, L. Ludhova, C. M. B. Monteiro, F. Mulhauser, T. Nebel, P. Rabinowitz, J. M. F. dos Santos, L. A. Schaller, K. Schuhmann, C. Schwob, D. Taqqu, J. F. C. A. Veloso, and F. Kottmann, “The size of the proton,” *Nature*, vol. 466, pp. 213–216, 2010. 1, 2, 10, 39, 43, 51, 52, 78
- [8] F. Nez, A. Antognini, F. D. Amaro, F. Biraben, J. M. R. Cardoso, D. Covita, A. Dax, S. Dhawan, L. Fernandes, A. Giesen, T. Graf, T. W. Haensch, P. Indelicato, L. Julien, C. Y. Kao, P. E. Knowles, E. Le Bigot, Y. W. Liu, J. A. M. Lopes, L. Ludhova, C. M. B. Monteiro, F. Mulhauser, T. Nebel, P. Rabinowitz, J. M. F. Dos Santos, L. Schaller, K. Schuhmann, C. Schwob, D. Taqqu, J. F. C. A. Veloso, F. Kottmann, and R. Pohl, “Is the proton radius a player in the redefinition of the International System of Units?,” *Phil. Trans. R. Soc. A - Math. Phy. and Eng. Scien.*, vol. 369, pp. 4064–4077, OCT 28 2011. 1, 2
- [9] A. Antognini, F. Nez, K. Schuhmann, F. D. Amaro, F. Biraben, J. M. R. Cardoso, D. S. Covita, A. Dax, S. Dhawan, M. Diepold, L. M. P. Fernandes, A. Giesen, A. L. Gouvea, T. Graf, T. W. Hänsch, P. Indelicato, L. Julien, C.-Y. Kao, P. Knowles, F. Kottmann, E.-O. Le Bigot, Y.-W. Liu, J. A. M. Lopes, L. Ludhova, C. M. B. Monteiro, F. Mulhauser, T. Nebel, P. Rabinowitz, J. M. F. dos Santos, L. A. Schaller, C. Schwob, D. Taqqu, J. F. C. A. Veloso, J. Vogelsang, and R. Pohl, “Proton Structure from the Measurements of 2S-2P Transition Frequencies of Muonic Hydrogen,” *Science*, vol. 339, pp. 417–420, Jan 2013. 1, 2, 10, 51, 52, 78
- [10] G. P. Christian, A. Matveev, J. Alnis, B. Bernhardt, A. Beyer, R. Holzwarth, A. Maistrou, R. Pohl, K. Predehl, T. Udem, T. Wilken, N. Kolachevsky, M. Abgrall, D. Rovera, C. Salomon, P. Laurent, and T. W. Hänsch, “Improved Measurement of the Hydrogen 1S2S Transition Frequency,” *Phys. Rev. Lett.*, vol. 107, p. , 2011. 1, 10

- [11] B. de Beauvoir, F. Nez, L. Julien, B. Cagnac, F. Biraben, D. Touahri, L. Hilico, O. Acef, A. Clairon, and J. J. Zondy, “Absolute Frequency Measurement of the 2S-8S/D Transitions in Hydrogen and Deuterium: New Determination of the Rydberg Constant,” *Phys. Rev. Lett.*, vol. 77, p. , 1997. 1
- [12] C. Schwob, L. Jozefowski, B. de Beauvoir, L. Hilico, F. Nez, L. Julien, F. Biraben, O. Acef, J. J. Zondy, and A. Clairon, “Optical Frequency Measurement of the 2S-12D Transitions in Hydrogen and Deuterium: Rydberg Constant and Lamb Shift Determinations,” *Phys. Rev. Lett.*, vol. 82, p. , 1999. 1
- [13] J. A. ans Kees de Jager and C. F. Perdrisat, “Nucleon Form Factors - A Jefferson Lab Perspective,” *Journal of Physics: Conference Series*, vol. 299, p. , 2011. 1, 10
- [14] J. Arrington, P. G. Blunden, and W. Melnitchouk, “Review of two-photon exchange in electron scattering,” *Prog. Part. Nucl. Phys*, vol. 66, pp. 782–833, 2011. 1
- [15] J. Arrington, “Coulomb corrections in the extraction of the proton radius,” arXiv:1210.267 [nucl-ex], 2013. 1, 10
- [16] P. J. Mohr, B. N. Taylor, and D. B. Newell, “CODATA recommended values of the fundamental physical constants: 2010,” *Rev. Mod. Phys.*, vol. 84, p. 1527, 2012. 1, 2
- [17] D. Taqqu, D. Biraben, C. Conde, T. Hänsch, F. Hartmann, P. Hauser, P. Indelicato, P. Knowles, F. Kottmann, F. Mulhauser, C. Petitjean, R. Pohl, P. Rabinowitz, R. Rosenfelder, J. dos Santos, W. Schott, L. Simons, and J. Veloso, “Laser spectroscopy of the Lamb shift in muonic hydrogen,” *Hyperfine Interactions*, vol. 119, pp. 311–315, 1999. 1, 14

-
- [18] R. Pohl, R. Gilman, G. A. Miller, and K. Pachucki, “Muonic Hydrogen and the Proton Radius Puzzle,” *Annu. Rev. Nucl. Part. Sci.*, vol. 63, pp. 175–204, 2013. 2
- [19] A. Antognini, F. Biraben, J. M. R. Cardoso, D. S. Covita, A. Dax, L. M. P. Fernandes, A. L. Gouvea, T. Graf, T. W. Hänsch, M. Hildebrandt, P. Indelicato, L. Julien, K. Kirch, F. Kottmann, Y. M. Liu, C. M. B. Monteiro, F. Mulhauser, T. Nebel, F. Nez, J. M. F. dos Santos, K. Schuhmann, D. Taqqu, J. F. C. A. Veloso, A. Voss, and R. Pohl, “Illuminating the proton radius conundrum: the μHe^+ lamb shift,” *Can. J. Phys.*, vol. 89, pp. 47–57, 2011. 2, 13, 14, 45, 51
- [20] A. Antognini, R. Pohl, F. D. Amaro, F. Biraben, J. M. R. Cardoso, D. S. Covita, A. Dax, S. Dhawan, L. M. P. Fernandes, A. Giesen, A. L. Gouvea, T. Graf, T. W. Hänsch, M. Hildebrandt, P. Indelicato, L. Julien, C.-Y. Kao, K. Kirch, P. Knowles, E.-O. Le Bigot, Y.-W. Liu, J. A. M. Lopes, L. Ludhova, C. M. B. Monteiro, F. Mulhauser, T. Nebel, F. Nez, P. Rabinowitz, J. M. F. dos Santos, L. A. Schaller, C. Schuhmann, K. Schwob, D. Taqqu, J. F. C. A. Veloso, A. Voss, and F. Kottmann, “The Lamb shift in muonic hydrogen and the proton radius,” *Physics Procedia*, vol. 17, pp. 10–19, 2011. 2
- [21] J. C. Bernauer and R. Pohl, “The Proton Radius Problem,” *Scientific American*, vol. 310, pp. 32–39, FEB 2014. 2
- [22] R. Pohl, T. Nebel, T. W. Hansch, F. Biraben, L. Indelicato, L. Julien, F. Nez, J. M. R. Cardoso, L. M. P. Fernandes, A. L. Gouvea, C. M. B. Monteiro, J. M. F. dos Santos, D. S. Covita, J. F. C. A. Veloso, A. Voss, T. Graf, K. Schuhmann, F. Kottmann, A. Antognini, K. Kirch, D. Taqqu, M. Hildebrandt, Y.-W. Liu, and A. Dax, “Proposal for an Experiment at PSI - Lamb Shift in Muonic Helium.” Internal Report, CREMA collaboration, January 2010. 3, 12, 14, 40, 45, 78, 122

- [23] Y. Yatsu, Y. Kuramoto, J. Kataoka, J. Kotoku, T. Saito, T. Ikagawa, R. Sato, N. Kawai, S. Kishimoto, K. Mori, T. Kamae, Y. Ishikawa, and N. Kawabata, “Study of avalanche photodiodes for soft X-ray detection below 20 keV,” *Nucl. Instrum. Meth. A*, vol. 564, pp. 334–143, 2006. 3, 30, 51, 59, 72, 75, 76
- [24] J. Kataoka, T. Saito, Y. Kuramoto, T. Ikagawa, Y. Yatsu, J. Kotoku, M. Arimoto, N. Kawai, Y. Ishikawa, and N. Kawabata, “Recent progress of avalanche photodiodes in high-resolution X-rays and γ -rays detection,” *Nucl. Instrum. Meth. A*, vol. 541, pp. 398–404, 2005. 3, 30, 51
- [25] P. Atkins, *The Elements of Physical Chemistry*. Oxford University Press, third revised ed., 2001. 8
- [26] R. Pohl, F. D. Amaro, A. Antognini, F. Biraben, J. M. R. Cardoso, D. S. Covita, A. Dax, S. Dhawan, L. M. P. Fernandes, A. Giesen, T. Graf, T. W. Hänsch, P. Indelicato, L. Julien, C.-Y. Kao, P. Knowles, E.-O. Le Bigot, Y.-W. Liu, J. A. M. Lopes, L. Ludhova, C. M. B. Monteiro, F. Mulhauser, T. Nebel, F. Nez, P. Rabinowitz, J. M. F. dos Santos, L. A. Schaller, K. Schuhmann, C. Schwob, , D. Taqqu, J. F. C. A. Veloso, and F. Kottmann, “The size of the proton and the deuteron,” *22nd International Conference on Atomic Physics*, vol. 264, p. 012008, 2011. 8
- [27] L. Ludhova, *The Muonic Hydrogen Lamb Shift Experiment: Lifetime and Population of the $\mu p(2S)$ State*. PhD thesis, Department of Physics, University of Fribourg, Faculty of Sciences, Department of Physics, University of Fribourg, Switzerland, OCT 2005. 9, 10, 11, 17, 92, 93
- [28] H. A. Bethe, “The electromagnetic shift of energy levels.,” *Phys. Rev. Lett.*, vol. 91, pp. 339–341, 1947. 9
- [29] T. W. Hänsch, J. Alnis, P. Fendel, m. Fischer, C. Gohle, M. Herrmann, R. Holzwarth, N. Kolachevsky, T. Udem, and M. Zimmermann, “Precision

-
- spectroscopy of hydrogen and femtosecond laser frequency combs,” *Phil. Trans. R. Soc. A - Math. Phy. and Eng. Scien.*, vol. 363, pp. 2155–2163, 2005. 10
- [30] A. A. Krutov and A. P. Martynenko, “Lamb shift in the muonic deuterium atom,” *Physical Review A*, vol. 84, 2011. 10
- [31] K. Pachucki, “Nuclear Structure Corrections in Muonic Deuterium,” *Phys. Rev. Lett.*, vol. 106, 2011. 10, 11, 12
- [32] T. Nebel, *The Lamb Shift in Muonic Hydrogen*. PhD thesis, Department of Physics, Ludwig-Maximilians University, Department of Physics, Ludwig-Maximilians University, Munchen, Germany, MAY 2010. 10, 12, 39, 100, 118, 131, 132
- [33] M. Eides, H. Grotch, and V. Shelyuto, “Theory of light hydrogenlike atoms,” *Physics Reports-Review Section of Physics Letters*, vol. 342, pp. 63–261, FEB 2001. 11
- [34] E. Borie, “Lamb shift of muonic deuterium,” *Phys. Rev. A*, vol. 72, 2005. 11, 12
- [35] P. Hauser, H. von Arb, A. Bianchetti, H. Hofer, F. Kottmann, and C. Lüchinger, “Search for the 2S-2P energy difference in muonic ^4He ions,” *Phys. Rev. A*, vol. 46, pp. 2363–2377, 1992. 12
- [36] T. Nebel, F. D. Amaro, A. Antognini, F. Biraben, J. M. R. Cardoso, D. S. Covita, A. Dax, L. M. P. Fernandes, A. L. Gouvea, T. Graf, T. W. Haensch, M. Hildebrandt, P. Indelicato, L. Julien, K. Kirch, F. Kottmann, Y. W. Liu, C. M. B. Monteiro, F. Nez, J. M. F. dos Santos, K. Schuhmann, D. Taqqu, J. F. C. A. Veloso, A. Voss, and R. Pohl, “The Lamb-shift experiment in Muonic helium,” *Hyperfine Interactions*, vol. 212, pp. 195–201, DEC 2012. 12, 45
- [37] H. P. von Arb, F. Dittus, H. Heeb, H. Hofer, F. Kottmann, S. Niggli, R. Schaeren, D. Taqqu, J. Unternhrer, and J. Egelhof, “Measurement of the

- lifetime and quenching rate of metastable 2S muonic helium ions,” *Phys. Lett. B*, vol. 136, p. 232, 1984. 12
- [38] B. Lauss, P. Ackerbauer, W. Breunlich, B. Gartner, M. Jeitler, P. Kammel, J. Marton, J. Prymas, W. and Zmeskal, D. Chatellard, J. Egger, H. Daniel, F. Hartmann, A. Kosak, and C. Petitjean, “Cascade in muonic deuterium atoms,” *Phys. Rev. A*, vol. 60, pp. 209–217, 1999. 12
- [39] C. A. N. Conde and A. J. P. L. Policarpo, “A gas proportional scintillation counter,” *Nucl. Instrum. Meth.*, vol. 53, pp. 7–12, 1967. 14
- [40] J. F. C. A. Veloso, J. A. M. Lopes, J. M. F. dos Santos, and C. A. N. Conde, “Performance characteristics of a gas proportional scintillation counter coupled to a microstrip gas chamber photosensor,” *IEEE Trans. Nucl. Sci.*, vol. 43, pp. 1232–1236, 1996. 14
- [41] J. F. C. A. Veloso, *Detectors Gasosos de Radiação Baseados em Microestruturas*. PhD thesis, Departamento de Física, Faculdade de Ciências e Tecnologia da Universidade de Coimbra, Portugal, JAN 2000. 16
- [42] J. A. M. Lopes, *Contadores Gasosos de Cintilação Proporcional: Novas Aplicações e Tecnologias de Fotossensores Integrados*. PhD thesis, Departamento de Física, Faculdade de Ciências e Tecnologia da Universidade de Coimbra, Portugal, 2002. 16, 17
- [43] L. M. P. Fernandes, *Characterization of Large Area Avalanche Photodiodes for Detection of X-Rays, Vacuum Ultraviolet and Visible Light*. PhD thesis, Department of Physics, University of Coimbra, Faculty of Sciences and Technology, Department of Physics, University of Coimbra, Portugal, APR 2005. 16, 17, 19, 32, 35, 36, 43, 70, 72

-
- [44] Advanced Photonix Inc., “LAAPDs,” Nov. 2013. http://www.advancedphotonix.com/ap_products/standard_SiAvalanche.asp?from=leftnav. 16
- [45] B. Koren and M. Szawlowski, “Large-area avalanche photodiodes challenge PMTs,” *Laser Focus World*, vol. 34, pp. 71–82, Nov 1998. 16, 28
- [46] J. P. Pansart, “Avalanche photodiodes for particle detection,” *Nucl. Instrum. Meth. A*, vol. 387, pp. 186–193, March 1997. 17, 30
- [47] M. Moszynski, M. Kapusta, M. Balcerzyk, M. Szawlowski, and D. Wolski, “Large Area Avalanche Photodiodes in X-rays and scintillation detection,” *Nucl. Instrum. Meth. A*, vol. 442, pp. 230–237, 2000. 17, 58
- [48] D. Renker, “Properties of avalanche photodiodes for applications in high energy physics, astrophysics and medical imaging,” *Nucl. Instr. Meth. A*, vol. 486, pp. 164–169, 2002. 17, 28, 31, 32, 55
- [49] M. Moszynski, M. Szawlowski, M. Kapusta, and M. Balcerzyk, “Large area avalanche photodiodes in scintillation and X-rays detection,” *Nucl. Instrum. Meth. A*, vol. 485, pp. 504–521, 2002. 17, 31, 32, 53, 55, 64, 68, 72, 74, 75, 96
- [50] F. Mulhauser, L. M. P. Fernandes, C. A. N. Antognini, A. Conde, O. Hout, P. E. Knowles, F. Kottmann, L. Ludhova, R. Pohl, J. M. F. Santos, L. A. Schaller, D. Taqqu, and J. F. C. A. Veloso, “LAAPD low temperature performance in X-ray and visible-light detection,” *Spect. Acta Part B*, vol. 58, pp. 2255–2260, 2003. 17
- [51] L. M. P. Fernandes, J. A. M. Lopes, J. M. F. dos Santos, P. E. Knowles, L. Ludhova, F. Mulhauser, F. Kottmann, R. Pohl, and D. Taqqu, “LAAPD low temperature performance in X-ray and visible-light detection,” *IEEE Trans. Nucl. Sci.*, vol. 51, pp. 1575–1580, 2004. 17, 53, 55, 59, 61, 72, 74, 75

- [52] L. Ludhova, F. D. Amaro, A. Antognini, F. Biraben, J. M. R. Cardoso, C. A. N. Conde, D. S. Covita, A. Dax, S. Dhawan, L. M. P. Fernandes, T. W. Hänsch, V. W. Hughes, O. Huot, P. Indelicato, L. Julien, P. E. Knowles, F. Kottmann, J. A. M. Lopes, Y. W. Liu, C. M. B. Monteiro, F. Mulhauser, F. Nez, R. Pohl, P. Rabinowitz, J. M. F. dos Santos, L. A. Schaller, D. Taquu, and J. F. C. A. Veloso, “Planar LAAPDs: temperature dependence, performance, and application in low-energy X-ray spectroscopy,” *Nucl. Instr. Meth. A*, vol. 540, pp. 169–179, 2005. 17, 31, 53, 55, 58, 59, 61, 64, 68, 74, 75, 77
- [53] L. M. P. Fernandes, F. D. Amaro, A. Antognini, J. M. R. Cardoso, C. A. N. Conde, O. Huot, P. E. Knowles, F. Kottmann, J. A. M. Lopes, L. Ludhova, C. M. B. Monteiro, F. Mulhauser, R. Pohl, J. M. F. dos Santos, L. A. Schaller, D. Taquu, and J. F. C. A. Veloso, “Characterization of large area avalanche photodiodes in X-ray and VUV-light detection,” *Journal Instr.*, vol. 2, 2007. 17, 31, 32, 36, 52, 58, 61, 63, 72, 74, 75, 76, 77, 96
- [54] L. M. P. Fernandes, J. A. M. Lopes, J. M. F. dos Santos, and C. A. N. Conde, “X-ray spectrometry with Petier-cooled large area avalanche photodiodes,” *Nucl. Instrum. Meth. B*, vol. 213, pp. 267–271, 2004. 17, 78
- [55] RAL, “CLRC Rutherford Appleton Laboratory, Chilton, Didcot, Oxfordshire, OX11, 0QX, England.” 19, 53, 78, 100
- [56] N. Tsoulfanidis, *Measurements and Detection of Radiation*. Taylor and Francis, second ed., 1995. 22, 24, 25, 27
- [57] W. R. Leo, *Techniques for Nuclear and Particle Physics Experiments - A How-to Approach*. Springer-Verlag, second revised ed., 1994. 22, 24, 25, 27
- [58] G. F. Knoll, *Radiation Detection and Measurements*. John Wiley and Sons, fourth ed., 2010. 22, 24, 25, 27, 32, 34, 35, 36, 37, 38, 52, 53

-
- [59] Center for Proton Therapy - PSI, “The Bragg peak,” 2014. <http://www.psi.ch/protontherapy/protons-and-their-properties>. 26
- [60] Albert Thompson, David Attwood et al, “X-Ray Data Booklet.” LBNL/PUB-490 Rev.3, Lawrence Berkeley Laboratory, University of California, Berkeley, CA 94720, October 2009. 28
- [61] T. E. Schlesinger, J. E. Toney, H. Yoon, E. Y. Lee, B. Brunett, L. Franks, and R. B. James, “Cadmium zinc telluride and its use as a nuclear radiation detector material,” *Materials Science and Engineering*, vol. 32, pp. 103–189, 2001. 29, 30
- [62] D. Gagnon, G. L. Zeng, J. M. Links, J. J. Griesmer, and F. C. Valentino, “Design Considerations for a New Solid-State Gamma-Camera: SOLSTICE,” *Proc. IEEE Nuclear Science Symposium and Medical Imaging Conference*, vol. 2, pp. 4–10, October 2001. 29, 30
- [63] T. H. Prettyman, M. C. Browne, K. D. Ianakiev, C. E. Moss, and S. E. Soldner, “Characterization of a large-volume multi-element CdZnTe detector,” *Proc. SPIE*, vol. 4141, pp. 1–10, November 2000. 29, 30
- [64] A. Owens, M. Bavdaz, H. Andersson, T. Gagliardi, M. Krumrey, S. Nenonen, A. Peacock, I. Taylor, and L. Trogër, “The X-ray response of CdZnTe,” *Nucl. Instr. Meth. A*, vol. 484, pp. 242–250, 2002. 29, 30
- [65] Amptek, “Amptek Inc., 14 De Angelo Drive, Bedford, MA, USA.” 29, 30
- [66] E. Abro and G. Johansen, “Low noise gamma-ray and X-ray detectors based on CdTe-materials,” *Nucl. Instr. Meth. A*, vol. 377, pp. 470–474, 1996. 30
- [67] P. J. Sellin, “Recent advances in compound semiconductor radiation detectors,” *Nucl. Instr. Meth. A*, vol. 513, pp. 332–339, 2003. 30

- [68] P. P. Webb and R. J. McIntyre, “Large Area Reach-Through Avalanche Diodes For X-ray Spectroscopy,” *IEEE Trans. Nucl. Sci.*, vol. 23, pp. 138–144, 1976. 30
- [69] S. Tanaka, Y. Kataoka, Y. Yatsu, M. Arimoto, M. Koizumi, N. Kawai, Y. Ishikawa, S. Kawai, and N. Kawabata, “Development of wideband X-rays and γ -ray spectrometer using transmission-type, large-area APD,” *Nucl. Instrum. Meth. A*, vol. 582, pp. 662–569, 2007. 30
- [70] T. Nakamori, T. Enomoto, T. Toizumi, K. Tokoyoda, Y. Yatsu, N. Kawai, J. Kataoka, Y. Ishikawa, T. Kawai, N. Kawabata, and Y. Matsunaga, “Development of X-ray/gamma-ray imaging spectrometers using reach-through APD arrays,” *Journal of Instrumentation*, vol. 7, MAR 2012. 30
- [71] M. Moszynski, M. Szawlowski, M. Kapusta, M. Balcerzyk, and D. Wolski, “Large Area Avalanche Photodiodes in X-rays and scintillation detection,” *IEEE Trans. Nucl. Sci.*, vol. 47, pp. 1297–1302, 2000. 31
- [72] L. M. P. Fernandes, J. A. M. Lopes, J. M. F. dos Santos, and C. A. N. Conde, “Application of large-area avalanche photodiodes to energy-dispersive x-ray fluorescence analysis,” *X-Ray Spectrom.*, vol. 30, pp. 164–169, 2001. 31, 55
- [73] D. Renker and L. E, “Advances in solid state photon detectors,” *JINST*, vol. 4, p. P04004, 2009. 31, 32, 36
- [74] T. R. Gentile, M. Bales, U. Arp, B. Dong, and R. Farrel, “Response of large avalanche photodiodes to low energy x rays,” *Review of Scientific Instruments*, vol. 83, pp. 1–9, 2012. 31
- [75] K. Ogasawara, F. Allegrini, M. I. Desai, S. Livi, and D. J. McComas, “A Linear Mode Avalanche Photodiodes for Ion Detection in the Energy Range 5-250 keV,” *IEEE Trans. Nucl. Sci.*, vol. 59, pp. 2601–2607, 2012. 31

-
- [76] S. Kasahara, T. Takashima, and M. Hirahara, “Variability of the minimum detectable energy of an APD as an electron detector,” *Nucl. Instr. Meth. A*, vol. 664, pp. 282–288, 2012. 31
- [77] B. J. Pichler, M. S. Judenhofer, C. Catana, J. H. Walton, M. Kneilling, R. E. Nutt, S. B. Siegel, C. D. Claussen, and S. R. Cherry, “Performance Test of an LSO-APD Detector in a 7-T MRI Scanner for Simultaneous PET/MRI,” *J. Nucl. Med.*, vol. 47, pp. 639–647, April 2006. 31
- [78] S. N. Ahmed, *Physics and Engineering of Radiation Detection*. Academic Press - Elsevier Science, first edition ed., 2007. 32, 34, 35, 36
- [79] J. Piprek, *Semiconductor Optoelectronic Devices - Introduction to Physics and Simulation*. Academic Press - Elsevier Science, first edition ed., 2003. 32, 34, 38
- [80] HMT, “Hamamatsu Photonics K.K.,1126-1, Ichino-cho, Higashi-ku, Hamamatsu City, Shizuoka Pref., 435-8558, Japan.” 32, 51
- [81] Hamamatsu, “Avalanche Photodiode,” 2014. <http://hamamatsu.magnet.fsu.edu/articles/avalanche.html>. 32, 33
- [82] Henke L.B.L. Gov., “X-ray attenuation length,” Apr. 2014. http://henke.lbl.gov/optical_constants/atten2.html. 32
- [83] R. J. McIntyre, “Multiplication Noise in Uniform Avalanche Diodes,” *IEEE Trans. Dev.*, vol. 13, pp. 164–168, 1966. 36
- [84] F. S. Goulding and D. A. Landis, “Signal Processing for Semiconductor Detectors,” *IEEE Trans. Nucl. Sci.*, vol. 29, pp. 1125–1141, 1982. 36
- [85] A. Antognini, F. Nez, F. D. Amaro, F. Biraben, J. M. R. Cardoso, D. S. Covita, A. Dax, S. Dhawan, L. M. P. Fernandes, A. Giesen, T. Graf, T. W. Hänsch,

- P. Indelicato, L. Julien, C.-Y. Kao, P. Knowles, F. Kottman, E.-O. Le Bigot, Y.-W. Liu, J. A. M. Lopes, L. Ludhova, C. M. B. Monteiro, F. Mulhauser, T. Nebel, P. Rabinowitz, J. M. F. dos Santos, L. A. Schaller, K. Schuhmann, C. Schwob, D. Taqqu, J. F. C. A. Veloso, and R. Pohl, “Muonic hydrogen spectroscopy: the proton radius puzzle,” in *ICONO 2010: International Conference on Coherent and Nonlinear Optics* (Fabre, C and Zadkov, V and Drabovich, K, ed.), vol. 7993 of *Proceedings of SPIE*, Russian Acad Sci; Russian Fdn Bas Res; Govt Republ Tatarstan; Opt Soc Amer; Russian Acad Sci; MV Lomonosov Moscow State Univ; Zavoisky Phys Tech Inst; Acad Sci Republ Tatarstan, 2011. Conference on ICONO 2010 - International Conference on Coherent and Nonlinear Optics, Kazan, RUSSIA, AUG 23-26, 2010. 42, 43, 44, 49
- [86] RMD, “Radiation Monitoring Devices Inc., Watertown, MA 02472, USA.” 47, 51
- [87] L. M. P. Fernandes, A. Antognini, M. Boucher, C. A. N. Conde, O. Huot, P. E. Knowles, F. Kottmann, L. Ludhova, F. Mulhauser, R. Pohl, L. A. Schaller, J. M. F. dos Santos, , D. Taqqu, and J. F. C. A. Veloso, “Behaviour of large-area avalanche photodiodes under intense magnetic fields for VUV- visible and X-ray photon detection,” *Nucl. Instrum. Meth. A*, vol. 498, pp. 362–368, 2003. 47, 77
- [88] Stefan Ritt, Pierre Amaudruz and Konstantin Olchanski , “MIDAS (Maximum Integrated Data Acquisition System),” 2014. <http://midas.psi.ch/html/doc/>. 49
- [89] CAEN, “V1720 8 channel (250 MS/s ADC) WFD,” Mar. 2014. <http://www.caen.it/csite>. 50
- [90] P. E. Optoelectronics, “PerkinElmer Inc., 940 Winter Street, Waltham, Massachusetts 02451, USA.” 51

-
- [91] M. N. Mazziotta, “Electron-hole pair creation energy and fano factor temperature dependence in silicon,” *Nucl. Instrum. Meth. A*, vol. 584, pp. 436–439, 2008. 53
- [92] ORTEC, “Amplifiers,” Dec. 2013. <http://www.ortec-online.com/>. 54, 79
- [93] Amptek, “Multichannel analyzer - Pocket MCA,” Nov. 2013. <http://www.amptek.com/mca8000a.html>. 54, 79
- [94] T. Lux, E. Freitas, F. Amaro, O. Ballestar, G. Jover-Manas, and C. M. et al., “Characterization of the Hamamatsu S8664 Avalanche Photodiodes for X-Ray and VUV-Light detection,” *Nucl. Instrum. Meth. A*, vol. 685, p. 11, 2012. 57
- [95] A. L. Gouvea, A. Antognini, F. Kottmann, R. Pohl, and L. M. P. Fernandes, “Reach-through avalanche photodiodes in soft X-ray detection,” *IEEE Trans. Nucl. Sci.*, vol. 61, pp. 1–6, 2014. 64, 96
- [96] N. I. Karmalitsyn, T. E. Sazonova, S. V. Sepman, and A. V. Zanevsky, “Standardization of the ^{65}Zn ,” *Applied Radiation and Isotopes*, vol. 60, pp. 391–395, 2004. 78, 79
- [97] N. N. D. Center, “Chart of Nuclides,” Dec. 2013. <http://www.nndc.bnl.gov/>. 78
- [98] Amptek, “Si-PIN XR-100CR,” Nov. 2013. <http://www.amptek.com/xr100cr.html>. 85, 86, 87
- [99] Henke L.B.L. Gov., “X-ray attenuation length,” Dec. 2013. <http://henke.lbl.gov/cgi-bin/filter.pl>. 94
- [100] F. Mulhauser, L. Ludhova, and P. E. Knowles, “LAAPD’s and Related Electronics Study.” Internal Report, University of Fribourg, August 2002. 100

Curriculum Vitæ

Andrea Leite Gouvêa was born in Coimbra in September 24 of 1980. After finished her basic school in Ponte de Sor, she moved to Portalegre to finished the secondary school. She started university education in 1998 in Electronics and Computer Engineering at the University of Coimbra and moved to Biomedical Engineering in 2002. In 2006 she started in research world with a grant for under-graduate students in Laboratório de Física Experimental de Partículas (LIP) in the project, “Applications of Timming Resistive Plate Chambers developed in CERN to FAE and Radioisotope Imaging” in the team of gas detectors, specifically in the field of Resistive Plate Chamber (RPC). She finished her graduation in 2007 with the thesis “Temporal resolution measurement of gas detector - RPC, designed for time of flight (TOF) - Positron Emission Tomography (PET)” under the supervision of Professor Rui Marques and Professor Paulo Fonte. In 2008 she started research in the University of Aveiro in the Group - Grupo de Detecção de Radiação e Imagiologia Médica (DRIM) with the project, “Gamma detectors for Medical Imaging” under the supervision of Professor João Filipe Calapez de Albuquerque Veloso. In 2009 she finished her M.Sc. studies and from 2010 to 2014 she worked in her Ph.D., under the supervision of Dr. Luis Fernandes and Dr. Randolph Pohl. The project is dedicated to determine the Lamb Shift in mounic helium, with focus on the X-ray detection system. The aim of the project is to determine the helium RMS nuclear radius with a relative accuracy of 3×10^{-4} . In addition the fine structure components and the magnetic moment distributions will be revealed. Some results of her work have

been published in this thesis, as well as in peer-reviewed papers in international journals. During the Ph.D., in March of 2010 she had the opportunity to attend to an "Intense Course on Accelerators and Reactor Operation" - ICARO in Catania-Palermo, Italy and more recently in March of 2013 she attended to "Excellence in Detectors and Instrumentation Technology (EDIT)" in Tsukuba, Japan. Her research activity during this time was supported by the Portuguese Foundation for Science and Technology (FCT).

List of Publications

Papers in international peer-reviewed journals

- **“Reach-Through Avalanche Photodiodes in low-energy X-ray detection”**
Gouvea A.L., Fernandes L.M.P., Kottmann F., Antognini A., and Pohl R.
Published in IEEE Transaction on Nuclear Science, vol. 61, pp. 1-6, Aug. 2014
DOI: 10.1109/TNS.2014.2331461
- **“Energy Resolution Contributions in Reach-Through Avalanche Photodiodes”**
Gouvea A.L. and Fernandes L.M.P.
Accepted for publication in IEEE Transaction on Nuclear Science, Oct. 2014
DOI: 10.1109/TNS.2014.2356854
- **“Lifetime and population of the 2S state in muonic hydrogen and deuterium”**
Diepold M., Amaro F., Antognini A., Biraben F., Cardoso M.R.J. et al.
Published in Physical Review A, vol. 88, pp. 042520-042526, Oct. 2013
DOI: 10.1103/PhysRevA.88.042520
- **“Laser spectroscopy of muonic hydrogen”**
Pohl R., Antognini A., Amaro F.D., Biraben F., Cardoso M.R.J. et al.
Published in Annalen Der Physik, vol. 525, pp. 647-651, Sep. 2013
DOI: 10.1002/andp.201300058

- **“Proton Structure from the Measurement of 2S-2P Transition Frequencies of Muonic Hydrogen”**

Antognini A., Nez F., Schuhmann K., Amaro F.D., Biraben F. et al.

Published in Science, vol. 339, pp. 417-420, Jan. 2013

DOI: 10.1126/science.1230016

- **“The Lamb-shift experiment in Muonic helium”**

Nebel T., Amaro F.D., A., Antognini A., Biraben F., Cardoso M.R.J. et al.

Published in Hyperfine Interactions, vol. 212, pp. 195-201, Dec. 2012

DOI: 10.1007/s10751-012-0637-0

- **“The Lamb shift in muonic hydrogen and the proton radius”**

Antognini A., Pohl R., Amaro F.D., Biraben F., Cardoso M.R.J. et al.

Published Physics Procedia, vol. 17, pp. 10-19, 2011

DOI: 10.1016/j.phpro.2011.06.012

- **“Illuminating the proton radius conundrum: the μ He⁺ lamb shift”**

Antognini A., Biraben F., Cardoso J.M.R., Covita D.S., Dax A. et al.

Published in Canadian Journal of Physics, vol. 89, pp. 47-57, Jan. 2011

DOI: 10.1139/P10-113

- **“Energy resolved X-ray fluorescence imaging based on a micropattern gas detector”**

Veloso J.F.C.A., Silva A.L.M., Oliveira C.A.B., Gouvea A.L., Azevedo C.D.R. et al.

Spectrochimica Acta Part B, vol. 65, pp. 241-247, Mar. 2010

DOI: 10.1016/j.sab.2010.03.006

- **“The 2D-Micro Hole & Strip Plate in CF₄ atmosphere aiming neutron imaging”**

da Luz H.N., Gouvea A.L., Mir J.A., dos Santos J.M.F. and Veloso J.F.C.A.

Published in the Journal of Instrumentation, vol. 4, pp. P12010, Dec. 2009

DOI: 10.1088/1748-0221/4/12/P12010

- **“EDXF imaging of Pb depth penetration in glazed ceramics using a Micropattern Gas Detector”**

Silva A.L.M., Oliveira C.A.B., Gouvea A.L., dos Santos J.M.F., Carvalho M.L. et al.

Published in the Analytical Bioanalytical Chemistry, vol. 395, pp. 2073-2080, Dec. 2009

DOI: 10.1007/s00216-009-3196-8

Papers in Conference Proceedings

- **“Reach-Through APDs for X-ray detection”**

Gouvea A.L., Fernandes L.M.P., dos Santos J.M.F and Kottmann F.

Presented in the Congress 2012 IEEE Nuclear Science Symposium and Medical Imaging Conference, Anaheim, California, Oct 29 - Nov 3, 2012

Published in the Conference Records 2012 NSS/MIC, pp. 424-427, 2012

DOI: 10.1109/NSSMIC.2012.6551140

- **“Energy Resolution Contributions in Reach-through Avalanche Photodiodes”**

Fernandes L.M.P., Gouvea A.L., dos Santos J.M.F and Kottmann F.

Presented in the Congress 2012 IEEE Nuclear Science Symposium and Medical Imaging Conference, Anaheim, California, Oct 29 - Nov 3, 2012

Published in the Conference Records 2012 NSS/MIC, pp. 415-417, 2012

DOI: 10.1109/NSSMIC.2012.6551137

- **“Quantum X-ray imaging with the 2D Micro Hole and Strip Plate”**

Gouvea A.L., da Luz H.N., Santos C.A., Oliveira C.A.B., Silva A.L.M. et al.

Presented in the World Congress 2009 on Medical Physics and Biomedical Engineering, Munich, Germany, September 7-12, 2009

Published in the Conference Records of IFMBE Proceedings, vol. 25/2, pp. 890-893, 2009

DOI: 10.1007/978 – 3 – 642 – 03879 – 2_249

- **“X-ray Polarimetric Measurements in Xenon Gas Filled Detectors”**

Botte G.S., Rachinhas P.J.B.M., Dias T.H.V.T., Curado da Silva R.M., Veloso J.F.C.A. et al.

Presented in the 2008 IEEE Nuclear Science Symposium and Medical Imaging, Special focus Workshop on X-Ray Micro Imaging of Materials, Devices, and Organisms, Dresden, Germany, October 19-25, 2008

Published in the Conference Records 2008 NSS/MIC, pp. 943-946, 2008

DOI: 10.1109/NSSMIC.2008.4774550

Poster Communications

- **“The X-ray detection system for the Muonic Helium Experiment”**

Gouvea A.L.

International School EDIT 2013: Excellence in Detectors and Instrumentation Technologies , KEK, Tsukuba, Japan, March 12-22, 2013

- **“Reach-through APDs for X-ray detection”**

Gouvea A.L., Fernandes L.M.P., dos Santos J.M.F. and Kottmann F.

2012 IEEE Nuclear Science Symposium and Medical Imaging Conference, Anaheim, California, October 29 - November 3, 2012

- **“Energy Resolution Contributions in Reach-through Avalanche Photodiodes”**

Fernandes L.M.P., Gouvea A.L., dos Santos J.M.F. and Kottmann F.

2012 IEEE Nuclear Science Symposium and Medical Imaging Conference, Anaheim, California, October 29 - November 3, 2012

- **“Quantum X-ray imaging with the 2D Micro Hole and Strip Plate”**

Gouvêa A.L., da Luz H.N., Oliveira C.A.B., Azevedo C.D.R., Silva A.L.M. et al.

World Congress 2009 on Medical Physics and Biomedical Engineering, Munich, Germany, September 7-12, 2009

- **“CsI Photoelectron Extraction Efficiency in HpXe medium”**

Azevedo C.D.R., Gouvêa A.L., Santos C.A., Oliveira C.A.B, Veloso J.F.C.A et al.

2009 IEEE Nuclear Science Symposium and Medical Imaging Conference, Orlando, Florida, October 25-31, 2009

- **“2D-Sensitive HpXe Gas Proportional Scintillation Counter”**

Azevedo C.D.R., Gouvêa A.L., da Luz H.N., Veloso J.F.C.A. et al.

2009 IEEE Nuclear Science Symposium and Medical Imaging Conference, Orlando, Florida, October 25-31, 2009

- **“The 2D-Micro Hole & Strip Plate in CF4”**

da Luz H.N., Gouvêa A.L., Mir J.A., dos Santos J.M.F., Veloso J.F.C.A. et al. MPGD2009, Crete, Greece, June 12-15, 2009

- **“X-ray Polarimetric Measurements in Xenon Gas Filled Detectors”**

Botte G.S., Gouvêa A.L., Conde C.A.N., Stauffer A.D. et al.

2008 IEEE Nuclear Science Symposium and Medical Imaging, Special focus Workshop on X-Ray Micro Imaging of Materials, Devices, and Organisms, Dresden, Germany, October 19-25, 2008

- **“CF4 Filled Micropattern Detector Aiming Neutron Imaging”**

Veloso J.F.C.A., Mir J.A., da Luz H.N., Gouvêa A.L. et al.

8th International Conference on Position Sensitive Detectors, Glasgow, Scotland, UK, September 1-5, 2008